Measurements of Neutron Doses from Radiotherapy with ^{12}C Ions and Photons

Master Thesis in Nuclear Physics

by

Kristian Ytre-Hauge

University of Bergen
Department of Physics and Technology
May 2009

Acknowledgments

First of all I would like to thank my supervisors Professor Dieter Röhrich and Dr. Scient. Odd Harald Odland. Thanks to Professor Dieter Röhrich for making it possible for me to perform experiments at GSI and be introduced to the scientific community there. Also thanks for guidance and clarifying conversations. Thanks to Dr. Scient. Odd Harald Odland for organizing measurements at Haukeland University Hospital (HUS) and for being helpful and enthusiastic in every aspect of this project.

Thanks to Camilla Hanquist Stokkevåg who has been working together with me during the majority of the experimental work performed in this thesis. It has been inspiring and very helpful to be able to discuss the experimental methods and results with you.

I would like to thank the head of the Medical Physics Section at HUS, Anfinn Mehus, for his committed support of this project. I also want to thank Finn Totland for guidance concerning the TLD system at HUS.

Thanks to Dieter Schardt for your time, support and guidance during my stays at GSI. I would also like to thank Giovanna Martino for introducing me to the work performed in the biophysics group at GSI.

Thanks to Dagfinn Knutsen for making the phantom used for the measurements.

Thanks to my fellow students at 5^{th} floor for your friendship and many enlightening discussions on physics. Especially, I would like to thank Knut Arne Birkedal for his friendship throughout the 5 years we have studied together in Bergen.

A special thanks to my parents, Karl Ytre-Hauge and Lillian Ytre-Hauge for encouraging me to focus on my studies, and thanks to my brothers Helge, Sigmund and Vidar who always have given me inspiration to improve myself.

Bergen, 20th May, 2009

Kristian Ytre-Hauge

Summary

The overall objective of this thesis has been to investigate the neutron doses from radiotherapy with photons and ions. The advantages of proton and ion therapy, compared to the use of photons were also examined.

During cancer radiotherapy, patients receive undesired dose from neutrons produced in collimators and in the patient. Measurements with bubble detectors were performed to investigate neutron doses from radiotherapy, using 200 MeV/u ^{12}C ions, at GSI-Darmstadt in Germany, and a 15 MeV photon beam at Haukeland University Hospital in Bergen. Neutron energy spectra were also obtained from the photon beam measurements. The bubble detectors were tested in a series of measurements to investigate the uncertainties in the measurements of neutron dose.

The principles of neutron production were investigated both for radiotherapy with photons and carbon ions. During photon radiotherapy, neutrons are produced through photonuclear reactions. The majority of the neutrons are produced in the target and the collimators in the linear accelerator, but neutrons can also be produced in the patient body if the photon energy is sufficiently high. The carbon therapy facility at GSI do not use collimators, but neutrons are still produced through nuclear interactions between the primary carbon ions and nuclei in the patient.

Neutron sensitive thermoluminescence detectors and a uranium-based fission counter have also been tested as neutron detectors in this study. Only preliminary tests have been performed with these detectors, and neutron doses have not been obtained with these detectors in this work.

The total neutron dose from radiotherapy with photons was found to be in the order of mSv per Gray. The spectra obtained indicate a neutron fluence in the order of 10^7 $n.cm^{-2}$ per Gray with a peak in the neutron energy around 1 MeV for measurements without a phantom, while compared to this, the spectra for in-phantom measurements are shifted downwards in energy. Concerning the spectra obtained, the results indicate that the uncertainties are relatively large, making it difficult to reach conclusive information.

Changes in response of the bubble detectors due to temperature variations in the measuring environment has been one of the factors which increased the uncertainties in the measurements. Changes in response for the bubble detectors after repeated use have also had an influence on the results. Future measurements should be made using the knowledge gained in this work in order to reduce uncertainties. The bubble detectors' response to neutrons of energies above 20 MeV was not established during these measurements, therefore, no conclusion has been drawn concerning the equivalent neutron doses from carbon radiotherapy.

Contents

Acknowledgments **i**

Summary **iv**

1 Introduction **1**

2 Radiotherapy With Photons **5**
- 2.1 Interaction of Photons With Matter 5
  - 2.1.1 The photoelectric effect 6
  - 2.1.2 Compton scattering 6
  - 2.1.3 Pair production 9
  - 2.1.4 Photon beam attenuation 9
- 2.2 Neutron Contamination of the Photon Beam 11
  - 2.2.1 Neutron production through photon interactions . . . 11
  - 2.2.2 Neutron spectra and attenuation 16
- 2.3 Accelerators for Photon Radiotherapy 20

3 Radiotherapy With Hadrons **23**
- 3.1 Interaction of Charged Particles With Matter 24
  - 3.1.1 The Bethe-Bloch equation 25
  - 3.1.2 Lateral scattering 26
  - 3.1.3 Neutron production and fragmentation 26
- 3.2 Principles of Particle Therapy 28
- 3.3 Relative Biological Effectiveness 30
- 3.4 Accelerators for Particle Therapy 32
- 3.5 GSI-Darmstadt 32
  - 3.5.1 Intensity Modulated Particle Therapy 34
  - 3.5.2 Online PET scan with ^{12}C beam 34
  - 3.5.3 Moving targets 35

4 Dosimetry **37**
- 4.1 Dosimetric Quantities 37
  - 4.1.1 Absorbed dose 37
  - 4.1.2 The biological effects of ionizing radiation 38

4.1.3 Equivalent dose 40
4.1.4 Effective dose 41
4.2 Dose deposition 41
4.2.1 Dose deposition from neutrons 42
4.3 Shielding Considerations 43

5 Neutron Detectors **45**
5.1 BF_3 Proportional Counter 46
5.2 Bubble Detectors 46
5.2.1 Physical principles of bubble detectors 47
5.2.2 Response to protons 50
5.2.3 Bubble detector spectrometer - BDS 50
5.2.4 BDS detectors' response to high energy neutrons . . . 52
5.2.5 Bubble detector thermal - BDT 53
5.2.6 Recompression of bubbles 54
5.2.7 Counting of bubbles 54
5.3 Thermoluminescence Detectors - TLD 54
5.3.1 Principles of thermoluminescence 54
5.3.2 TLD neutron dosimetry 56
5.4 Thin Film Breakdown Counter - TFBC 56

6 Experimental Setup **59**
6.1 Neutron Source Setup 59
6.2 Photon Beam Setup 59
6.3 Carbon Beam Setup 63

7 Experimental Results and Discussion **67**
7.1 Bubble Detector Characteristics 67
7.1.1 Reproducibility tests 68
7.1.2 Spread in sensitivity 69
7.1.3 Temperature dependence of the BDS 71
7.1.4 Disintegration of bubble detectors 72
7.2 Neutron Source Measurements 76
7.2.1 Spectrum measurements with the BDS 76
7.2.2 Thermal neutron measurements 80
7.3 Photon Beam Measurements 80
7.3.1 Isocenter plane spectrum 81
7.3.2 In-phantom spectra 83
7.3.3 Integral fluence and equivalent dose 86
7.4 Thermal Neutrons in the Photon Setup 88
7.5 Carbon beam measurements 89

8 Conclusion **95**

Bibliography **98**

A Particle Therapy Facilities **103**

B BDS Spectrum Unfolding Procedure **105**

C Photon Beam Data **109**

D Carbon Beam Data **111**

E Error Propagation in the Unfolding Process **113**

F Neutron Conversion Factors **115**

Chapter 1

Introduction

As of 2009, cancer is the second most frequent cause of death in developed countries in the world. Research on cancer treatment is performed on a large scale with different approaches. The three main cancer treatment branches are radiotherapy, surgery and chemotherapy. To increase the chances of recovering from malignancy, the three are often combined. About 50% of cancer patients receive radiation therapy. The by far most common radiotherapy today is the use of an external high energy photon beam. Substantial progress in radiotherapy with photons has been made over the last decades, and there is a continuous effort on improving the treatment techniques for all kinds of cancer diagnostics.

During the last decades, several changes and developments in photon radiotherapy have taken place with the purpose of increasing the treatment efficiency. The introduction of intensity modulated radiotherapy (IMRT) has improved the confinement of the photon beam to the target volume by the use of medical linear accelerators equipped with dynamic multileaf collimator systems (MLCs) and sophisticated optimization algorithms. The energies of the photon beams applied have also increased in order to more efficiently damage the cancer cells. However, the extended use of MLCs combined with photon beams with energies of 15 MeV, 18 MeV or even higher, contributes to that patients of today receive a higher neutron dose than earlier [1].

Growing attention has evolved for the consequences from the neutron dose received during radiotherapy. The neutron dose is mainly related to an increased risk of secondary malignancies outside of the target volume. Factors contributing to the increased concern are the increased use of collimators in radiotherapy with photons and the fact that the number of younger cancer survivors with prospects of a long life after the initial treatment has increased. The latter may result in that late effects from radiotherapy in a larger scale are revealed.

Techniques involving extended use of collimators will require more radiation dose output, referred to in this thesis as monitor units (MU), and thus might produce more secondary particles that contribute to dose also outside the treatment volume. Comparisons between conventional treatment and IMRT shows that the neutron dose can be up to three times higher for IMRT treatments [1]. Standard treatment planning today does not take into account neutron producing interactions.

An alternative to radiotherapy with photons is the use of high energy proton and heavy ion beams. These techniques have a greater potential than photons with respect to dose control, normal tissue sparing and treatment of radioresistant tumors. The use of high energy protons and ions in cancer treatment is often referred to as particle therapy or hadron therapy.

In hadron therapy using passive scattering techniques, the neutron dose outside the main radiation field is also significant. In the future, most particle therapy facilities will use beam scanning techniques employing magnetically scanned pencil beams over the target volume or similar solutions without the use of collimators. This eliminates the problem of neutron production in collimators, however, neutrons are still produced inside the patient. The primary beam particles will be fragmented through nuclear reactions with nuclei in the body resulting in a mixed particle field including neutrons, protons and heavier fragments up to the primary ions.

Experimental evaluation of the neutron field from a medical linear accelerator is difficult due to the dominating photon component in the radiation field and the pulsed nature of the beam. The photon background can cause noise problems, and the intense pulses result in dead-time errors in active detectors. It is therefore important to use detectors that are suited for the radiation environment in which the measurements are to be performed. For these reasons, passive detectors are often preferred.

In this work, the main focus has been on two types of bubble detectors from the vendor, Bubble Technology Industries (BTI); A ^{6}Li-based detector, Bubble Detector Thermal (BDT), which mainly measures thermal neutrons, and a spectrometer set, Bubble Detector Spectrometer (BDS), of bubble detectors. The spectrometer set consists of detectors with six different energy thresholds covering the neutron energy range of 10 keV - 20 MeV. The main advantages of bubble detectors are that they are passive devices, and insensitive to photons, making them suitable for measurements in a pulsed radiation field with a large photon background.

The bubble detectors have also been used for neutron dose measurements in a ^{12}C beam. The problems related to short intense pulses and large gamma background in the radiation field are not present here. The use of active detectors can therefore be a good solution. However, bubble detectors may still be a good alternative, or supplement, for neutron dose measurements due to their relatively low sensitivity to other particles, e.g. protons and photons.

In addition to the bubble detectors, preliminary tests have been performed with thermoluminescence detectors and a fission counter in order to investigate these detectors as alternatives in neutron dosimetry.

Chapter 2

Radiotherapy With Photons

Radiotherapy with photons is today the most widely used radiation for cancer treatment. It is used in hospitals in all parts of the world, and there is an ongoing world wide continuous development of new techniques. Medical linear accelerators (linacs) delivering photon beams in the energy range 4-25 MeV are used for external irradiation of tumors.

The goal of radiation therapy is to damage as many cancer cells as possible, while limiting damage to healthy tissue. The photon beam is shaped by collimators in order to hit the tumor and avoid healthy tissue. The beam shaping collimators are usually made of lead and tungsten. Both cancer cells and healthy tissue hit by the photon beam will be damaged. Consequently there is a limit on how much one may irradiate a person. The treatment is given in fractions, allowing healthy tissue to recover between the treatments. In the last decades radiotherapy with photons has been improved by the introduction of image guided radiotherapy (IGRT) and intensity modulated radiotherapy (IMRT). IGRT includes the use of diagnostic imaging systems which is the use of x-ray cameras integrated in the medical linac for more precise positioning of the patients.

2.1 Interaction of Photons With Matter

Because the photon is a neutral particle, it does not collide inelastically with atomic electrons like charged particles do. Nevertheless, the photons will undergo a multitude of different interactions when passing through matter. The main interactions are; the photoelectric effect, Compton scattering and pair production [2]. Other less dominant interactions are Rayleigh scattering, Thomson scattering and photonuclear reactions.

2.1.1 The photoelectric effect

A photon passing through matter can be absorbed by an atomic electron, and the electron is subsequently ejected from the atom. This phenomenon is known as the photoelectric effect. The process is illustrated in figure 2.1. The electron has to be bound in an atom for this absorption to happen. The reason for this is that there must be a nucleus in the vicinity to absorb the recoil momentum so that the total momentum is conserved in the interaction. The probability for interaction is highest if the photon energy is equal or slightly higher than the binding energy of the atomic electron. All the energy from the photon is transferred to the electron, consequently, the kinetic energy of the outgoing electron, often referred to as the photo electron, will be

$$E_e = h\nu - E_b \tag{2.1}$$

where $h\nu$ is the photon energy and E_b is the binding energy of the electron. Photons can interact with electrons in the K, L, M or N shells. After this process, there will be an electron missing from one of these shells. An electron from one of the outer shells will undergo a transition to fill this vacancy, and at the same time it will emit characteristic x-rays [3]. There is also the possibility of emission of Auger electrons, which are monoenergetic electrons produced by the absorption of characteristic x-rays internally by the atom. As seen from figure 2.4, the cross section for photoelectric effect as a function of the photon energy, has some sharp edges. These are known as absorption edges and correspond to a rise in the interaction cross section when the photon energy reaches the binding energy for a new electron energy level. The cross section for the photoelectric effect increases with Z^5 for photons with energies in the MeV range. This indicates that high-Z materials are a good choice of shielding material for photons.

2.1.2 Compton scattering

The process of Compton scattering is scattering of photons on essentially free electrons, i.e. the outer electrons. In matter, the electrons are bound, but if the photon energy is high compared to the binding energy of the electrons, they can be considered to be essentially free. By applying energy and momentum conservation the following relations can be derived

$$h\nu' = \frac{h\nu}{1+\gamma(1-cos\theta)}, \tag{2.2}$$

$$T = h\nu - h\nu' = h\nu\frac{\gamma(1-cos\theta)}{1+\gamma(1-cos\theta)}, \tag{2.3}$$

$$cos\theta = 1 - \frac{2}{(1+\gamma)^2 tan^2\phi + 1}, \tag{2.4}$$

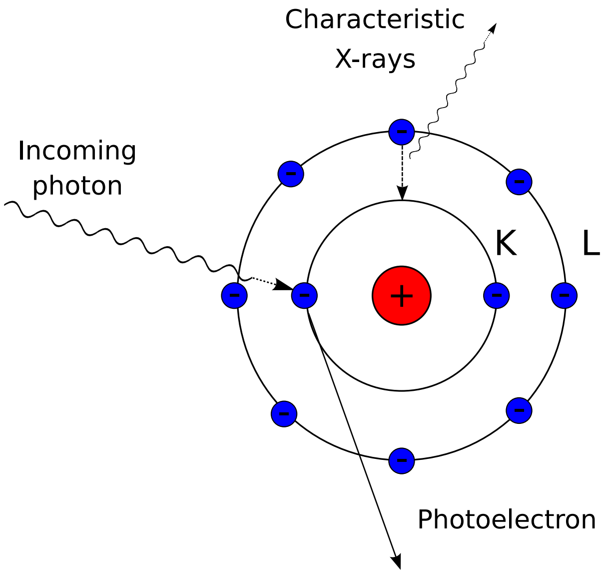

Figure 2.1: Illustration of the process of the photoelectric effect. An incoming photon is absorbed by an electron which escapes from the atom. Outerlaying electrons will fall to a lower shell to fill the vacancy. Characteristic x-rays is emitted in this process.

$$cot\phi = (1+\gamma)tan\frac{\theta}{2} \tag{2.5}$$

where

$$\gamma = \frac{h\nu}{m_e c^2} \tag{2.6}$$

If a photon makes a direct hit on an electron, the scattered photon may travel backwards ($\gamma = 180°$) and the electron in forward direction ($\phi = 0°$). In this case maximum energy is transferred from the photon to the electron. Using equation 2.3 this yields

$$T_{max} = h\nu(\frac{2\gamma}{1+2\gamma}) \tag{2.7}$$

which is called the Compton energy edge.

Considering two cases, a high energy photon and a low energy photon, illustrates the energy dependence of the Compton effect. A photon with energy 51.1 keV gives the following maximum energy transfer

$$T_{max} = 51.1\ keV(\frac{2\times 0.1}{1+2\times 0.1}), \tag{2.8}$$

$$\Rightarrow T_{max} = 8.52\ keV \tag{2.9}$$

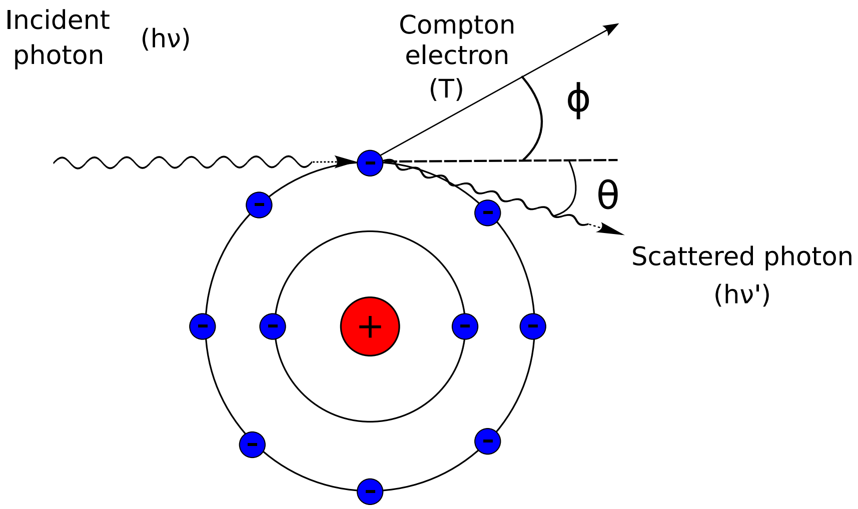

Figure 2.2: Compton scattering. The initial photon energy is denoted as hν, T is the kinetic energy of the compton electron and hν' is the energy of the scattered photon.

while a photon with an energy of 10.22 MeV, which is a typical energy for radiotherapy, yields a maximum energy transfer

$$T_{max} = 10.22MeV(\frac{2*20}{1+2*20}), \tag{2.10}$$

$$\Rightarrow T_{max} = 9.76MeV \tag{2.11}$$

From these examples it can be seen that high energy photons will deposit a larger fraction of their energy through Compton scattering. In other words, Compton interactions involving high energy photons causes a relatively large amount of energy absorption in the tissue compared to the deposition of energy through Compton scattering of low photon energies. The variation of the Compton scattering cross section with photon energy can be seen in figure 2.4. As figure 2.4 shows, dose deposition is at low photon energies is dominated by the photoelectric effect.

It is important to note that because the electrons are considered to be essentially free, the Compton effect will have little dependence on the atomic number Z, of the matter. The electron density (electrons per cm^3) will be the important factor for attenuation of a photon beam by Compton scattering.

Related to Compton scattering are the classical processes of Rayleigh and Thomson scattering. Rayleigh scattering is scattering of photons by atoms as a whole. This is also referred to as coherent scattering because all the electrons in the atom participate in a coherent manner. Thomson scattering is the scattering of photons by free electrons in the classical limit.

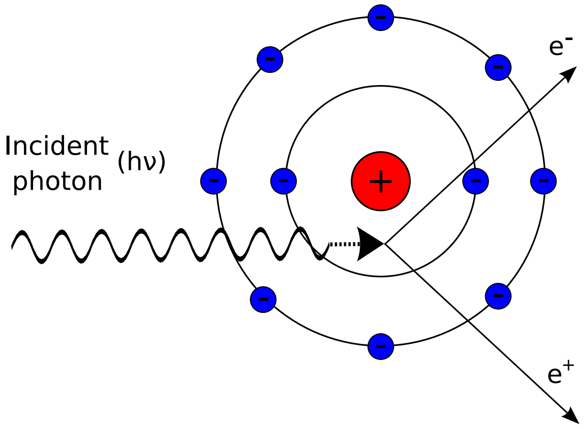

Figure 2.3: Illustration of the process of pair production. A photon is transformed to an electron positron pair in the vicinity of a nucleus.

Both in the case of Thomson and Rayleigh scattering the atoms are neither excited nor ionized and only the direction of the photon is changed. At the photon energies used in medical linacs the contribution from Thomson and Rayleigh scattering is very small and can be neglected [2].

2.1.3 Pair production

The mechanism of pair production involves a photon transforming into an electron-positron pair. All the photon energy is transferred to the created particles. The electron has a rest mass of 0.511 MeV, consequently, the threshold photon energy for pair production is 1.022 MeV. The photon energy excess above this threshold can be distributed evenly or uneven between the two particles, but the most probable case is for each particle to acquire half of the excess energy. In order to conserve momentum, pair production can only occur if there is another particle in the vicinity, usually a nucleus [2].

Contrary to the Compton effect, the pair production increases rapidly with atomic number, Z. In fact, pair production cross section is proportional to Z^2. Furthermore, the cross section for a given material increases as the logarithm of the incident excess photon energy above the threshold for interaction. The cross section for pair production in lead is shown in figure 2.4.

2.1.4 Photon beam attenuation

The probability for a photon to interact is the sum of the individual cross sections for the various interactions the photon can go through. When only considering the main interactions, the photoelectric effect, Compton scattering and pair production, the total cross section per atom is given as

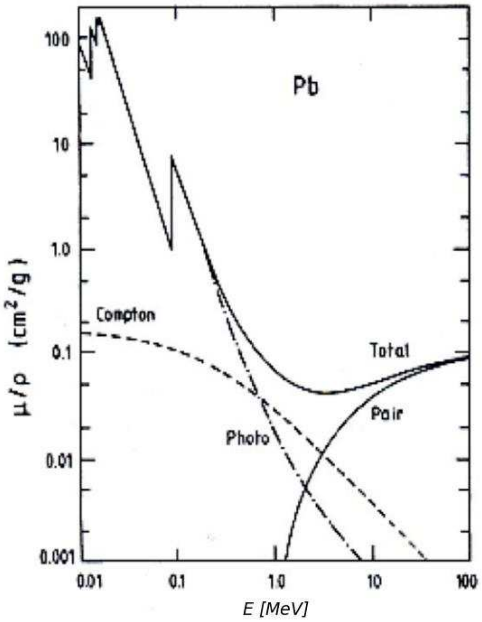

Figure 2.4: Mass absorption coefficient for photons in lead. This illustrates the cross sections' dependence of photon energy for the three main interactions with matter.

$$\sigma_{tot} = \sigma_{ph} + \sigma_c + \sigma_{pair} \tag{2.12}$$

where the Compton cross section is multiplied by Z to take into account the number of electrons per atom [2]. The probability of interaction per unit length is found by multiplying the total cross section, σ by the density of atoms, N.

$$\mu = \sigma \times N = \sigma(\frac{N_a \times \rho}{A}) \tag{2.13}$$

N_a is Avogadro's number, ρ is the density of the material and A is the molecular weight. μ is known as the total absorption coefficient and is the inverse of the mean free path of the photon. Because the absorption depends on the number of electrons present, μ depends on the density of the material. Thus, by dividing μ by the density ρ, the resulting coefficient will be independent of density. μ/ρ is known as the mass absorption coefficient. This is shown in figure 2.4 for photons in lead.

The number of photons in a photon beam traversing a material can be expressed as

$$dN = -\mu N dx \tag{2.14}$$

Where μ, the total absorption coefficient, is the constant of proportionality and N is the initial number of photons. In terms of intensity the equation becomes

$$dI = -\mu I dx \tag{2.15}$$

Solving equation 2.15 yields

$$I(x) = I_0 e^{-\mu x} \tag{2.16}$$

with $I(x)$ as the intensity after passing through a thickness x of the material and I_0 as the initial photon intensity.

For the energies used in radiotherapy with photons the energy deposition as a function of depth in tissue will increase to a maximum located a few cm inside the tissue and then decrease exponentially with increasing depth. This is shown in figure 3.1. The region in front of the maximum is known as the build up region because more and more secondary electrons are set in motion by the photons resulting in an increasing energy deposition up to the dose maximum which is located at a few cm depth in tissue.

2.2 Neutron Contamination of the Photon Beam

As mentioned in the introduction, neutrons are produced in radiotherapy through interactions of the primary beam particles with high-Z collimators or in the patient body. In this section, the theoretical basis of neutron production, and the propagation of neutrons through matter is discussed.

2.2.1 Neutron production through photon interactions

Neutrons are produced from photons through two different interactions known as evaporation and the direct knockout effect. When a nucleus as a whole is excited by a high energy photon, a neutron can be emitted (evaporated) in the de-excitation process. In the case of the direct effect, a photon interacts with the neutron in a nucleus and the photon energy is absorbed by the neutron resulting in the neutron being knocked out of the nucleus. Several nucleons can be emitted through photonuclear reactions, but most common at the energies used in radiotherapy is the emission of a single neutron. In order to calculate the required energy for the photon to kick out a neutron from the nucleus, the neutron separation energy, $s_n(Z, N)$ can be estimated. This is given by

$$s_n(Z, N) = B(Z, N) - B(Z, N - 1) \tag{2.17}$$

where B is the binding energy of the nucleus

$$B(Z,N) = Z \times m_{(^1H)} + N \times m_n - m(Z,N) \tag{2.18}$$

$m_{(^1H)}$ is the mass of a hydrogen atom and m_n is the neutron mass. Because high-Z materials like lead or tungsten are used as collimators for photon beams, the probability for lead nuclei photon interactions is quite large. The energy required for emission of a neutron from ^{207}Pb is from equations 2.17 and 2.18

$$s_n(82,125) = B(82,125) - B(82,124) \tag{2.19}$$

$$s_n(82,125) = m_n + m(82,124) - m(82,125) \tag{2.20}$$

$$s_n(82,125) = 1.008665\ u + 205.974440\ u - 206.975872\ u \tag{2.21}$$

$$u \approx 931.494\ MeV/c^2 \tag{2.22}$$

this gives

$$s_n(82,125) = 6.74\ MeV \tag{2.23}$$

Above the neutron separation energy, the cross section for neutron production increases with photon energy up to a maximum value and then decreases again with higher photon energies [4]. This peak in the cross section is known as the giant resonance. In most light elements, the giant resonance in the neutron production cross section is located between photon energies of 20 to 25 MeV. For heavier elements, the peak is located at lower energies, e.g. at 13.4 MeV for lead (see figure 2.5). Hence, neutrons can be produced in the treatment head of a medical linac and in the patient itself if the photon energy is sufficiently high. Collimators are the dominant source of neutron contamination because these are surrounding the photon producing metal target in the forward beam direction and are made from high-Z material.

The line marked with a "B" in figure 2.6 shows the relative energy of the top of the Coulomb barrier for protons. In the heavy nuclides, the top of the Coulomb barrier lies above the giant resonance, and the decay goes mainly by neutron emission because protons and charged particles in general cannot as easily as the neutrons cross the Coulomb barrier. Therefore, to a very good approximation, the sum of the neutron producing cross sections in the heavy nuclides is the total nuclear absorption cross section for photons [4].

With the introduction of IMRT in the late 1990s, the concern for neutron contamination has increased because this new technique involves an

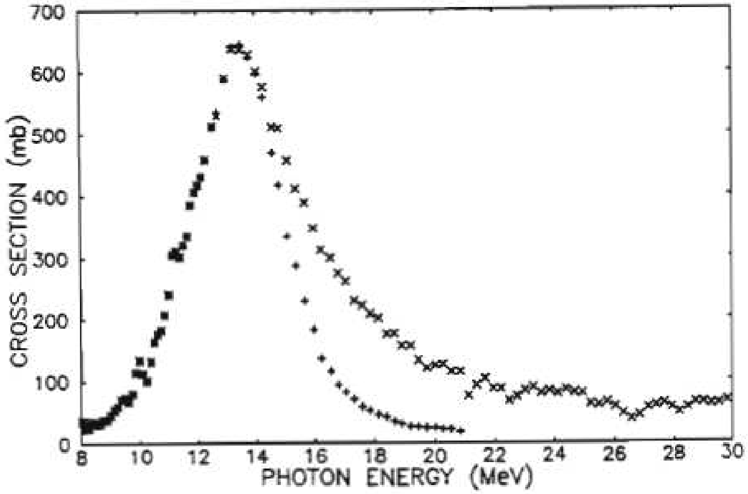

Figure 2.5: Giant resonance for ^{208}Pb. The (γ, xn) and (γ, n) cross sections are represented by crosses and plus signs, respectively. [4].

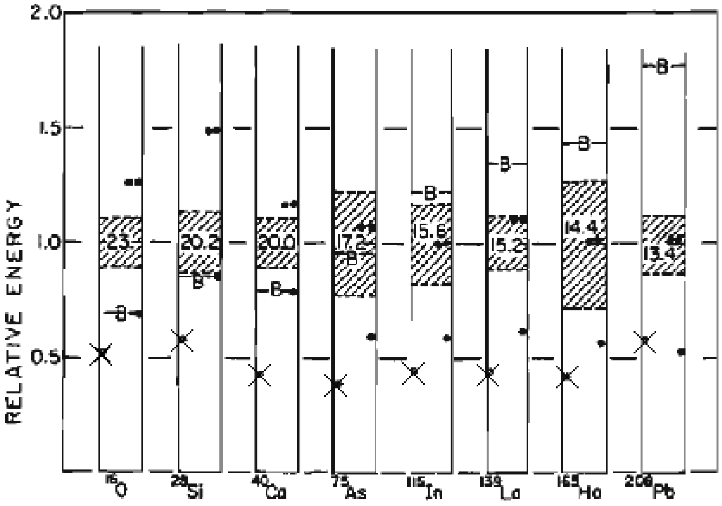

Figure 2.6: Giant resonance summary. The shaded areas indicate the width of the giant resonance, and the number gives the energy in MeV at the resonance peak. The energies have been normalized so that it is one at the giant resonance when looking at the scale for the y-axis. The circles shows the relative separation energy for one and two neutrons, and the crosses (x) marks the relative separation energy for protons [4].

Table 2.1: Relative isotopic abundances, neutron separation energies and lowest excited states for tungsten and lead [4].

Nuclide	Abundance[%]	S_n[MeV]	S_{2n}[MeV]	1st excited state[MeV]
^{180}W	0.1	8.41	15.30	-
^{182}W	26.3	8.06	14.75	0.100
^{183}W	14.3	6.19	14.25	0.047
^{184}W	30.6	7.41	13.60	0.111
^{186}W	28.6	7.20	12.95	0.123
^{204}Pb	1.4	8.40	15.30	-
^{206}Pb	24.1	8.09	14.82	0.803
^{207}Pb	22.1	6.74	14.82	0.570
^{208}Pb	52.4	7.37	14.11	2.610

extensive use of collimators and require more radiation output than conventional radiotherapy. In a medical linac, the radiation output is measured by ionization chambers placed in the photon beam (see figure 2.14). The ionization chambers measure the amount of charge released by the photon beam, and this is a measure of the photon beam's ability to ionize matter. The response from the ionization chambers is given in units of MU (Monitor Units), and the measured ionized charge is proportional to the deposited dose in a phantom or a patient. For an IMRT treatment, the number of monitor units applied is typically three times higher than in conventional treatment techniques. This implies that the production of neutrons will be higher in an IMRT treatment. It has been found that, independent of the treatment technique, the neutron production is proportional to the amount of monitor units applied [1].

The collimators in the medical linacs used at Haukeland University Hospital consists of lead and tungsten. As seen in figure 2.6 the giant resonance peak for ^{208}Pb is at 13.4 MeV, the (γ, n) threshold is 7.37 MeV and the $(\gamma, 2n)$ threshold is 14.11 MeV. For ^{184}W, which has the highest relative abundance of the tungsten isotopes in nature, S_n is 7.41 MeV and S_{2n} is 13.60 MeV. It follows from this that the 15 MeV photon beam used for experiments in this work will produce neutrons through both (γ, n) and $(\gamma, 2n)$ reactions. While the photon beam is efficiently collimated into the desired shape, the neutrons produced inside the treatment head are emitted approximately isotropic and penetrate the shielding in all directions. The only significant interactions for neutron moderation in the collimators are inelastic scattering and $(n, 2n)$ reactions [4].

Figure 2.7 and 2.8 show the interaction cross sections for neutrons in tungsten and lead. σ_{el} is the elastic scattering cross section, and $\sigma_{(n,n')}$ is the inelastic cross section. The sum of the inelastic and the $(n, 2n)$ cross sections is defined as σ_{non} (nonelastic cross section). It can be seen that

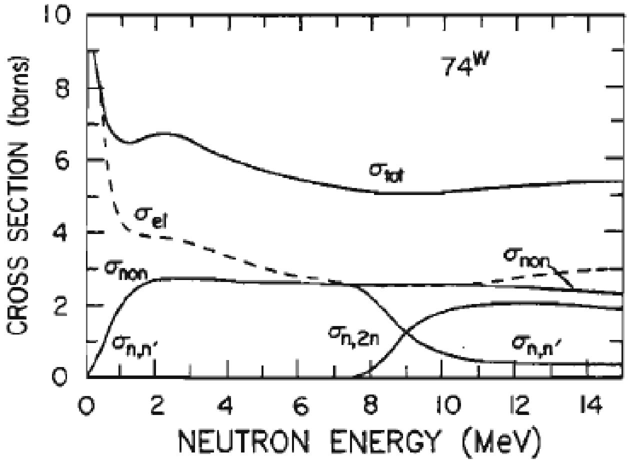

Figure 2.7: Neutron interaction cross section in natural tungsten as a function of neutron energy [4].

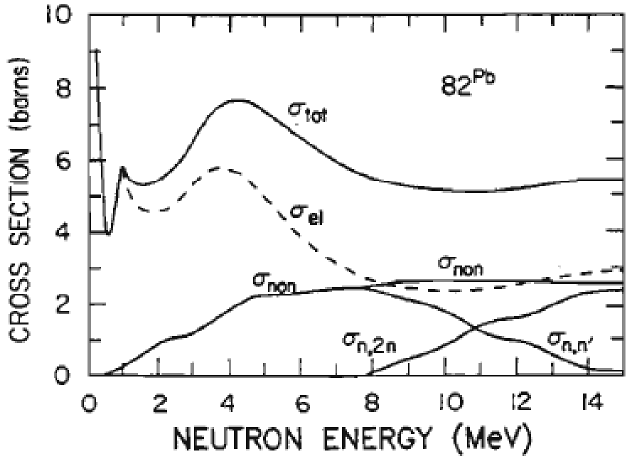

Figure 2.8: Neutron interaction cross section in natural lead as a function of neutron energy [4].

elastic scattering is the dominant interaction both in lead and tungsten at low neutron energies. Tungsten is more efficient than lead as a shielding material for neutrons, although the nonelastic cross sections are similar. This is because tungsten has 1.9 times more atoms per cm^3 compared to lead, and inelastic scattering in tungsten is possible at much lower energies than in lead. Inelastic scattering can only occur at energies above the lowest excited state of the shielding material. From table 2.1 it can be deduced that below 0.57 MeV, neutrons can only be moderated through elastic scattering.

2.2.2 Neutron spectra and attenuation

As mentioned in section 2.2.1, neutrons are produced from photons through two different interactions known as evaporation and the direct knockout effect. Neutrons originating from evaporation are emitted isotropically, while in the case of the direct effect, the distribution of neutrons is peaked in the direction of the incident photon. Simulations [5] show that a typical photoneutron spectrum from a medical photon linac consists of a dominant evaporation component with a peak in the energy interval 200 - 700 keV and a smaller direct effect component above 2 MeV. The simulated photoneutron spectrum from a 18 MeV photon linac is shown in figure 2.9.

The neutron spectrum in a treatment room will vary with the material in which the neutrons are produced and moderated. It will also depend on the surroundings as neutrons can be absorbed or reflected in the walls. In figure 2.10 the integral photoneutron spectrum for 15 MeV electrons striking a tungsten target can be seen. Also showed is the spectrum obtained when 10 cm of tungsten shielding surrounds the target, and the spectrum when the linac is situated in a concrete bunker. The spectra indicate that the amount of neutrons with energies above 10 MeV is low, and that the neutrons with energies of a few MeV or lower dominate the spectra. In addition, it should be noticed that when the neutron source is surrounded by a layer of high-Z material, the neutrons are moderated and hence the energy spectrum is shifted downwards.

From figure 2.11 and 2.12 it can be seen that the average neutron energy decreases almost exponentially with increasing shielding thickness when using lead or tungsten as shielding material. This is a good approximation for the material thicknesses used in medical accelerators. But as the neutron energy drops below the first excited state of the shielding nuclei, inelastic scattering will no longer occur, and the neutrons can only lose energy through elastic scattering. There will then no longer be an exponential decrease, and the average energy will remain close to constant through further shielding of the same material.

In a medical linac with all-tungsten shielding, as much as 15% of the neutron fluence might be absorbed, but in lead shielded medical linacs there would be essentially zero attenuation, or possibly even a build-up of neutron

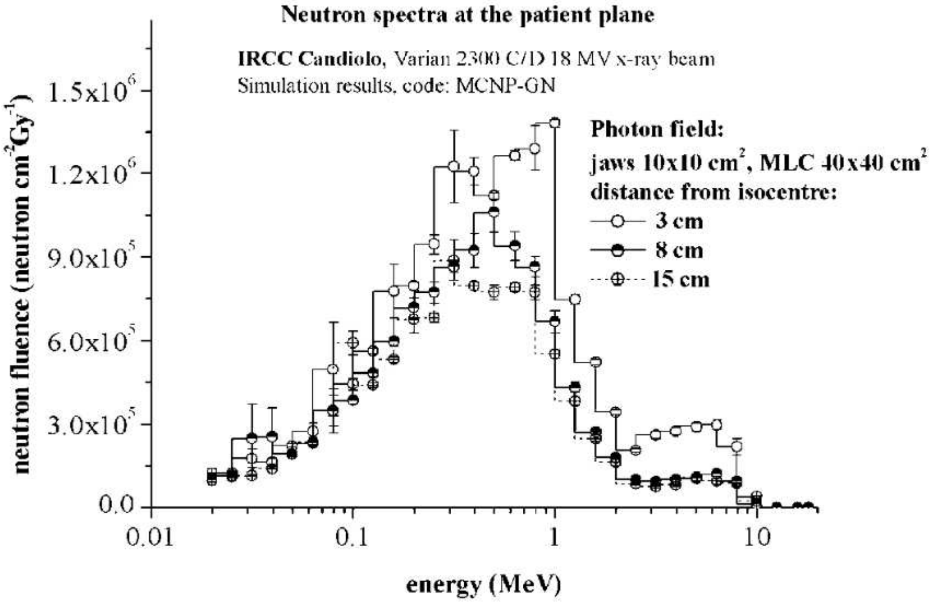

Figure 2.9: Neutron spectrum obtained from Monte Carlo simulations of neutrons from a 18 MeV medical linac [5]. Neutrons from evaporation dominate the spectrum and show a peak at approximately 0.5 MeV. The direct knockout effect contribution amounts to about 10% of the total fluence and is seen as the smaller peak in the spectrum with energies up to roughly 10 MeV.

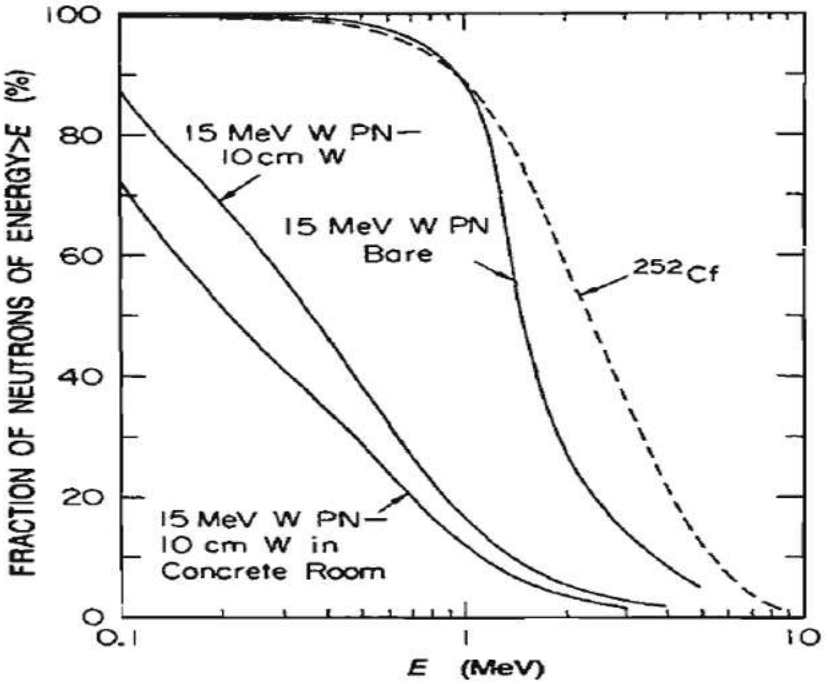

Figure 2.10: Integral photoneutron (PN) spectrum from 15 MeV electrons striking a tungsten target. In addition, the effect of 10 cm tungsten shielding around the target, and the effect of taking into account the concrete walls of the room are shown. A spectrum for fission of ^{252}Cf is also shown for comparison [4].

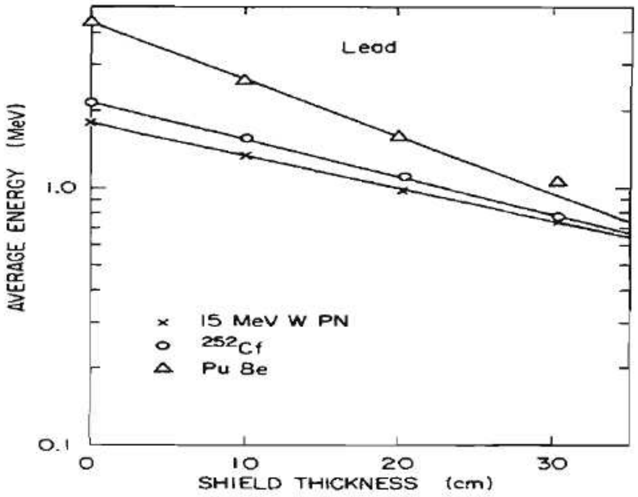

Figure 2.11: The average energy of neutron spectra as a function the thickness of lead surrounding the source is shown. The neutrons originate from 15 MeV electrons incident on a tungsten target and fission in ^{252}Cf and Pu-Be neutron sources [4].

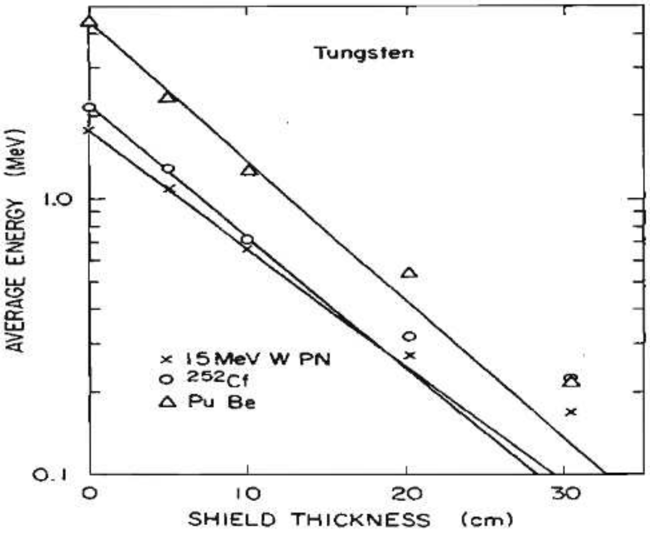

Figure 2.12: The average energy of neutron spectra as a function the thickness of tungsten surrounding the source is shown. The neutrons originate from 15 MeV electrons incident on a tungsten target and fission in ^{252}Cf and Pu-Be neutron sources [4].

fluence due to the (n,2n) reactions. While these shielding materials do not attenuate the neutron fluence significantly, they will moderate the neutrons and hence to some degree reduce the absorbed neutron dose for the patient.

2.3 Accelerators for Photon Radiotherapy

To produce photons with therapeutic energies, usually between 4 and 25 MeV, linear accelerators are used. In a linear accelerator, electrons are accelerated and sent to a target in which bremsstrahlung photons are produced. The medical linear accelerators (linacs) use high-frequency alternating voltage to accelerate electrons to energies in the MeV range. The linac has a moderator which delivers flat-topped DC pulses with a length of a few microseconds to an electron gun and simultaneously to a klystron or magnetron [3]. A block diagram of a typical medical linac can be seen in figure 2.13. From the klystron or magnetron, pulsed microwaves are transported to the accelerating structure through a waveguide. The electron gun injects electrons into the accelerating structure with timing correlated to the microwaves coming through the waveguide. As the electrons enter the accelerating structure, they are grouped together in bunches. The electric field from the microwaves will accelerate the electrons up to energies required for radiotherapy. When the electrons have passed the accelerating structure, they are sent to the treatment head guided and focused by bending magnets.

Most medical linacs have a gantry which makes it possible to rotate the treatment head 360° around the patient table. The gantry makes it possible to irradiate tumors from several angles. This is known as the “crossfire” technique, and can make it possible to irradiate the target volume with sufficiently high dose with tolerable damage in healthy tissue. However, this does not lower the integral dose to healthy tissue, but distributes it over a larger volume.

To produce a photon beam, a target of high-Z material such as gold plated tungsten is placed in the treatment head. When incident on this target, the electrons produce photons in the form of bremsstrahlung. The target itself is sufficiently thick to absorb most of the electrons. Figure 2.14 shows a typical design of a treatment head.

Because the electrons come in bunches, the photon beam will be a short pulsed beam. This causes problems when trying to measure neutrons with active detectors. The intense pulse will have the potential to saturate the readout of the detector, and the rather large dead time will inhibit the detector to be able to respond to each burst of neutrons coming from the pulsed electron beam. This is one of the main reasons why passive detectors often are preferred for neutron measurements in connection with medical linacs.

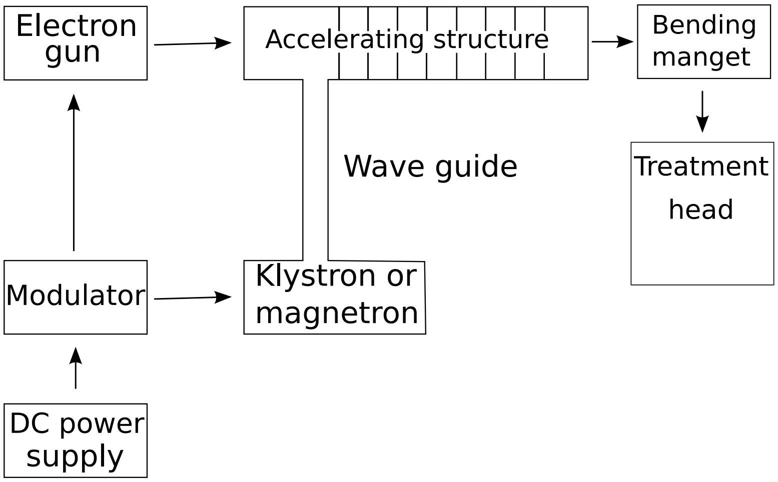

Figure 2.13: Block diagram of a medical linear accelerator.

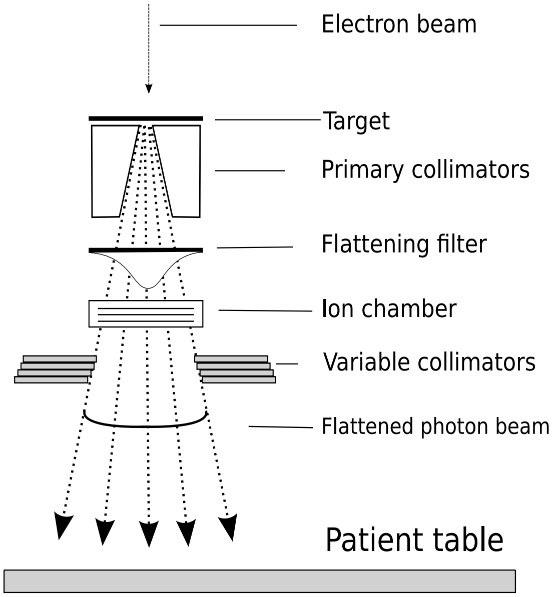

Figure 2.14: Sketch of a typical treatment head.

Chapter 3

Radiotherapy With Hadrons

As early as in 1946 the American physicist Robert Wilson published an article on the advantages in radiotherapy of the depth dose distribution of protons in tissue [6]. Since then, a variety of particles have been tested as alternatives to photons in radiotherapy. Pions, protons, helium ions and carbon ions are the particles which have been most widely used [7].

There are many considerations and factors involved in the choice of particles for radiotherapy. Heavy ions will efficiently damage cancer cells in deep seated tumors because of their high energy deposition in tissue at the end of their range. However, heavy ions will also be fragmented when passing through tissue, resulting in a mixed radiation field. Lighter particles such as protons have the advantage that they are easier to accelerate up to therapeutic energies, and the beam can not be fragmented into lighter elements. While the dose from photons reaches a maximum a few centimeters inside the tissue and then decreases exponentially, the dose from protons and ions will reach a maximum at the end of the particles range. This maximum is known as the Bragg peak. The depth dose curves, shown in figure 3.1, illustrates this. The depth dose curves also show a sharp fall of the dose behind the Bragg peak.

For deep seated tumors, it is evident that radiotherapy with protons or ions can confine the dose better to the tumor than radiotherapy with photons. Consequently, healthy tissue will receive less dose. For tumors located close to radiosensitive organs, it may in some cases not be justifiable to irradiate the target volume with the dose needed to treat the malignancy using photons due to the relatively slow fall of the depthdose curve for the photons. In such cases, particle therapy may give the possibility to apply sufficiently high doses in the target area and still give a satisfactory low dose to the critical organs. Today, protons and carbon ions are found to be the particles best suited for radiotherapy. However, it is not obvious that these are the best choices, and experiments with other ions are ongoing.

The number of particle radiotherapy facilities is still relatively low, but

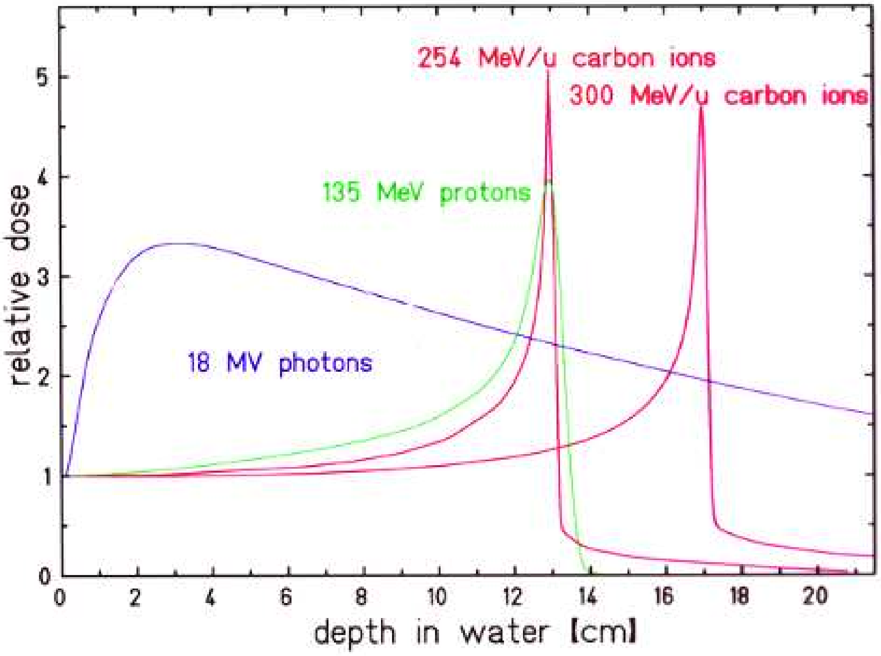

Figure 3.1: Depth dose distribution of photon, carbon and proton beams. In the case of photons, the dose decreases exponentially after a maximum a few centimeters inside the body. The proton and carbon beams have a relatively low entrance dose and have their dose maximum at the end of their range. This maximum is known as the Bragg peak [8].

the field is growing fast, and the demand for this treatment will continue to rise as systematic statistics for the clinical results are achieved. Although the potential of radiotherapy with protons and ions has been known for more than fifty years, it is in the last few decades that focus has started moving from research to treatment on a larger scale. Today, 29 centers are operational, while 23 facilities are on the list of planned particle therapy centers [7]. From this increase, it is may be deduced that there is an increasing interest for the use of radiotherapy with protons and ions on a larger scale. Until now, more than 60000 cancer patients have been treated using proton radiotherapy, and more than 5000 patients have been treated with carbon-ions. An overview of particle therapy facilities in operation and under planning is shown in appendix A.

3.1 Interaction of Charged Particles With Matter

Charged particles traversing through matter lose energy primarily through inelastic collisions with atomic electrons causing excitation and ionization of the atoms. A heavy charged particle, like the proton or a carbon ion, transfer only a small fraction of its energy in a single collision with an atomic electron, and is only to a small degree deflected from its initial path. Thus, a heavy charged particle can propagate along an almost straight path through tissue leaving ionized and excited atoms along the track. The particle energy, and thus the velocity, is reduced by a small amount in each collision. As the velocity decreases, the energy loss per length will increase resulting in maximum energy deposition at the end of the particles range, i.e. in the Bragg peak.

3.1.1 The Bethe-Bloch equation

Energy loss of charged particles by ionization and excitation of atoms in matter is described by the Bethe-Bloch formula [2]. Equation 3.1 shows the Bethe-Bloch formula for heavy charged particles like protons and ions. The last two terms are corrections to the equation and take into account the density effect and shell corrections.

$$-\frac{dE}{dx} = 2\pi N_a r_e^2 m_e c^2 \rho \frac{Z}{A}\frac{z^2}{\beta^2}\left[ln\left(\frac{2m_e\gamma^2 v^2 W_{max}}{I^2}\right) - 2\beta^2 - \delta - 2\frac{C}{N}\right] \quad (3.1)$$

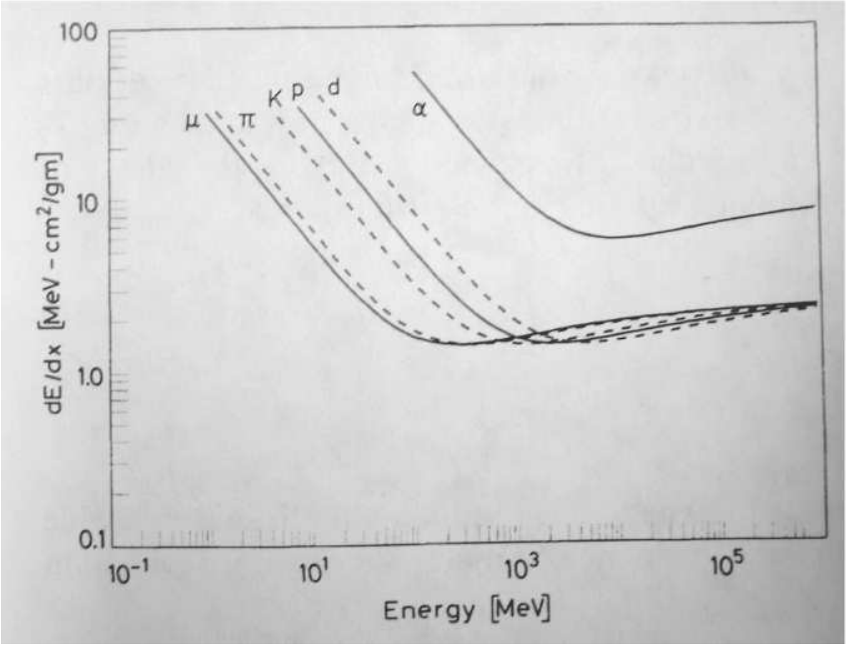

Figure 3.2: The stopping power dE/dx as function of energy for different particles. This plot is based on the Bethe-Bloch equation [2].

Table 3.1: Factors involved in the Bethe-Bloch equation [2].

N_a	Avogadro's number
r_e	Classical electron radius
m_e	Electron mass
ρ	Density of absorbing material
Z	Atomic number of absorbing material
A	atomic weight of absorbing material
z	Charge of incident particle in units of e
β	$\frac{v}{c}$ of the incident particle
γ	The Lorentz factor
W_{max}	maximum energy transfer in a single collision
I	mean excitation potential
δ	Density correction
C	shell correction

In particle therapy, the particles will have a high initial velocity when penetrating the body, resulting in a short interaction time and only a small amount of energy is transferred to the tissue. As the particles are gradually slowed down the local interaction time becomes longer resulting in that most of the particles energy is deposited at the end of their range. The main dependencies of energy loss, which should be noticed from equation 3.1, is that the energy loss is dependent on the square of the particle charge (z) and on the velocity (β) of the particle. High charge and low velocity gives a high energy loss, dE/dx.

3.1.2 Lateral scattering

One of the advantages of particle therapy is the possibility to use very narrow beams referred to as pencil beams. Irradiating patients with pencil beams makes very high precision in the treatment possible. However, particle and photon beams will always be broadened as they pass through tissue. Figure 3.3 illustrates that lateral scattering is less for carbon ions compared to that of protons. The low degree of lateral scattering allows accurate irradiation adjacent to critical radiosensitive organs by the use of carbon ions.

3.1.3 Neutron production and fragmentation

Although the carbon ions stop at or immediately after the Bragg peak depth in tissue and to a small degree are scattered laterally, secondary particles produced from the primary ions will contribute to undesired dose deposition outside the target volume.

The most frequently occurring nuclear reactions in radiotherapy with carbon ions are peripheral collisions, where the primary carbon ions lose one

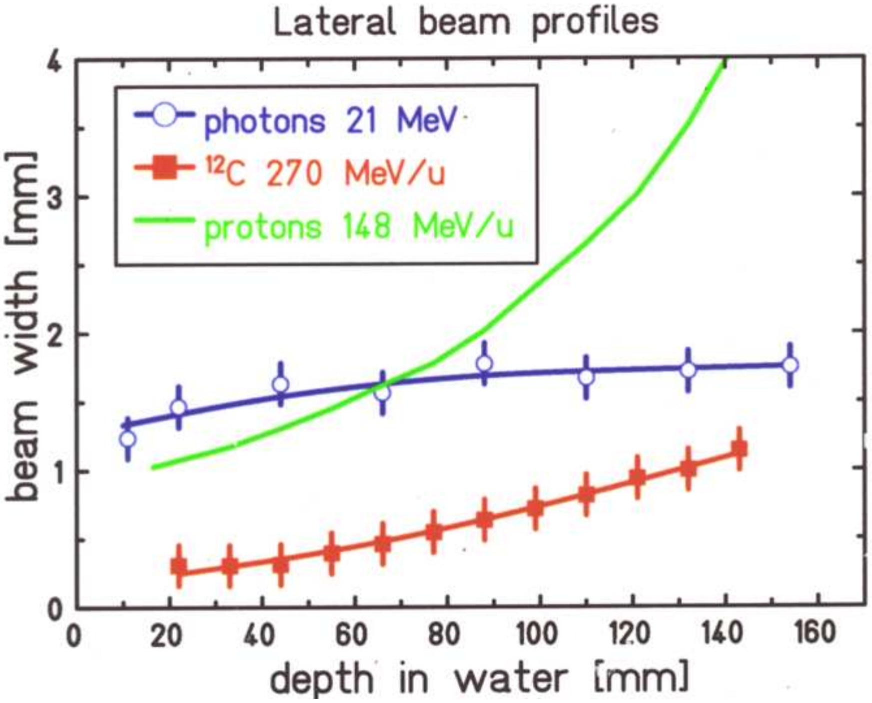

Figure 3.3: Lateral beam profiles for protons, photons and ^{12}C ions as a function of depth in water [8].

or several nucleons. This interaction is described by the abrasion-ablation model which is shown in figure 3.4. Nucleons in the overlapping zone of the projectile and target nuclei are abraded and form the reaction zone known as the fireball. The outer nucleons are less affected by the collision and are referred to as spectators. The remaining projectile and target fragments, as well as the fireball, de-excite by evaporating nucleons and light clusters.

Particles emitted from the projectile fragments have a forward peaked distribution due to the high velocity of the projectile. Neutrons and clusters originating from the target are emitted isotropically and with much lower velocities. This leads to a build-up of lower Z fragments with increasing depth. Because the range of particles is proportional to A/Z^2, where A is the atomic weight and Z is the charge, the fragments will have longer ranges than the primary ions. Consequently, the depth dose distribution of a heavy ion beam includes a characteristic fragment tail beyond the bragg peak of the primary ions [9]. This is in contrast to a proton beam where production of lower Z fragments is not possible. Both proton and carbon depth dose distributions are shown in figures 3.5 and 3.1.

The energy of fragments extends up to the initial beam energy per nucleon. For neutrons and protons produced from a 200 MeV/u ^{12}C beam, the energy of the neutrons and protons can be up to twice the initial energy per nucleon of the carbon ions. This can be explained by the transfer of the Fermi-momentum of target nucleons during the collision. The proton and neutron energy spectra are similar at all angles, while the fragment distribution is more forward peaked. At large angles, the neutron emission becomes close to isotropic because these neutrons originate from the evaporation process. At smaller angles, the energy distribution have a broad maximum at about half of the projectiles energy per nucleon. This is related to the beam energy, because the neutrons emitted at small angles are mainly produced by projectile abrasion. Thus, these neutrons have energies close to the beam energy at the moment of nuclear interaction and are therefore forward peaked [9].

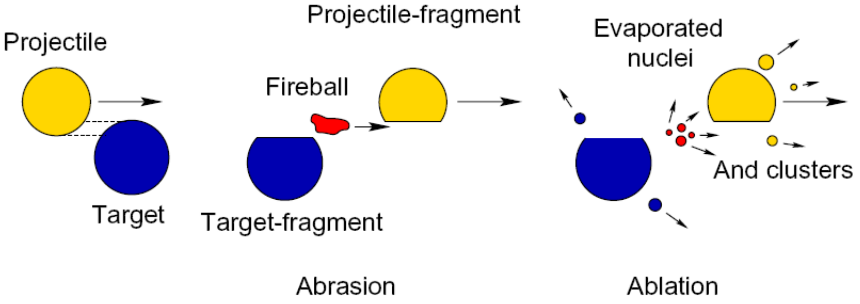

Figure 3.4: Illustration of nuclear fragmentation due to peripheral collisions of projectiles (carbon ions) and target nuclei (nuclei in the body) [9].

3.2 Principles of Particle Therapy

Figure 3.5 illustrates the basic principle of particle therapy and its main advantages compared to radiotherapy with photons. As mentioned, particle dose distributions reach a maximum at the end of the particles range. If a target volume is defined as the shaded area in figure 3.5, a monoenergetic particle beam will only cover a small area of the tumor. This is because the Bragg peak is relatively narrow, but if the energy of the particle beam is lowered, the range is also reduced. Consequently, if the energy, as well as the intensity of the beam, is gradually decreased, a series of overlapping Bragg peaks can add up to a homogenous dose deposited over the whole tumor. This is shown by the black curves in figure 3.5. The sum of the overlapping Bragg peaks is known as the Spread Out Bragg Peak (SOBP) and is shown both for carbon ions and protons in the illustration.

As discussed in section 2.3, it may be an advantage to irradiate the tumor from several angles to reduce the dose to critical organs in the area. This is also advantageous in particle therapy in many cases. However, because

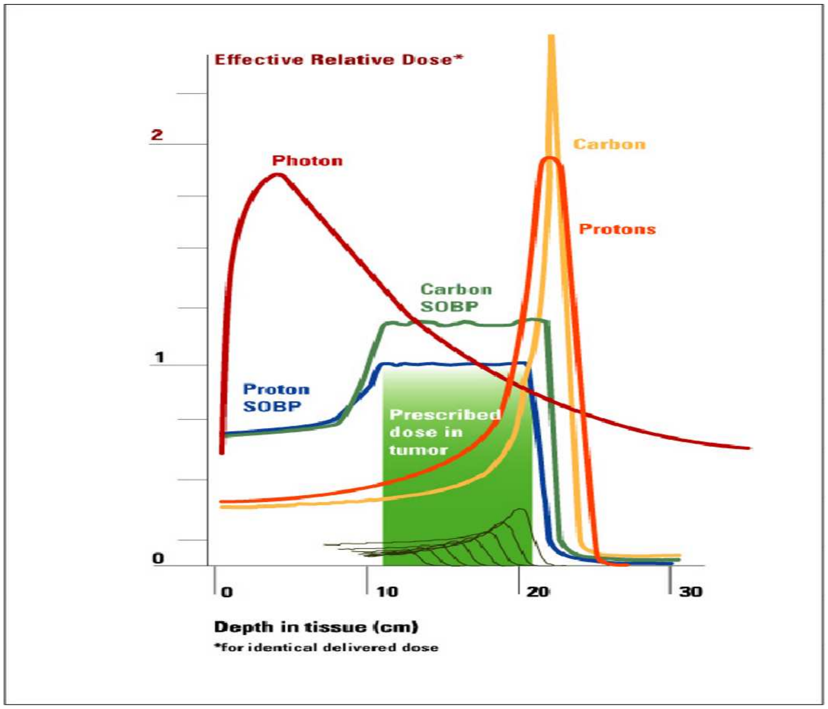

Figure 3.5: Depth dose curves for photons, protons and carbon ions. By varying the energy, the range of the particle beams can be shifted. The black curves at the bottom show a series of proton depth dose curves for different energies. A particle beam consisting of a wide range of energies (the black curves) will give a Spread Out Bragg Peak (SOBP) which may cover a large area in contrast to the narrow Bragg peak of a monoenergetic beam [10]. Compared to photon radiotherapy, it is clear that the confinement of dose to the target volume is better for proton and carbon beams.

protons and ions are much heavier particles than electrons, they require higher energies and larger installations for acceleration and beam focusing. This complicates the process of changing the beam direction. For proton therapy centers, it is feasible to use gantries, and it is becoming a standard that new proton facilities have at least one treatment room with a gantry. For carbon facilities however, the construction of a gantry is extremely costly and might not be the best solution. At the carbon ion therapy center in Heidelberg, the world's only heavy ion gantry has been built. With a weight of 600 tons, the gantry is a huge construction, and it is likely that other solutions with flexible movement of the patient table relative to a fixed beam direction will be preferred by most ion therapy center in the near future. A flexible solution may be to have treatment rooms with fixed ion beams and treatment rooms with proton gantries in the same facilities.

3.3 Relative Biological Effectiveness

Because radiation of different beam particle qualities deposits energy in tissue in various ways, the same physical dose can lead to different biological effects depending on the type of radiation. The fact that the carbon ion has a 6 times higher charge than the proton indicates that carbon ions can more densely ionize tissue than protons. This is because the energy loss in tissue is strongly dependent on the charge of the particle. The typical number of protons applied in a treatment will be much higher than that of carbon ions, but at a microscopic level, the ionization will be more spread out in proton therapy leading to more repairable DNA damage. In general, it is believed that radiation with the ability to densely ionize tissue will give a higher biological effect than sparsely ionizing types of radiation, e.g. photons. Figure 3.6 illustrates how the ionization density increases along a carbon ion track as the energy decreases. The picture at the bottom shows ionization from a carbon ion with an energy of 10 MeV per nucleon. The illustrations above show ionization from protons and carbon ions with energies of 1 and 0.5 MeV per nucleon [11].

The biological effect of radiation has been studied in cell experiments in order to look into the difference in cell survival after irradiation with carbon ions, protons and photons. For typical energies in the entrance channel of a carbon treatment, the cell survival, and thus the biological effect, is found to be close to that of photons [11]. In the last 2 cm of the carbon ions range, the Bragg peak area, the cell survival rate is found to be significantly lower. This would correspond to a 3 times higher biological effect in tissue compared to that of the same physical dose from photons. In other words, 3 times more physical dose would have to be applied to achieve the same biological effect with photons compared to that of carbon ions. Other ions have been found to have similar properties. Ions heavier than carbon, e.g argon and neon have been used for radiotherapy at Berkeley, and has shown high tumor control rates. However, for the argon and neon ions the biological effectiveness is very high already early in the entrance channel resulting in a high biological dose also in healthy tissue. The many late effects in normal tissue related to argon and neon ion treatment is the main reason why these are not used for particle therapy at present time.

For protons, cell experiments have shown that high biological effectiveness is achieved only for the last few micrometers of the particles range. For clinical use, the biological effect of proton therapy has been found to be approximately 15% higher than that of the same absorbed dose applied with photons [11].

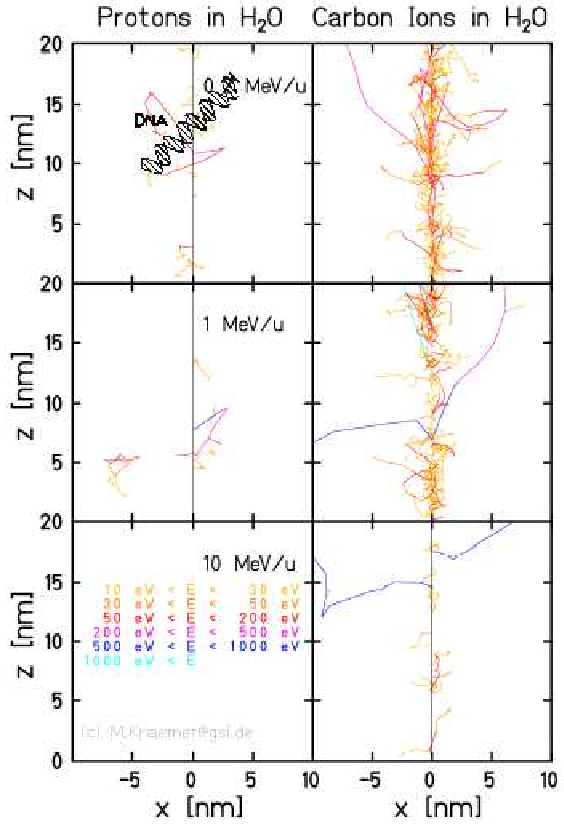

Figure 3.6: Illustration of the ionization density along the primary particle tracks for protons and carbon ions [11]. The tracks of electrons liberated by the particles is shown. These produce biological damage in the tissue. As the energy decrease from 10 MeV/u to 1 MeV/u and 0.5 MeV/u it can be seen that the ionization increases. The sketch of a DNA molecule is shown to illustrate the order of magnitude of the ionization tracks.

3.4 Accelerators for Particle Therapy

Compared to electrons, which are accelerated in radiotherapy with photons, far more energy is needed to accelerate protons and ions to therapeutic energies. Linear accelerators can in principle reach arbitrarily high particle energies, but the length and hence the cost of the machine grows with the energy. It is therefore desirable to drive the particles around a circular path and so use the same accelerating structure many times for the same particles.

The carbon ion therapy centers today use synchrotrons to achieve the desired particle energies. A synchrotron ring consists of an almost circular vacuum beam line with dipole and quadrupole magnets positioned around the orbit. These magnets are used for bending and focusing the beam. Particles gain energy by passing through one or more accelerating cavities made from RF generators. The synchrotron principle is shown in figure 3.7. Synchrotrons are not able to accelerate particles with no initial kinetic energy. The reason for this is that it is not possible to increase the strength of the magnetic fields linearly and precisely enough from zero magnetic field [12]. This is why synchrotrons also require a linear accelerator or a cyclotron connected to the synchrotron ring. An alternative to synchrotrons is the superconducting cyclotron. This is a more compact solution, as superconducting cyclotrons of about 6 meter diameter are capable of supplying therapeutic beams of protons as well as heavy ions [10].

The conventional cyclotron (figure 3.8) is currently used in proton therapy and is commercially available from several manufacturers. To make the particles follow a circular path, the cyclotron uses an iron magnet which produces a homogeneous magnetic field with a typical strength of a few Tesla. The particles circulate in a plane between the poles. A vacuum chamber is placed between the poles of this magnet. This also contains two D-shaped electrodes, often referred to as DEEs, which are needed for particle acceleration. The particles are emitted from an ion source in the center, and between the two halves a RF voltage is applied. As the particles pass through the gap between the DEEs, they are accelerated and continue along a new circular path with a larger radius [12].

3.5 GSI-Darmstadt

GSI (Gesellschaft für Schwerionenforschung) is a facility for research in fundamental physics and especially heavy ion research. Since 1997, GSI has been operating a radiotherapy unit for cancer treatment using carbon ions. Today, more than 400 patients have been treated for tumors in the head and neck region. Also patients with tumors along the spinal cord and prostate cancer have been treated at GSI. The cancer therapy at GSI has been a pilot project and has never been intended to be a large scale treatment fa-

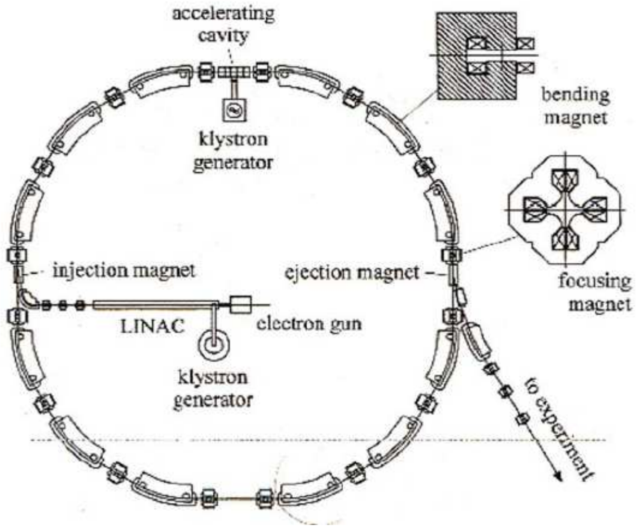

Figure 3.7: Synchrotrons are used for accelerating carbon ions to energies needed for radiotherapy. The magnetic field varies and increases, as the name suggests, synchronous with the particle energy. A linear accelerator is needed to give the particles some initial energy before they are sent into the synchrotron ring.

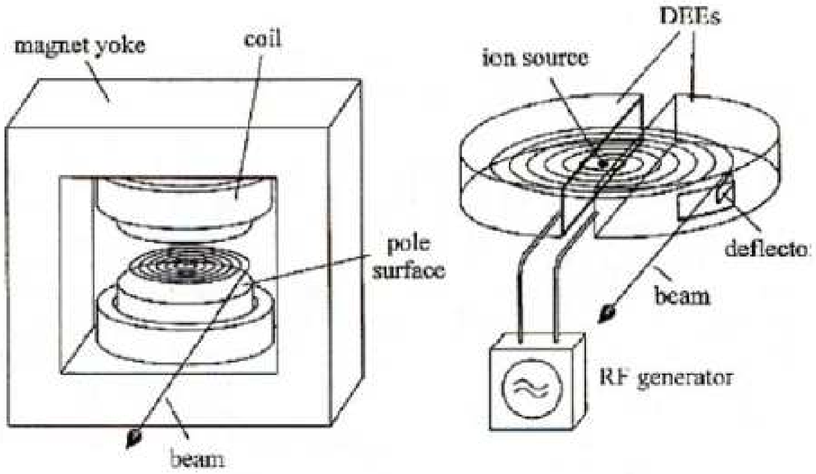

Figure 3.8: The cyclotron is used as accelerator in proton therapy facilities. A constant magnetic field is applied and the radius of the particle track increases with energy [12].

cility. Knowledge and experience is now being transferred to an ion-beam radiotherapy center built in Heidelberg which is expected to treat more than 1000 cancer patients annually.

3.5.1 Intensity Modulated Particle Therapy

Ions and protons are charged particles and can thus be deflected by the use of magnetic fields. This gives the possibility to use a narrow beam for radiotherapy and deflect the beam horizontally and vertically by the use of dipole magnets. The range of the particles can be adjusted by varying the energy of the beam. At GSI a system known as the raster-scan technique (figure 3.9), based on this principle is used. The target volume is dissected in slices and each slice is covered by a grid of pixels. A slice is irradiated pixel by pixel. When all pixels have been irradiated, the beam energy is changed, and consequently the particle range, and a new slice can be irradiated. During irradiation of the most distal layers, the proximal layers will also receive some dose, and this must then be corrected for and yields in general an inhomogeneous particle distribution for all individual layers [11].

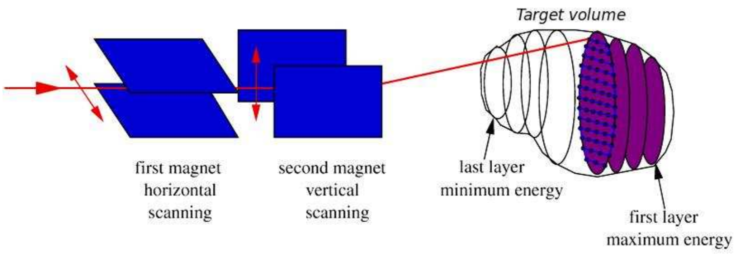

Figure 3.9: Intensity modulated radiotherapy by the raster-scan principle. The target volume is divided into slices. Each slice is covered by a grid of pixels which are irradiated in a row-by-row pattern by the carbon beam. Dipole magnets are used for beam steering [11].

3.5.2 Online PET scan with ^{12}C beam

A carbon beam passing through tissue will continuously be fragmented through nuclear reactions. This results in a mixed radiation field, where dose contributions from various fragments will occur also outside the target volume. Some of the fragments produced are the radioactive isotopes ^{10}C and ^{11}C with half lives of 19 seconds and 20 minutes, respectively [11]. Equations 3.2 and 3.3 show the decay process of ^{10}C and ^{11}C. These isotopes are both β^+ emitters, and the annihilation of these positrons produces two gamma-rays which can be detected outside the body using a Positron

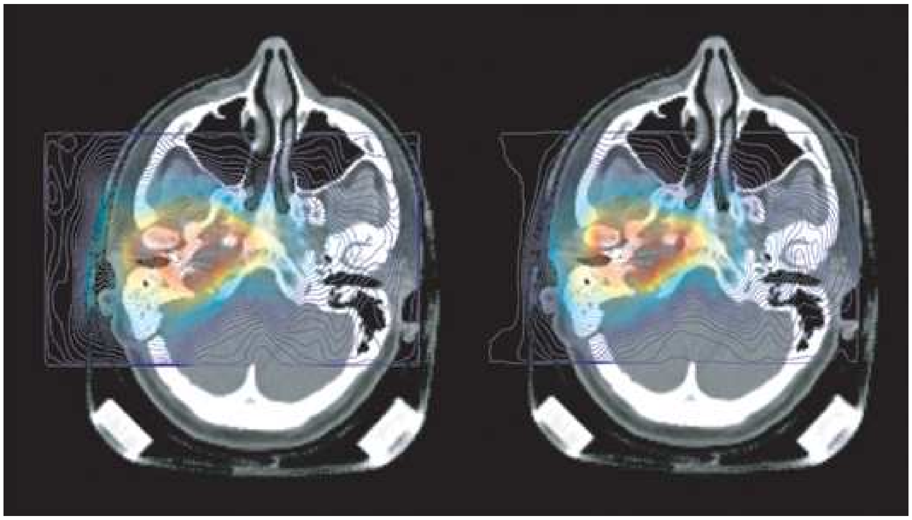

Figure 3.10: The PET analysis visualizes the irradiation inside the patient. From the doseplanning, a distribution of positron activity can be predicted (left). The figure on the right shows the measured positron activity during irradiation. Both PET images have been projected onto a CT-picture. By comparing the two images, it can be confirmed whether or not the planned dose distribution was achieved [13].

Emission Tomography, PET-camera. The ^{10}C and ^{11}C isotopes are stopped nearly at the same position in the patient as the primary carbon ions, and the positrons emitted have a very short range of only a few millimeters. This gives an excellent opportunity to confirm the range and control the beam. The PET system is especially important in cases where irradiation with a longer range than estimated could cause damage to critical organs.

$$^{10}C \longrightarrow \; ^{10}B + e^{+} + \nu_e \tag{3.2}$$

$$^{11}C \longrightarrow \; ^{11}B + e^{+} + \nu_e \tag{3.3}$$

Figure 3.10 illustrates use of the online PET scan. The expected positron activity from an irradiation can be estimated. This can be compared to the activity detected by the PET camera to see if the dose was distributed according to the treatment plan.

3.5.3 Moving targets

Due to the high biological effectiveness and the level of precision possible to obtain in particle therapy, high radiation doses are applied in the target volume with sharp dose gradients to normal tissue on the distal side of the tumor. Hence, the consequences of errors in positioning or other factors leading to unnecessary irradiation of normal tissue can be more severe than in photon radiotherapy. For many tumor sites, it is a problem that the tumor can not be completely immobilized during irradiation. For example, tumors in the pelvic and the thorax region may move significantly as a result of breathing and the heart beat.

Research is currently being conducted on how to in a safe way irradiated tumors which are difficult to immobilize, referred to as moving targets. The first and easiest step in treating these types of tumors is the gating technique. Using this method, the breathing cycle is controlled and the patient irradiated in a certain time interval, e.g. only when the lungs are empty.

Because the gating technique will cause a substantial increase in the treatment time, other more sophisticated techniques are also being investigated. If the motion of the tumor as a function with time is known, the beam can be adjusted correspondingly in the lateral direction by using the scanner system. For corrections of the particles range, the accelerator system can not at present time, change the energy fast enough to follow the variations in the target depth. A passive wedge system has been developed at GSI to be able to rapidly vary the beam energy and consequently, the range. Two wedges are mounted on linear motors which can be moved with high velocity against each other. Then, the thickness of this absorber, and accordingly, the range of the beam can be shifted. Tests of the double wedge system combined with the raster scan show promising results, but it will take time to implement the system in the patient treatment [11].

It should be mentioned that the introduction of the wedge system is a step away from the collimator free system which is a part of what makes particle therapy with beam scanning favorable. As in the body, the primary beam will be fragmented in the wedges, and the effect of this needs to be investigated.

Chapter 4

Dosimetry

Radiation dosimetry is the field where the aim is to quantitatively relate measurements in environments where radiation is present to biological changes that the radiation can induce in a target volume. Radiation interacting with the human body will directly or indirectly excite and ionize atoms and molecules. Secondary electrons from ionization will produce further excitations and ionizations until their energies fall below the thresholds for excitation of atoms in the medium. Measurements of ionization and energy deposition is the basis for radiation dosimetry. Dose deposition from the photon and hadron treatment modalities is also described briefly in this chapter.

4.1 Dosimetric Quantities

4.1.1 Absorbed dose

The absorbed dose, D, is defined as the energy, ΔE, which is deposited per mass unit in a small mass, Δm.

$$D = \frac{\Delta E}{\Delta m} \tag{4.1}$$

The unit for absorbed dose is the Gray [Gy].

$$1\ Gy = 1\ \frac{J}{Kg} \tag{4.2}$$

The old unit for absorbed dose is the rad (radiation absorbed dose), and 1 Gray equals 100 rad. In the radiation protection context, absorbed dose to a specific organ is denoted D_T and is given by

$$D_T = \frac{E}{m_T} \tag{4.3}$$

where m_T is the mass of the specific organ and E is the total energy absorbed from radiation in this organ. The disadvantage of this definition is that it gives the impression that the dose has been uniformly distributed throughout the organ. The damage from radiation will depend strongly on how the energy is absorbed in the tissue. Hence, two cases with the same total absorbed dose can give different biological effects depending on the distribution of dose within the organ.

4.1.2 The biological effects of ionizing radiation

The process of ionization changes atoms and may thus alter the structure of the molecules containing them. Molecular changes can also be caused by the excitation of atoms and molecules if the excitation energy exceeds the binding energy between atoms. If the affected molecules are in a living cell, the cell itself may occasionally be damaged, either directly if the molecule is critical to the cell's function, or indirectly by causing chemical changes in nearby molecules [14].

Radiation can cause various forms of damage in a human cell, but damage in the cell's DNA, which contains the complete genetic information, is by far the most important. Damage in the DNA may prevent the survival or reproduction of the cell. Figure 4.1 illustrates how ioniziong radiation can damage the DNA of a cell. Because the integrity of the DNA is essential for survival of the cell, and the complete organism, a very efficient repair system protects the integrity of the DNA. Thus, in many cases the cell is able to repair itself. Only if a high local ionization density produces many DNA-lesions close together, the cell repair mechanism may fail, and the cell loses its ability to divide (clonogenic death), or the cells are forced to destroy themselves (apoptotic death) [11]. A modified somatic cell can retain its reproductive capacity and give rise to a clone of modified cells that may result in a cancer. From this it is clear that in radiotherapy it is essential to, as far as possible, avoid irradiation of healthy tissue which could lead to late effects like secondary malignancies.

The biological effect depends not only on the absorbed dose, but also on the type of radiation. Biological damage caused by radiation varies with radiation type and with the energy of the specific radiation. A quantity related to the biological effectiveness is the linear energy transfer (LET). The LET is a measure of the energy locally deposited per unit path length [2]. For most situations in radiotherapy, this is the same as dE/dx (energy loss per length), but it should be noted that energy loss by emission of bremsstrahlung is not included in the LET because this energy is not in general deposited in the region of the particle path.

The LET value is thus a measure of the ionization density along the particle track, and as mentioned in section 3.3, the biological effect of radiation is correlated to this. In dosimetry, the relative biological effectiveness (RBE)

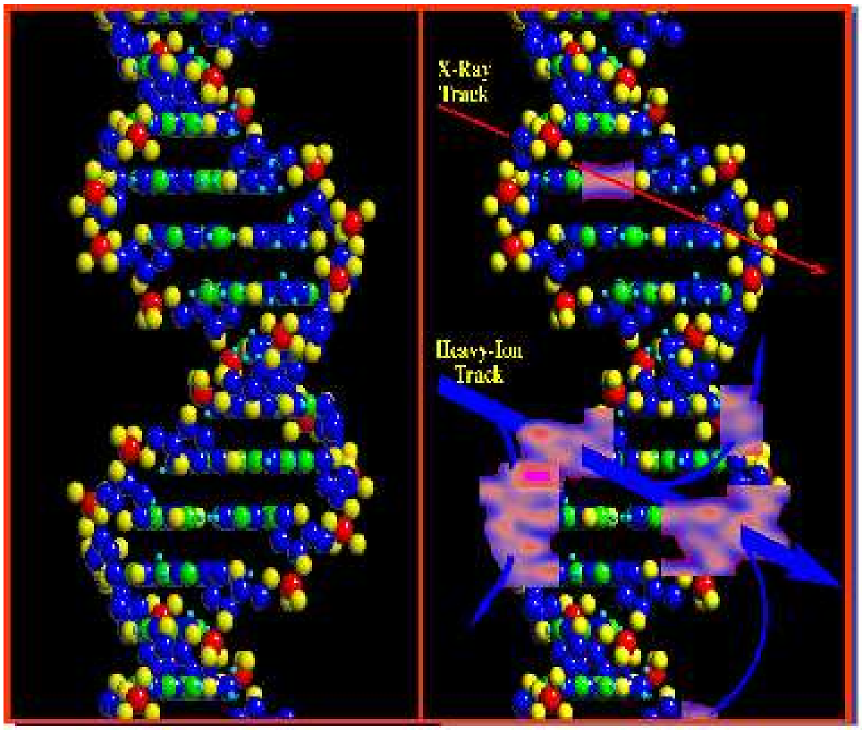

Figure 4.1: Illustration of a DNA molecule hit by sparsely ionizing photon and a densely ionizing heavy ion [15]. The ion is more likely to cause double-strand breaks which may lead to death of the cell.

Table 4.1: Quality factors, Q, showing the difference in biological effectiveness between the different types of radiation [14].

Radiation	Energy interval	Quality factor
Photons	All energies	1
Electrons	All energies	1
Protons	$E_p > 2$ MeV	5
α-particles	All energies	20
^{12}C and other heavy ions	All energies	20
Fission fragments	All energies	20
Neutrons (n)	$E_n < 10\ keV$	5
n	10 keV $< E_n <$ 100 keV	10
n	100 keV $< E_n <$ 2 MeV	20
n	2 MeV $< E_n <$ 20 MeV	10
n	$E_n > 20$ MeV	5

can be taken into account by applying a dimensionless weighting factor, w_R, which indicates the relative biological effectiveness based on radiation type and energy. Table 4.1 shows the most important weighting factors. The use of weighting factors is of course a simplification of the truth. The actual biological effect of radiation is dependent on many factors involving particle composition, dose deposition, particle energy, charge and from the biological side, the repair capacity and size of the cell nucleus of the affected tissue.

4.1.3 Equivalent dose

The equivalent dose, H_T gives a normalized measure of the biological effect on tissue from irradiation. It takes into consideration which type of radiation the tissue, or an organ, is exposed to, and it is calculated by multiplying the absorbed dose, averaged over the entire tissue or organ, by the radiation weighting factor. Thus

$$H_T = w_R \times D_R, \tag{4.4}$$

where D_R is the average absorbed dose received by organ R, and w_R is the radiation weighting factor. This factor is sometimes also referred to as the quality factor, Q, for the radiation. In the case of several types of radiation present, absorbed doses from each radiation type is multiplied by the corresponding weighting factors and finally they are added together. In this case the equivalent dose is given by

$$H_T = \sum_R w_R \times D_{T,R} \tag{4.5}$$

$D_{T,R}$ is the average absorbed dose received by organ T from the radiation type R. The unit for equivalent dose is the Sievert (Sv). An older unit for equivalent dose is the rem (1 Sievert = 100 rem).

4.1.4 Effective dose

Whole body exposures to radiation are rarely uniform. The equivalent dose received may vary considerably from one organ to another. Also, the effect of radiation is found to depend on the specific organ or tissue receiving the radiation. To take this into account, dimensionless tissue weighting factors, w_T, are defined for various organs of the body. The effective dose, E, is defined as

$$E = \sum_T w_T \times H_T, \tag{4.6}$$

where the equivalent dose to each organ and tissue is weighted by its individual factor w_T and then the sum over all tissues and organs is taken. The effective dose is, like the equivalent dose, measured in units of Sievert, and it has been found to give a better indication of the effects of radiation to specific organs.

4.2 Dose deposition

The dose deposited in the body through radiotherapy varies with the particles applied. As described earlier, particles passing through tissue deposits dose by, directly or indirectly, causing ionization of atoms. The main interactions of photons, protons and ions with matter are discussed in sections 2.1 and 3.1. These interactions are the basis for energy, an thus, dose deposition in tissue. During photon radiotherapy, secondary electrons produced by the photon interactions, will cause ionization in tissue and therefore dose deposition in the body. For this reason photons are often referred to as indirectly ionizing, in contrast to protons and ions which directly ionize the atoms in tissue. As briefly mentioned in section 2.1.4, when a photon beam traverses through matter, the dose deposition will increase with increasing depth in a build up region up to the maximum dose located a few cm inside the tissue depending on the photon beam energy. Although the photon intensity is highest initially, more and more electrons will be set in motion causing ionization as they propagate through the tissue. The photon intensity decreases exponentially and at some point, the amount of ionization, or dose deposition, begin to decrease as fewer ionizing electrons have been released due to the lower photon intensity. This point is the dose maximum of the depth dose curve in radiotherapy with photons.

The dose deposition from protons and ions is caused by the ionization produced along the particles tracks as they propagate through tissue, and the secondary ionizations from electrons liberated in this process. The directly ionizing properties of e.g. carbon ions, results in a more densely deposited dose which more efficiently damages cells compared to photon radiation, which is known as sparsely ionizing.

4.2.1 Dose deposition from neutrons

Fast neutrons passing through tissue will scatter mainly elastically, but also inelastically back and forth between the nuclei, losing energy until the energy is in the order of 0.025 eV. The neutrons are then said to be thermalized because they are in thermal equilibrium with the surrounding atoms [2]. In elastic scattering, the total kinetic energy is conserved in the interaction, and hence, the energy lost by the neutron is equal to the kinetic energy of the recoil nucleus. When inelastic scattering occurs, the nucleus absorbs some energy internally and is left in an excited state. The neutron can also be captured, or absorbed by a nucleus resulting in reactions such as (n,p), (n,2n), (n,α), or (n,γ) [16].

Neutrons may be captured or undergo nuclear reactions before they are thermalized, but at thermal energies, the neutrons will diffuse through matter until captured by a nucleus or until a nuclear reaction takes place. When energy from neutrons is transferred to charged particles through scattering, a light nucleus will in general absorb more of the neutrons energy than heavier nuclei. This is the reason why hydrogenous materials such as water and paraffin (CH_2) are effective neutron moderators. In tissue charged particles absorbing energy from neutrons through scattering will contribute to dose by ionization and exciting in the vicinity of the initial collision.

As mentioned, fast neutrons lose energy mainly by elastic scattering while slow and thermal neutrons are more likely to be captured. The two most important capture reactions in tissue are $^1H(n,\gamma)^2H$ and $^{14}\mathrm{N(n,p)}^{14}\mathrm{C}$. The nitrogen-capture reaction releases a 2.22 MeV gamma ray, which may deposit a fraction of its energy and leave the body. In the second capture reaction an energy of 0.626 MeV is released. This energy is deposited by the proton and recoil carbon nucleus in the close vicinity of the capture site and thus contributes to the local dose.

The absorbed dose from fast neutrons is primarily due to elastic scattering where energy is transferred to the atomic nuclei. A fast neutron loses on an average half its energy in a collision with hydrogen. A fast neutron will often undergo only one collision before leaving the body and thus can the estimation from a single collision be a good approximation to the dose from fast neutrons. A 5 MeV neutron has a mean free path of 20 cm in tissue and is then not expected to undergo multiple scattering while passing through the body. Because fast neutrons deposits the majority of their energy in tissue through collisions with hydrogen, the estimate of a first-collision dose with tissue hydrogen has been shown to give a good approximation of the lower-bound fast neutron dose. In fact, studies show that hydrogen recoils contribute 85-95% of the first-collision soft-tissue doses for neutrons with energies between 10 keV and 10 MeV [16].

4.3 Shielding Considerations

In all situations where radiation is present, shielding for workers and the general public is important in order to avoid harmful exposure to radiation. The choice of material used for shielding is dependent on the type of radiation present, its energy and intensity. In general, Gamma-rays are most efficiently attenuated by materials with a high atomic number, Z. Lead and tungsten are, as discussed earlier, the most common materials used as photon collimators in medical linear accelerators. For wall and room shielding in general, concrete is often chosen because it is relatively cheap. However, if space is limited, and there is no room for thick concrete walls, denser materials may also be used here.

For stopping charged particles like alpha particles and carbon ions, dense materials are well suited because charged particles then will have a high energy loss, dE/dx. Neutrons are efficiently moderated in hydrogenous material, e.g. water or paraffin. Thermal neutrons are most efficiently stopped by cadmium or boron. Cadmium will produce photons which then needs to be shielded for, while boron will produce alpha-particles which are easier to stop. Neutron shielding should in general be followed by a layer of high-Z material in order to absorb photons from neutron capture reactions. An overview of shielding materials for various radiations is given in table 4.2.

Table 4.2: Recommended shielding materials for various types of radiation [2].

Radiation	Shielding
Gamma-rays	High-Z materials, e.g Pb or W.
Electrons	Low-Z materials, e.g. polystyrene or lucite. Because high-Z materials would cause production of bremsstrahlung they should be avoided. In the case of intense electron sources, shielding by low-Z materials can be followed by an additional layer of a high-Z material to absorb the bremsstrahlung. In this case it is important that the first layer is thick enough to stop the electrons.
Positrons	High-Z materials
Charged particles	High density materials.
Neutrons	Hydrogenous materials such as water of paraffin. Thermal neutrons are most efficiently stopped by cadmium or boron.

Chapter 5

Neutron Detectors

Neutrons are detected through the charged particles they produce in nuclear reactions, both inelastic and elastic. When measuring neutrons, the choice of detector is dependent on a number of factors. In the radiation field from a medical linear accelerator, the neutrons constitute only a small part of the field, and the accelerators delivers radiation in short, intense, pulses. For these reasons, a detector which is not sensitive to photons, and which can be used without dead time problems due to high intensity in the pulses, would be preferable.

In this work, the main focus has been on bubble detectors, but also thermoluminescence detectors and a fission counter have been tested. The advantage of bubble detectors is that they are insensitive to photons and are passive devices. Hence, they can be used in pulsed fields without dead time related errors. TLDs are also passive devices, but they are sensitive to photons and this must then be corrected for. Other detectors which are common to use for neutron measurements at medical linacs are proportional counters, activation foils and thermoluminescence detectors in moderator spheres of various sizes known as Bonner Spheres.

In particle beams like the carbon ion beam at GSI, the use of active detectors, e.g. proportional counters or scintillators, is more common than passive detectors. One of the advantages of measuring with active detectors is that it is not necessary to enter the experimental room and change the detectors for each measurement which is the case for passive detectors. As beam time often is limited, the use of passive detectors may be inconvenient and time consuming.

In this work, bubble detectors were used to measure in the carbon beam experiments. It was a problem with respect to beam time that the detectors had to be exchanged for each measurement and the fact that they require repeated measurement to achieve sufficient statistics.

5.1 BF$_3$ Proportional Counter

The proportional counter using boron trifluoride (BF$_3$) gas is a widely used neutron detector. The reaction

$$ {}^{10}_{5}B + {}^{1}_{0}n \rightarrow {}^{7}_{3}Li + {}^{4}_{2}He \tag{5.1} $$

is the basis for the detection of the slow neutrons with this detector. For increased sensitivity, the ^{10}B is usually enriched above its 19.7% isotopic abundance in nature [16]. Just above 2 MeV energy is produced in the reaction where about two-thirds is carried away by the alpha particle and the rest by the recoiling ^{7}Li nucleus [17]. Because the energy released in the reaction is relatively large, the pulse produced in the detector is larger than pulses produced by photons in the MeV range. This is essential, as electronics applying pulse height discrimination then can be used to eliminate unwanted signals from photons, as well as electronic noise. However, it is a known problem that intense gamma fields causes pile up of multiple pulses from photons. Dead time corrections can in some cases be applied, but it may be difficult to get reliable readings if the photon background is too dominating.

The BF$_3$ counter can also detect fast neutrons if these are moderated. A layer of hydrogenous material, e.g. paraffin wax, is then usually surrounding the detector. The moderated BF$_3$ counter is designed to have an relatively energy-independent fluence response for neutrons of energies up to about 10 MeV.

5.2 Bubble Detectors

Bubble detectors are based on superheated liquids and use a similar principle as the more known bubble chamber. There has been some confusion over the term "bubble detector" and other radiation detectors based on superheated liquids such as the superheated drop detector or SDD [18]. Both types of detectors share the same physics in terms of the formation of bubbles during neutron irradiation. The two types differ only with respect to reading of the bubbles after their formation. The bubble detectors use superheated droplets dispersed throughout a clear elastic polymer. Neutrons passing through the detector produce small visible bubbles. The polymer ensures that the bubbles are trapped at the sites of formation. In the case of the superheated drop detector, the bubbles migrate through the medium (a soft gel) to collect at the top of the detector and the volume of collected gas is used as the basis of dose quantification [19].

For the bubble detectors, the bubbles can be counted visually or by use of automatic readers employing image analysis techniques [20]. From response curves produced by the vendors, it is possible to calculate the dose deposited based on the number of bubbles formed in the detector. A great advantage with this technology is that the detectors can be reused merely by re-compressing the bubbles back into droplets. The bubble detectors are completely insensitive to gamma radiation, and they are passive detectors. These two properties are very important as they make it possible to measure neutrons in areas with intense gamma background and in pulsed radiation fields.

5.2.1 Physical principles of bubble detectors

When a liquid continues to exist in the liquid state above its normal boiling point, it is said to be superheated. Boiling or nucleation can be retarded until the temperature of the liquid reaches its so-called superheated limit. The maximum attainable superheat at atmospheric pressure can be predicted on thermodynamic and kinetic grounds to be approximately 90% of the liquid's critical temperature [21].

In general, boiling in liquids is the result of "heterogeneous nucleation" where impurities in the liquid or liquid/solid interfaces facilitate the phase transition. But if the liquid is surrounded by a second immiscible phase with which it has a zero contact angle then normal boiling is suppressed and the liquid can be heated as high as its superheat limit at which point, it undergoes "homogeneous nucleation".

In 1958 Frederick Seitz postulated that ionizing radiation produces highly localized hot regions or "temperature spikes" within the liquid which literally explodes into bubbles through the evaporation of the superheated liquid [22]. This is often referred to as "thermal spike" theory, and is still widely accepted. The physical processes that produce the bubbles are viewed to be similar to those responsible for producing radiation damage in solids. In order to determine quantitatively the relationship between energy deposition and bubble formation, Seitz postulated that the formation of a visible bubble involved two critical steps: the formation of a vapor bubble of critical size, r_c, and the growth of this into a macroscopic bubble.

The existence of a vapor bubble of radius r_c represents a maximum in the free energy potential of the system and is therefor unstable to slight perturbation [23]. Vapor cavities of smaller radii will collapse under the effects of surface tension. On the other hand if r_c is exceeded then the cavity will spontaneously expand to form a macroscopic-sized bubble (see figure 5.1). The minimum amount of energy required to form a vapor cavity of radius r_c is shown to be [22]

$$E_{min} = 4\pi\sigma r_c^2 + \frac{4}{3}\pi r_c^3 \rho_v \frac{H}{M} \tag{5.2}$$

Here σ is the surface tension of the liquid and ρ_v is the density of the vapor. H and M represent the molar heat of vaporization and molecular weight respectively. The first term in the equation represents the energy required to form a bubble of radius r_c against the forces of surface tension while the second term gives the energy required to vaporize the liquid in order to produce the bubble [20].

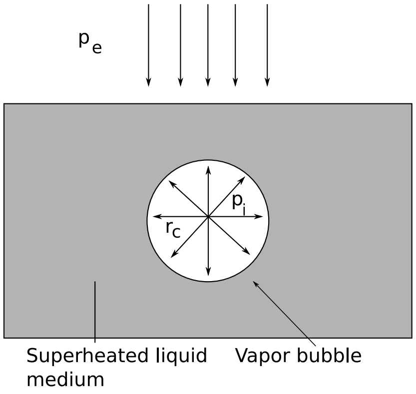

Figure 5.1: Schematic diagram showing a vapor bubble of radius r_c in a liquid medium. External pressure p_e plus pressure due to bubble surface tension tend to crush the bubble while the pressure p_i of the vapor associated with the liquid acts to expand the bubble [20].

Seitz postulated that the energy required to nucleate the superheated liquid was the result of energetic recoil ions stopping in the liquid. A portion of the energy loss is degraded to thermal energy allowing localized vapor formation. Today it is believed that the recoiling ions are envisaged to produce a plasma-like region (equivalent to the thermal-spike) within the droplet medium. As this plasma cools, microscopic gas bubbles are formed. Nucleation will occur if the local value of r_c is exceeded or, in others words, the local superheat limit is surpassed. Seitz's theory was developed for the bubble chamber, but is also applicable for bubble detectors as each superheated droplet is, in effect, an isolated bubble chamber. Further investigations showed that the effective length, (L), over which a particle must deposit sufficient energy to cause nucleation might be linearly related to the value of r_c [24]. If L is assumed to be much shorter than the total track length of the particle then the energy deposited is given by

$$E = L\left(\frac{dE}{dx}\right)_{avr} = kr_c\left(\frac{dE}{dx}\right)_{avr} \tag{5.3}$$

where $\left(\frac{dE}{dx}\right)_{avr}$ is the average stopping power over the interaction length L and k is a proportional constant. A number of estimates on the constant k has been performed, and the results are varying from values of 2 to 13. Equating equations 5.2 and 5.3 shows that at a given temperature there is a threshold value of $\left(\frac{dE}{dx}\right)_{avr}$ where nucleation is not possible [20]. This is important because it implies that detectors can be made with energy thresholds excluding unwanted signals. The idea of making a crude neutron spectrometer comes from this concept. A non-dimensional quantity, defined as 'reduced superheat', has recently been introduced and shown to permit a unified parametrization of the properties of superheated droplet detectors and bubble detectors. In particular, utilizing the reduced superheat concept, it is possible to predict the neutron detection thresholds of the detectors and their sensitivity to thermal neutrons and to photons.

The response, (R), of superheated droplet detectors for monoenergetic neutrons can be described in terms of the incident energy (E_n) and temperature (T) as follows

$$R(E_n, T) = \phi(E_n) V \sum^{n} N_i \sum^{m} \sigma_{ij} F_{ij}(E_n, T) \tag{5.4}$$

where $\phi(E_n)$ is the neutron flux and V is the total volume of superheated droplets. The number of isotopes in the superheated material is given by n and N_i represents the atomic density of each isotope. The number of considered reaction cross-sections is given by m and σ_{ij} is the relevant cross-section for the i, j interaction. The relevant nuclear reactions which are usually taken into account include elastic and inelastic scattering as well as charged particle production. F_{ij} is a factor which describes the probability of the i, j interaction leading to nucleation [20]. In the case of continuous neutron sources, detector response is calculated by integrating equation 5.4 with respect to neutron energy or by summing over the energy intervals [20].

To summarize the physical processes leading to the formation of visible bubbles from exposure of the bubble detector to neutrons: A fraction of the neutrons which traverse the bubble detector will interact with the detector. The probability of interaction is determined by the specific composition of the medium in the detector. Some of these interactions will occur "far" from the sites of the superheated liquid droplets, and others will occur "close" to these sites and a small fraction will interact with the superheated liquid droplets themselves. These interactions give rise to a variety of secondary charged particles, including recoil ions [20]. The charged particles will slow down in accordance with the stopping power of the ions in the medium at the interaction site. The energy deposited here is what produces the "thermal spike".

Some of the secondary charged particles will pass through a droplet and deposit a fraction, or all of its energy in the droplet. The passage of the particle within the superheated droplet will give rise to a trail of microscopic bubbles. Some of these bubbles may coalesce to form bigger bubbles. The smaller bubbles will be recompressed due to the surface tension. However, if bubbles exceed the critical bubble size, r_c, then they will grow into macroscopic bubbles. The minimum amount of energy required for creating a critical sized bubble is given by equation 5.2. This energy must be deposited over a distance less than approximately 100 nm within the superheated droplet. Once a bubble larger than the critical size is formed, all the liquid in the superheated droplet will be vaporized into the bubble causing it to grow quickly. The vaporization process emits a characteristic acoustic signal which actually can be used for detection of bubble formation.

Due to the elastic polymer in the detector, the bubbles will be trapped at the sites of formation. The number of bubbles can finally be used to provide a measure of the neutron field. It is important to notice that the size of the visible bubble is determined by the size of the droplet at the site and not by the amount of energy deposited. Thus, the size of the bubble is not related to the property of the incident neutron.

5.2.2 Response to protons

Protons of energies higher than 1.5 MeV do not have sufficient stopping power, dE/dx, to form bubbles in the detectors and thus must interact by nuclear reactions to produce bubbles. Experiments show that the BD-PND bubble detectors from Bubble Technology Industries have a response to protons with energy lower than 70 MeV of about one order of magnitude less than the sensitivity to neutrons. The sensitivity to protons of higher energies than 70 MeV is expected to be similar [25]. Estimates of the stopping power needed for bubble formation is shown in figure 5.2 together with stopping power of protons, helium and carbon as a function of energy. The horizontal lines show the lowest and highest thresholds estimated for the stopping power needed for bubble formation. Although these tests were made with a different bubble detector than those used in this work, the response to protons is expected to be similar.

5.2.3 Bubble detector spectrometer - BDS

The BDS consists of 36 neutron bubble detectors. The detectors have 6 different energy thresholds, covering the neutron energy range 10 keV to 20 MeV. From the individual thresholds in units of keV the detectors are named bds-10, bds-100, bds-600, bds-1000, bds-2500 and bds-10000. Figure 5.2 shows the response to neutrons of the BDS detectors. The detectors are calibrated by the manufacturer (Bubble

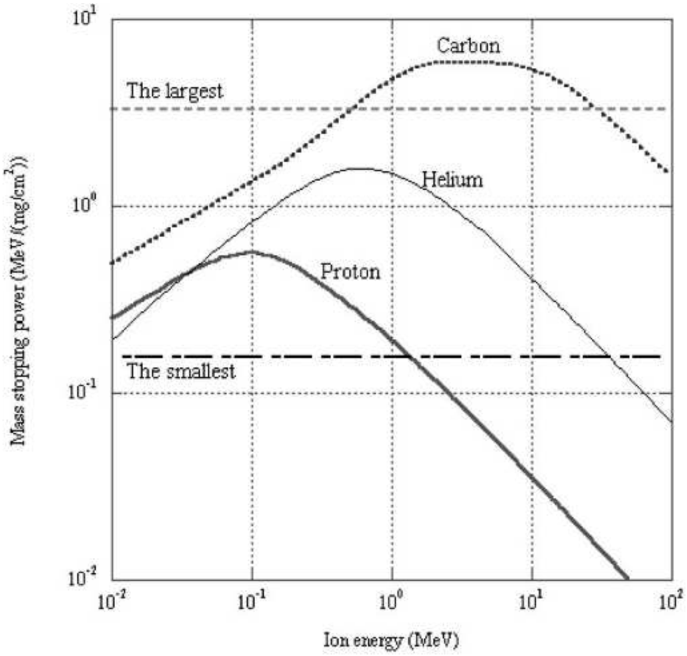

Figure 5.2: Mass stopping powers in a droplet of bubble liquid. The thick solid, the thin solid and the dotted lines show the mass stopping powers of protons, helium and carbon ions, respectively. The dashed and the alternate long and short dash horizontal lines show the largest and the smallest thresholds, respectively, of mass stopping powers to form bubbles in bubble detectors [25].

Technology Industries) by exposure to an AmBe neutron source, and a conversion factor of

$$3.70 \times 10^{-7}\ mSv/n.cm^{-2} \tag{5.5}$$

is applied to find the detectors sensitivity in units of equivalent dose, bubbles per μSv. As the detectors are sensitive to temperature changes, it is recommended that measurements are done at 20 ± 0.5 ℃. By comparing the response from the various detector types, a crude neutron spectrum can be obtained through a simple unfolding procedure. Unfolding of the data from the bubble detector spectrometer is based on a number of assumptions [26]:

1. The derived unfolded spectrum can be adequately approximated by a 6-region histogram.
2. The neutrons detected are assumed not to have higher energy than 20 MeV.

3. Fluence per unit energy is constant over the histogram interval.

If there are few or none neutrons in some energy intervals in the source spectrum, it might happen that one or more of the intervals comes out with a negative fluence. This is due to statistical uncertainties and usually occurs in the lower energy regions because the unfolding can suffer from error accumulation. In such cases, it is common to set the fluence for the current interval to zero. This is referred to as the "non-negativity" condition imposed on the spectral unfolding.

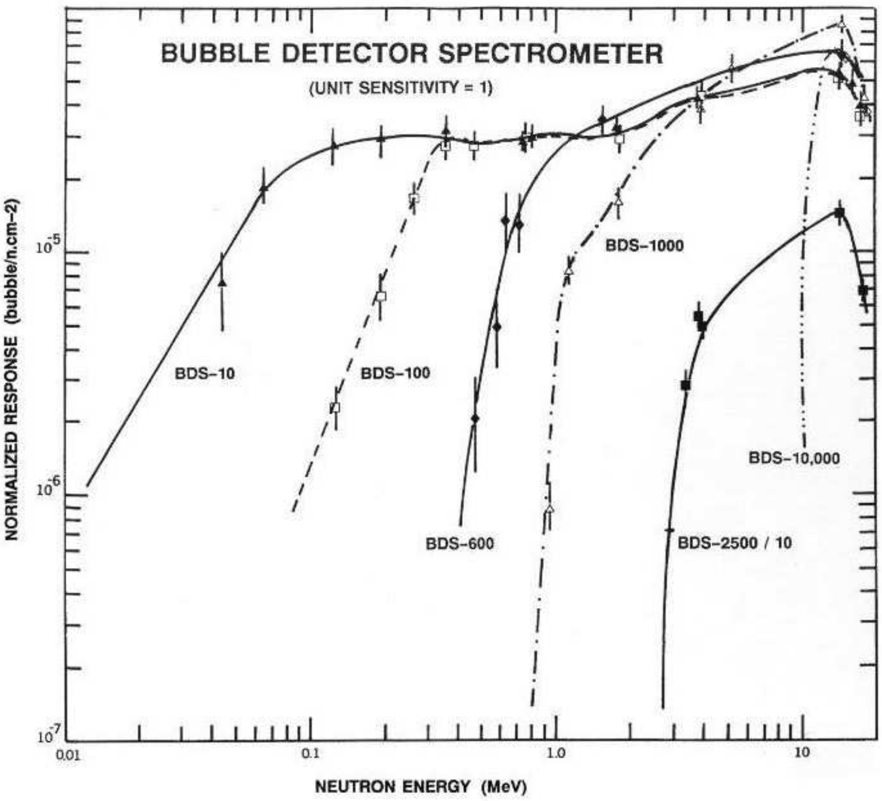

Figure 5.3: BDS normalized response in units of bubbles per neutron/cm^2 versus neutron energy [26]. The response for the BDS-2500 is divided by 10 in the figure.

5.2.4 BDS detectors' response to high energy neutrons

In the carbon beam measurements, neutrons with energies up to about twice the energy of the nucleons in the primary carbon ions are present. While the detectors are calibrated for neutrons up to 20 MeV, in this

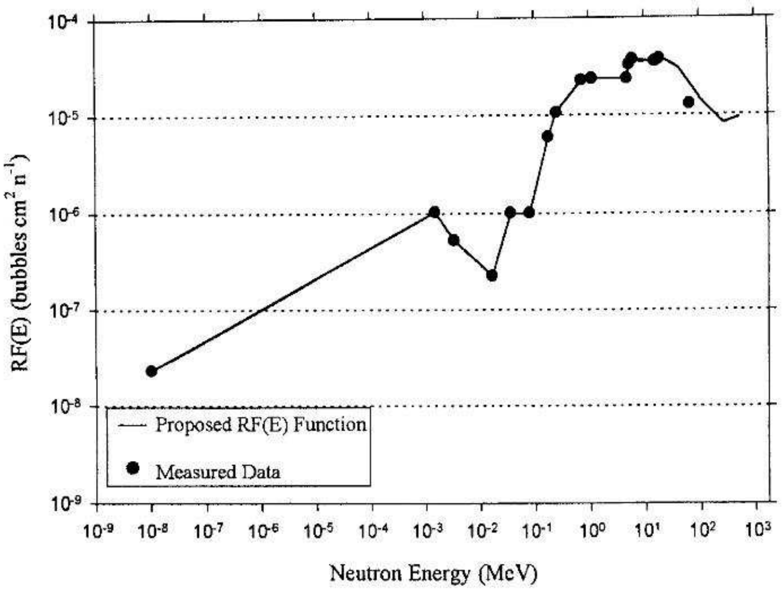

Figure 5.4: Response of the BD-PND bubble detector to neutrons over a wide energy range at 20 ℃ [27]. This detector is made by the vendor of the bubble detectors used in this work, and their response to high energy neutrons is expected to be similar.

setting there will be neutrons with energies up to 400 MeV. There has been some research on the response to high energy neutrons of the BD-PND which is another bubble detector from Bubble Technology Industries. Response for the BD-PND as a function of neutron energy is shown in figure 5.4. The investigation of response to high energy neutrons was performed in relation to measurements of neutron doses in commercial flights. In that experiment [27], it was concluded that the bubble detectors could be used with a correction factor of 1.5 to the original sensitivities to take into account that neutrons above 20 MeV were present. For the BDS detectors, a similar response to high energy neutrons is expected, but this must be investigated through experiments in a calibrated high energy neutron beam before equivalent neutron doses can be obtained in high energy neutron environments.

5.2.5 Bubble detector thermal - BDT

The BDT bubble detector uses a ^{6}Li compound dispersed throughout the polymer medium and a special formulation to detect preferentially α particles from the $^6Li(n, \alpha)T$ reaction. This gives the BDT an exclusion ratio of thermal to fast neutron response exceeding 10 to 1.

The BDTs have an integrated temperature compensating mechanism making it possible to use the detectors in the temperature range 20 to 37 ℃. As the BDS, the BDTs are calibrated by the manufacturer, and the average sensitivity in temperatures between 20 and 37 ℃ is given in units of bubbles per μSv.

5.2.6 Recompression of bubbles

After readout, the bubbles in the detectors need to be compressed into droplets again before the detectors can be reused. The BDT detectors have an integrated assembly making it possible to recompress the bubbles merely by screwing the top part of the detector back on after use. The BDS detectors do not have an integrated recompression assembly, and thus a pressure chamber is needed. BTI offers a recompression chamber which is simple in use and can recompress up to 18 detectors simultaneously. This recompression cycle takes about 15 minutes.

5.2.7 Counting of bubbles

The vendor of the bubble detectors offers an automatic reader specially designed for counting bubbles using computer image processing techniques. In this work however, the bubbles were counted manually. A digital SLR camera was used to take pictures of the irradiated detectors. Based on the digital images, the bubbles were counted manually in an image analysis software on the computer. Figure 5.5 shows the counting process.

5.3 Thermoluminescence Detectors - TLD

Thermoluminescence detectors (TLDs) are widely used in dosimetry. TLDs are found in a variety of shapes, and can be made from different materials depending on which type of radiation they are intended to detect.

5.3.1 Principles of thermoluminescence

When irradiated some mineral substances store a small fraction of the energy imparted in their crystal lattice. The energy can be released as light if the material is heated after irradiation. This phenomenon of the release of photons by thermal means is known as thermoluminescence (TL).

To understand the mechanisms involved in the process of thermoluminescence, some basic understanding of solid state physics is needed.

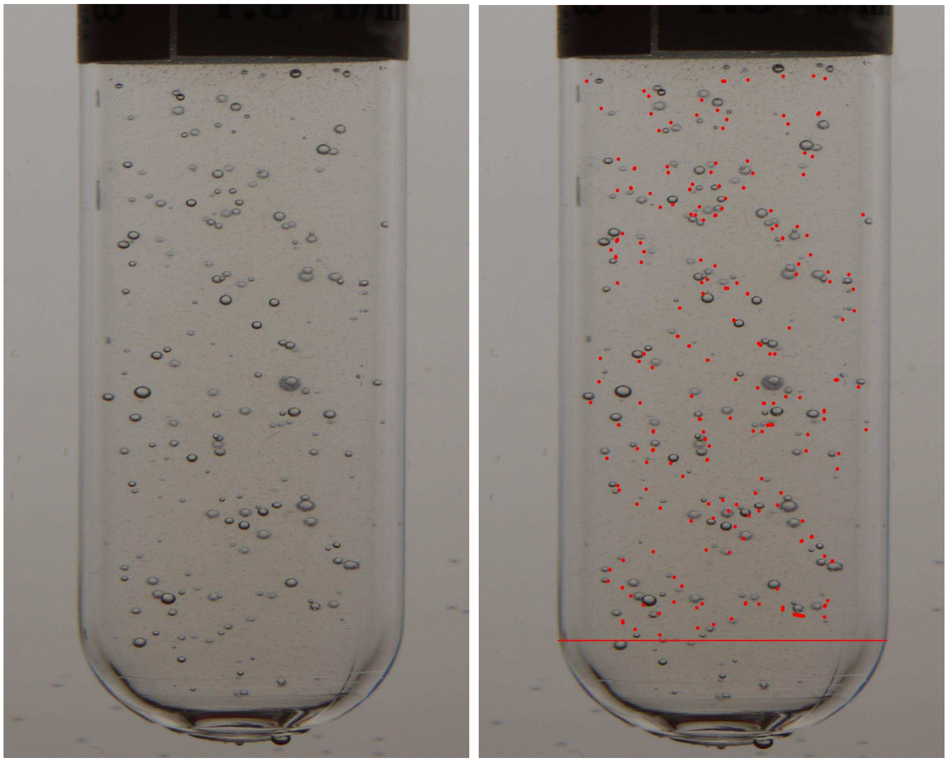

Figure 5.5: Bubble counting procedure. The original picture is shown to the left. On the right hand side, the bubbles have been marked and counted. In this case 181 bubbles. The red horizontal line gives the limit of the effective detector area.

In an individual atom electrons occupy discrete energy levels. In a crystal lattice, on the other hand, electron energy levels are perturbed by mutual interactions between atoms and give rise to energy levels referred to as "allowed" and "forbidden" energy bands. In addition, the presence of impurities in the crystal creates energy traps in the forbidden region, providing metastable states for the electrons [3]. When the material is irradiated, some of the electrons in the valence band (ground state) receive sufficient energy to be raised to the conduction band. The vacancy created in the valence band is called a positive hole. The electron and the hole move independently through their respective bands until they recombine (electron returning to the ground state), or until they fall into a trap.

If there is instantaneous emission of light owing to these transitions, the phenomenon is called fluorescence. If an electron in the trap requires energy to get out of the trap and fall to the valence band, the emission of light in this case is called phosphorescence (delayed fluorescence). If phosphorescence at room temperature is very slow, but can be speeded up significantly through heating, the phenomenon is called thermoluminescence. A plot of the emitted light output against temperature is called a glow curve. The photons emitted by the TLDs are collected and transformed into a current by a photomultiplier.

5.3.2 TLD neutron dosimetry

Measuring neutron doses with thermoluminescence detectors is not trivial because there are no neutron sensitive TL elements available which are not also sensitive to photons. The most common way to obtain neutron doses using TLDs is to use two types of TL elements, one which is sensitive to both neutrons and photons and one which is only sensitive to photons. Using these, the photon dose can be subtracted, and the dose from neutrons can be obtained. The TLD-600 and TLD-700 are the standard TL elements used for neutron dosimetry. The TLD-600 is based on ^6LiF (lithium fluoride) and has a large cross section for thermal neutrons while TLD-700 which contains ^7LiF, is relatively insensitive to thermal neutrons in comparison. Both types are sensitive to gamma radiation. To extract information about the neutron field there is a number of steps which needs to be performed. After an unfolding process the following equation is obtained

$$R_{600}^{n} = R_{600}^{n+\gamma} - \frac{R_{700}^{n+\gamma}}{k} \tag{5.6}$$

where R_{600}^{n} is the TLD-600's response to neutrons, $R_{600}^{n+\gamma}$ is the total response of the TLD-600 element, $R_{700}^{n+\gamma}$ is the total response from the TLD-700 and k is the ratio of the gamma sensitivities of the two TLD types. The light emitted from the TLDs is transformed to a current by a photomultiplier, and the total charge output, usually given in nanocoulombs (nC), is given by the TLD reader. To be able to convert the charge to dose, calibration is needed. For neutron dosimetry, the TL elements must be exposed to a thermalized neutron beam or a neutron source with a known fluence.

5.4 Thin Film Breakdown Counter - TFBC

The thin film breakdown counter is based on fission induced by hadrons incident on an uranium target (^{238}U). The threshold energy for neutron induced fission of ^{238}U is found in experiments to be 1.0±0.1 MeV [28]. Thus, a neutron of energy above 1 MeV incident on the uranium target can lead to a fission process. The fission fragments will lose energy by ionization, i.e., inelastic collisions with atomic electrons, in the counter and eventually stop. The bias voltage in the counter ensures that the free electrons drift along the electric field and produce a current. When a sufficient amount of atoms has be ionized, a signal is produced from the electron current and the neutron is detected. This concept can be used to measure the neutron flux in a radiation field dominated by photons. The uranium target of the detector can be changed in order to vary the sensitivity of the detector. Figure 5.4 illustrates the principle of the breakdown counter. This detector was briefly tested in this work, and it was found that the sensitivity of the uranium target was too low for measurements of radiation from medical linear accelerators. The use of this detector is therefore not discussed further in this thesis. However, a fission detector designed for this purpose might be a good alternative, or supplement, to the other neutron detectors discussed in this chapter.

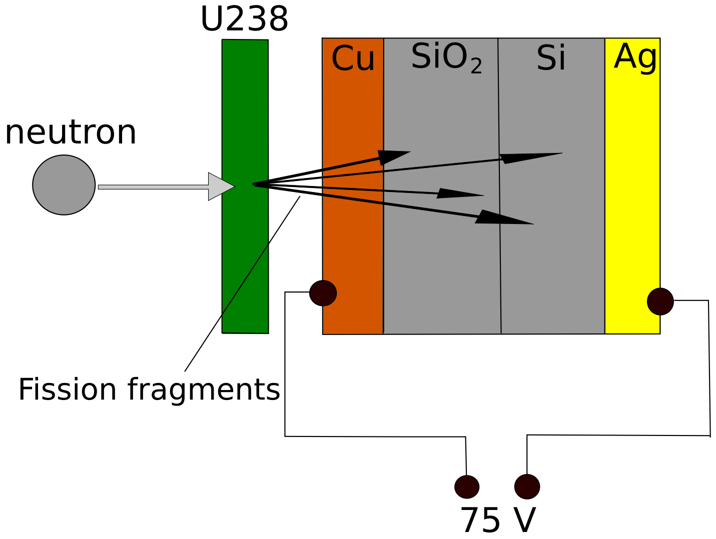

Figure 5.6: Sketch of the Thin Film Breakdown Counter.

Chapter 6

Experimental Setup

In this chapter, the various experimental measurement setups are described.

6.1 Neutron Source Setup

At GSI-Darmstadt in Germany, an Americium-241/Beryllium neutron source with a nominal activity of 1 Curie was used to perform tests of the bubble detectors and the TLDs. The bubble detectors were placed in a circle around the source at a distance of 9 cm to the source and exposed during a few hours for each measurement to achieve sufficient statistics. Figure 6.1 illustrates the setup. In the same way, the TLDs were placed around the neutron source.

6.2 Photon Beam Setup

A Varian 23iX medical linear accelerator, at Haukeland University Hospital in Bergen, was used for the photon beam measurements. For measurements with the bubble detectors, a water equivalent plastic phantom of size 30 × 30 × 20 cm^3 was designed. Measurements were made both in the phantom and in the isocenter plane without the phantom present. Figure 6.2 illustrates the top view of the phantom. The phantom has 36 holes designed for insertion of bubble detectors, and this render possible measurements at various positions. The positions 8, 9, 14 and 15 were used for measurements in the photon beam.

The energy of the photon beam was set to 15 MeV, except during the calibration of the TLD gamma response, where a 4 MeV photon beam was used. All the 15 MeV measurements except the measurements without, were performed by applying a 5 × 5 cm^2 field. The isocenter was located at 8.57 cm depth in the phantom. This depth

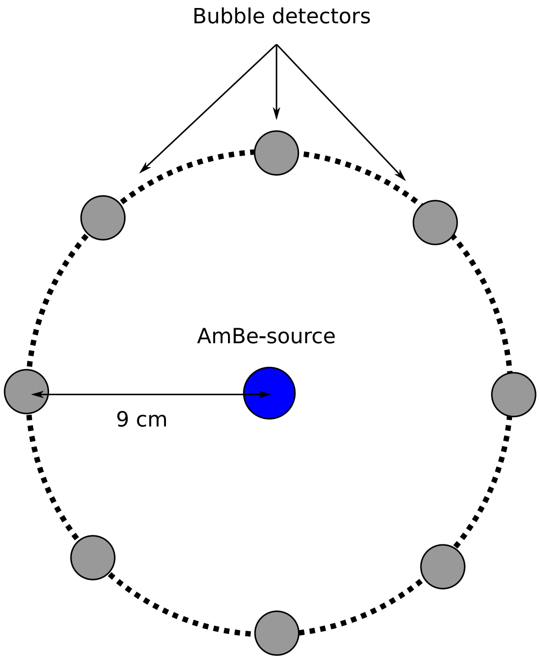

Figure 6.1: Top view of the setup for the neutron source measurements. The detectors were placed in a circle 9 cm from the AmBe-source.

is equivalent to the Bragg peak depth for the 200 MeV/u ^{12}C beam used at GSI. The setup for the measurements in the isocenter plane without the phantom is shown in figure 6.3. A 5×5 cm^2 photon field was also used for this measurement. The detectors were placed 4 cm off axis, as shown in the illustrations. Figure 6.4 shows the setup for the in-phantom measurements in the photon treatment room. The linac was equipped with multi leaf collimators (MLCs), which are frequently used in the daily patient treatments. The MLCs were fully retracted during all measurements in this work, with the exception of tests in position 8 and 9 in the phantom with the MLCs closed completely.

The linacs at Haukeland University Hospital are calibrated to deliver a dose of 1 Gray per 130 monitor units. This is not the dose applied to the whole photon field, but using a 10×10 cm^2 photon field, 1 Gray is delivered to the isocenter in the case where this is placed at 10 cm depth in water. The isocenter is the point in the center of the photon field located at 1 meter distance from the target which produces the beam.

When using other field sizes, and calculating doses at other depths than 10 cm, it is necessary to use conversion tables. As can be seen in figure 3.5, the dose as a function of depth increases to a maximum and then decreases. Hence, a target in any other position in depth will

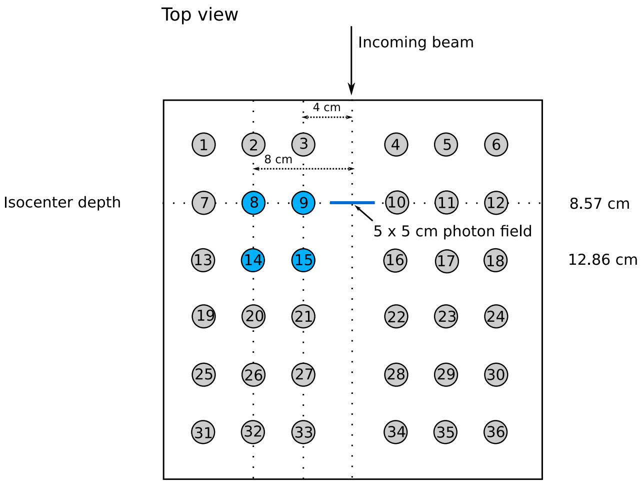

Figure 6.2: Top view of the phantom. The positions 8, 9, 10 and 11 were used for experiments in the photon beam.

receive a different dose from that in 10 cm depth. The Tissue Phantom Ratio (TPR) tables are used to correct for the change in depth from the calibration setup to the clinical or measurement setup. In addition to this, a change in field size will have impact on the absorbed dose. For field sizes larger than 10 × 10 cm^2, dose in the isocenter builds up with contributions also far from the isocenter itself. This results in a higher photon dose for larger photon fields, even though the number of monitor units is kept constant. To apply 1 Gray at 8.57 cm depth in tissue, using a 5 × 5 cm^2 field, the following calculations are needed

$$130MU \times \frac{FieldFactor}{TPR} \tag{6.1}$$

$$130MU \times \frac{1.07}{1.044} = 133MU \tag{6.2}$$

For the BDT in-phantom measurement, a typical dose of 1 Gray was sufficient to achieve adequate statistics for one detector. The BDS detectors have a lower sensitivity, and photon doses on the order of 8 Gray or more was applied to produce roughly 200 bubbles, which is the recommended amount. For the measurements in the isocenter plane without the phantom, the needed dose for producing 200 bubbles was between 1 and 4 Gray for the various detector subgroups. It should be noted that throughout this work the estimation of dose in Gray is based on the calculations in equation 6.2, i.e., 133 MU is equivalent to 1 Gray. In the photon beam setup, symmetry could not be assumed because neutrons here are mainly produced in the treatment head, and

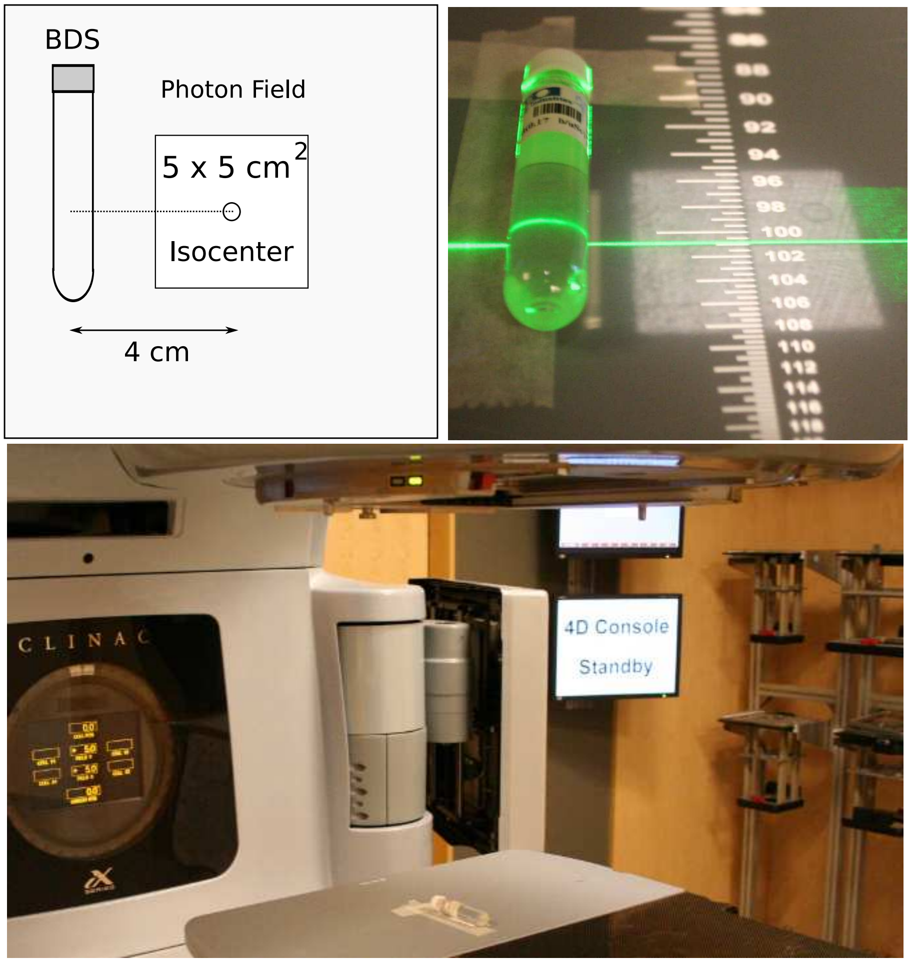

Figure 6.3: Top and side view of measurement setup in the isocenter plane without the phantom. The BDS detectors were placed in the isocenter plane 4 cm off axis from the center and aligned so that the effective detector area was aligned to the central beam axis in the longitudinal direction. The scale on the upper right picture shows that the center of the detector is placed at 1 meter vertical distance from the target in the linac.

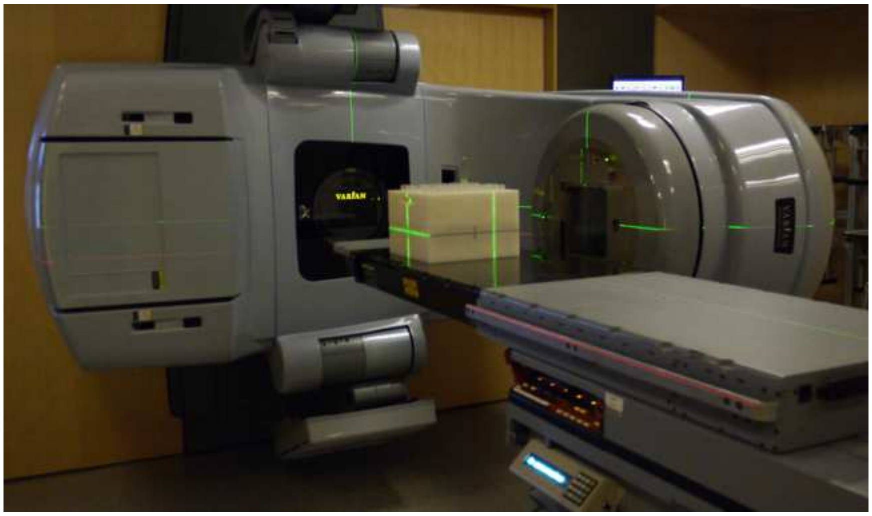

Figure 6.4: Experimental setup for the in-phantom measurements at Haukeland University Hospital. The isocenter is placed at 8.57 cm depth in the phantom.

the distribution of these neutrons in the room was not known. As shown in figure 6.2, the positions 8, 9, 14 and 15 were used for measurements in the photon beam.

6.3 Carbon Beam Setup

At GSI, a 200 MeV/u ^{12}C pencil beam was used for measurements with the bubble detectors BDS-10, BDS-2500 and BDS-10000, with the same phantom as used in the photon beam setup. Figure 6.7 shows a sketch of the phantom and marks the measurement positions used in the carbon beam experiment. All measurements were performed in the experimental room known as cave A in the GSI target hall. The energy of the primary carbon ions of 200 MeV/u represents a mean value of the set of energies typically required for treatments of tumors in the head and neck regions performed at GSI since 1997 [9]. It was assumed that the radiation field was symmetric with respect to the beam axis. This made it possible to use two equivalent measuring points at the same time, e.g position 9 and 10. The range of a 200 MeV/u ^{12}C beam in water was calculated to be 8.57 cm using the simulation tool LISE++. This indicates that the positions 8 to 11 are located at the Bragg peak depth, while positions 14 to 17 are located about 4.3 cm behind the Bragg peak.

The setup for the carbon beam measurements is shown in figure

Figure 6.5: Experimental setup in cave A at GSI. The beam pipe to the left is followed by an ionization chamber and the plastic phantom.

6.5 and 6.6. Before entering the phantom, the carbon beam passes through an ionization chamber, and from this the number of carbon ions irradiated can be obtained.

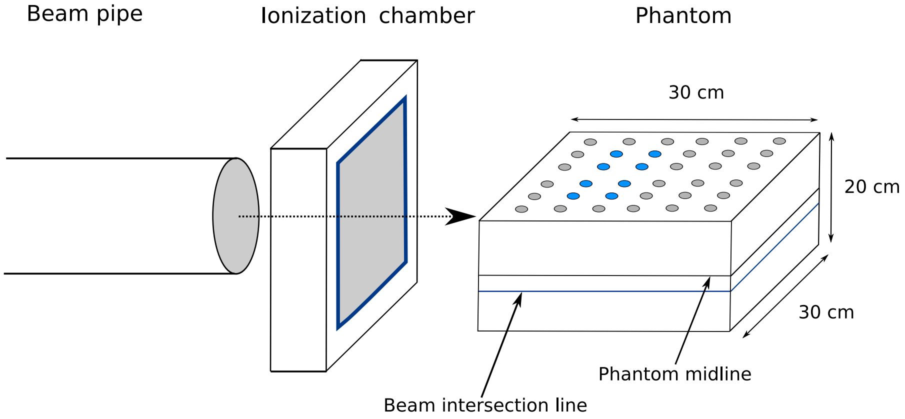

Figure 6.6: Setup in the experimental carbon beam room, cave A, at GSI.

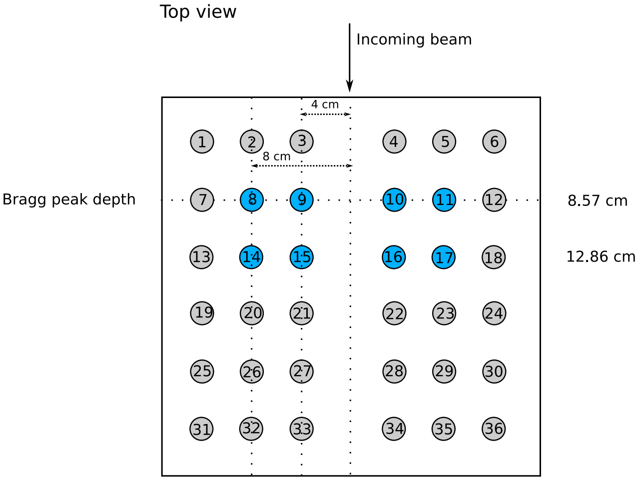

Figure 6.7: Top view of the phantom. The positions 8 to 11 and 14 to 17 were used for the experiments at GSI. The Bragg peak depth is based on an energy 200 MeV per nucleon for the ^{12}C beam.

Chapter 7

Experimental Results and Discussion

Presented in this chapter are the results from measurements performed in the 15 MeV photon beam setup in Bergen and from an AmBe neutron source and a 200 MeV/u carbon beam at GSI-Darmstadt in Germany.

7.1 Bubble Detector Characteristics

A number of tests were performed in order to understand the behavior of the bubble detectors, and to get an indication of the uncertainties that can be expected in experiments. It is always desired to achieve good statistics to get reliable results, also for these tests, however, as the bubble detectors have a limited lifetime and reuse capability it is not always favorable to concentrate on a few details and get very high statistics for those. In this work, the distribution in response for repeated measurements with single detectors were measured, also the spread in sensitivity within the same detector genre (e.g. BDS-10) was investigated. In addition to this, the temperature dependence and the change in sensitivity over time for the BDS detectors were studied. From these different investigations, a good understanding of the bubble detectors' performance can be achieved and information on the use of the detectors and the uncertainties in the measurements can be attained. Because very few neutrons above 10 MeV are present in the radiation field from the medical linacs at Haukeland it was not possible to include the BDS-10000 detectors in the experiments.

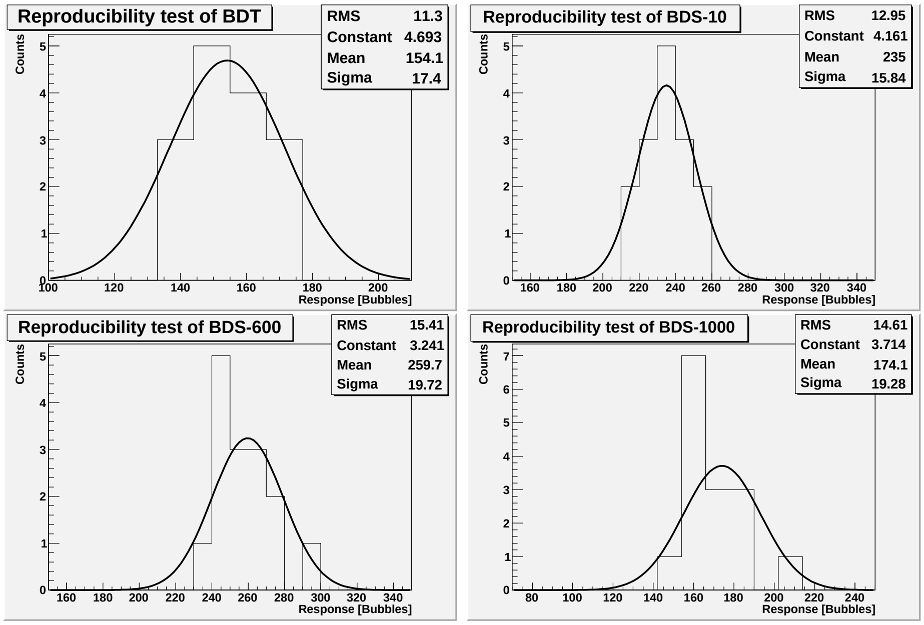

Figure 7.1: Reproducibility measurements for the BDT, BDS-10, BDS-600 and BDS-1000. A Gaussian fit has been applied and the standard deviation calculated from the fit. The rms is calculated from the raw data. While the BDT and BDS-10 response seems Gaussian distributed, a tail can be seen in the distribution both from the BDS-600 and BDS-1000.

7.1.1 Reproducibility tests

Repeated measurement with single bubble detectors were performed in order to study the reproducibility of the measurements. Detectors of the types BDT, BDS-10, BDS-600 and BDS-1000 where tested. Each individual detector was irradiated 15 times in position 9 of the phantom (see figure 6.7) with a 15 MeV photon beam. The results from the irradiations are shown in figure 7.1. To all histograms Gaussian fits have been applied, and the rms calculated from the data and the standard deviation obtain from the fit are also shown in the figure. Both the standard deviation and the rms is given in units of bubbles. The rms in percent are 7.3%, 5.5%, 5.9% and 8.4% for the BDT, BDS-10, BDS-600 and BDS-1000, respectively. For the higher threshold detectors, BDS-600 and BDS-1000, the response distributions are somewhat asymmetric, and a tail in the distribution can be seen. This may indicate that they are more sensitive to changes in temperature or other factors than the lower threshold detectors.

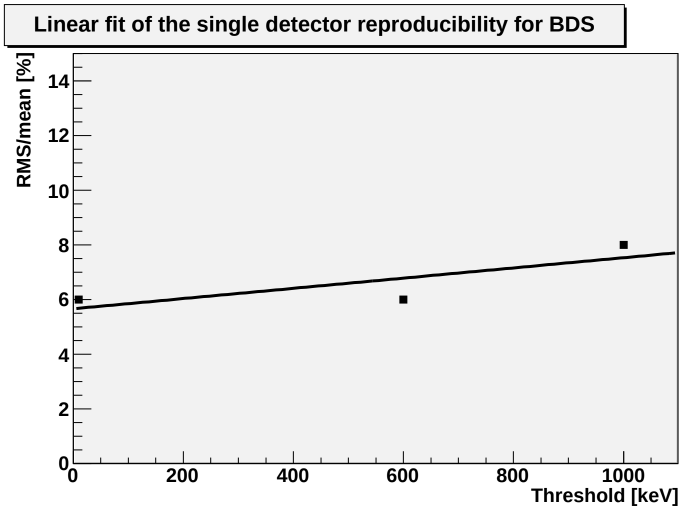

Figure 7.2: Linear fit of the uncertainties in single detector measurements. The fit is based on measurements with single BDS-10, BDS-600 and BDS-1000 detectors and uncertainties are given in percent of the mean value.

7.1.2 Spread in sensitivity

Although the detectors within a subgroup of the BDS are made in the same way, there will always be some variation in the sensitivity between detectors in a batch. The detectors are delivered from the manufacturer with a calibration certificate giving the average sensitivity of each single detector, obtained by exposure to an AmBe neutron source with known neutron fluence. However, no information about the uncertainties in the response is given, and it was clear that, at least after some use, the spread in sensitivity was significant and should be investigated.

To achieve an indication of the spread in sensitivity within the same detector type, all detectors were irradiated three times under equal conditions. Approximately 600 bubbles were obtained for each detector corresponding to a statistical uncertainty of about 4%. As for the distribution tests, a Gaussian fit has been applied in each plot, and the standard deviation estimated from this. The results from the measurements are displayed in figure 7.3. In percent, the rms values varies from 6% for the BDS-1000 detectors to 19% for the BDS-10.

In general, the spread is relatively small for the BDS-100, BDS-1000 and BDS-2500 detectors, while the BDS-10 and BDS-600 detector responses differ more from one detector to the next. It can be seen that the relative difference in response from the least sensitive to the most sensitive detector within a genre can be close to 100%. This can give misleading results if not all detectors have been made use of in

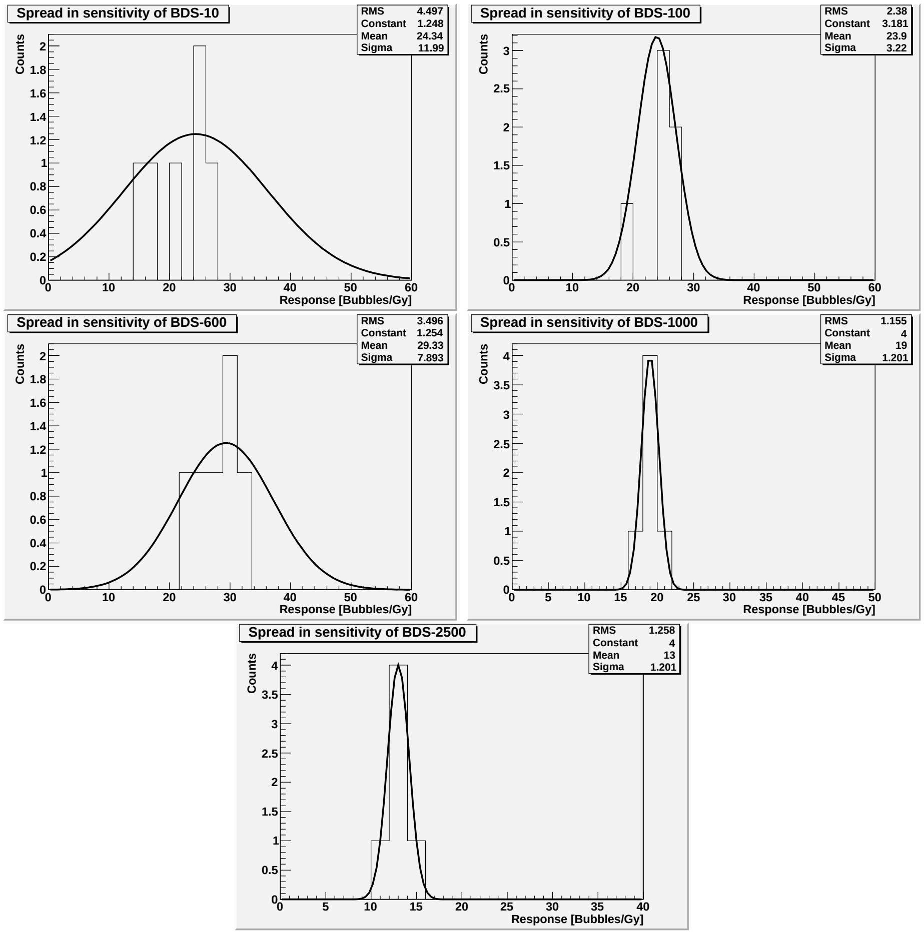
Spread in sensitivity of BDS-10

Spread in sensitivity of BDS-100

Spread in sensitivity of BDS-600

Spread in sensitivity of BDS-1000

Spread in sensitivity of BDS-2500

Figure 7.3: Spread in sensitivity between the six detectors of each threshold in the BDS. The standard deviation is calculated from the Gaussian fit, while the rms is obtained from the raw data.

each measurement series and an average value used as the valid result. All the detectors have not been used for every measurement in this work, and this implies that the average response found from repeated measurement might not be representative for the whole batch. In the unfolding procedure an average sensitivity given by the manufacturer is applied (table B.1), and this could then lead to misrepresentative neutron energy spectra and dose estimates. The importance of using all detectors in a batch to obtain the average response should be emphasized when planning further measurements with the BDS.

Table 7.1: Estimated uncertainties of single BDS detectors (rms_{single}) from the linear fit in figure 7.2, and spread (rms_{spread}) in sensitivity from the measurements in this section. For the in-phantom spectrum measurements nine measurements were performed in each position reducing the uncertainty by a factor 3.

Detector	rms_{single}/mean	rms_{spread}/mean
BDS 10	6%	19%
BDS 100	6%	10%
BDS 600	7%	12%
BDS 1000	8%	6%
BDS 2500	10%	10%

7.1.3 Temperature dependence of the BDS

From the manufacturer of the BDS it is recommended that measurements should be performed at a temperature of 20 ± 0.5 ℃ to ensure that the sensitivity of the detectors matches the values given in the calibration certificate. In some situations, it may be difficult to keep the temperature within this narrow range. In the measurements performed in the carbon beam and with the neutron source at GSI the temperature was not controlled with sufficient precision. For these reasons, it was important to investigate the impact of temperature changes on the detectors' sensitivities.

Figure 7.4 shows the results from measurements at 15 ℃, 20 ℃ and 25 ℃, a review table can also be seen in appendix C. It can be seen that the detectors with high energy thresholds are more sensitive to temperature changes than the BDS-10 and BDS-100 which already at 20 ℃ have low energy thresholds of 10 keV and 100 keV, respectively. According to experiments performed by Bubble Technology Industries the increases in sensitivities observed for the BDS are mainly due to a lowering of the detectors' neutron energy thresholds [29]. This is in agreement with the data acquired in this thesis. The results show the importance of controlling the temperature and keeping it as close to 20 ℃ as possible during measurements.

In between the measurements conducted in the photon setup, the detectors were placed in a temperature controlled water tank. During irradiation the detectors were inside the phantom, placed in the treatment room with a temperature of approximately 22.5 ℃. Some of the irradiations required longer time than others, and this indicates that errors due to temperature changes could occur in this setup. Temperature fluctuation of 2 ℃ might take place from one measurement to another. Assuming that the sensitivity changes linearly with tempera-

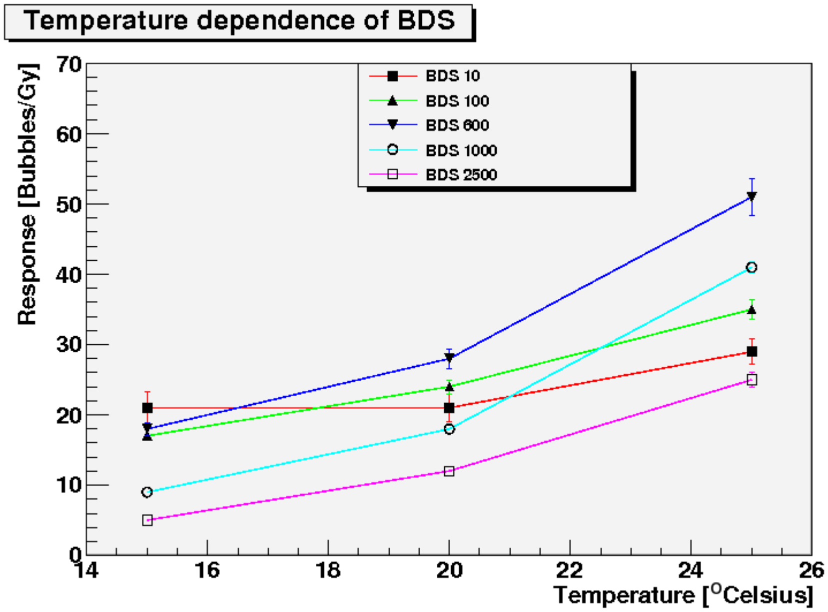

Figure 7.4: Temperature dependence of the BDS. The data indicates that the high threshold detectors are more sensitive to temperature changes. This is in agreement with other experimental work indicating that a rise in temperature will lower the detector thresholds [29].

ture, the results in figure 7.4 indicate that an increase of 2 ℃ from 20 to 22 ℃ may result in a rise in the response of 14%, 18%, 32%, 49% and 39% in individual measurements with the BDS-10 to the BDS-2500, respectively. From this it is likely that the unfolding process, based on the average sensitivities of the detectors at 20℃, will be affected due to temperature fluctuation, resulting in error accumulations in the unfolded spectra. It is evident that a temperature controlled water phantom would be the optimal setup with regard to the reliability of the measurements, and this should be considered as an alternative for future projects with bubble detectors.

7.1.4 Disintegration of bubble detectors

After activation, the bubble detectors have a limited lifetime. The bubble detector spectrometer from Bubble Technology Industries comes with a 90 days warranty, and it is also guaranteed the bubble detectors can be reused for more than ten cycles. The bubble detectors are stored at low temperature (~ 5 ℃) in a cooler to reduce their sensitivity. Still, bubbles may be formed in the detectors due to background radiation. If these bubbles are not recompressed within a few days, they will

Figure 7.5: Bubble detectors with signs of aging. The detector to the left has two large bubbles which are not possible to recompress into droplets using the recompression chamber. On the right, several small bubbles are trapped against the detector wall. These are known as surface bubbles. These effects will tend to make it more difficult to count the number of bubbles in the detectors.

grow and make it impossible to recompress them into droplets using the recompression chamber.

An example of a detector with uncompressable bubbles is shown to the left in figure 7.5. According to the manufacturer, these bubbles should not change the response of the detectors besides the fact that the effective detector volume will become smaller. However, it may in some cases make it more difficult to count the bubbles manually. Another effect that can complicate the counting process is the formation of so-called surface bubbles. These are small bubbles trapped against the detector wall, which may appear after several times use and in general do not disappear during recompressing. Figure 7.5 also shows a detector with such surface bubbles. In addition to these signs of aging, the fact that the detector gel is a water based medium results in a swelling of the top part of the detector gel as this part has been exposed to water during recompression. After many times use, water droplets would in some cases penetrate into the effective detector area causing a small change in the total detector volume sensitive to radiation. This effect will also have an impact on the lifetime of the detectors.

To measure if the sensitivity of the bubble detectors changes over

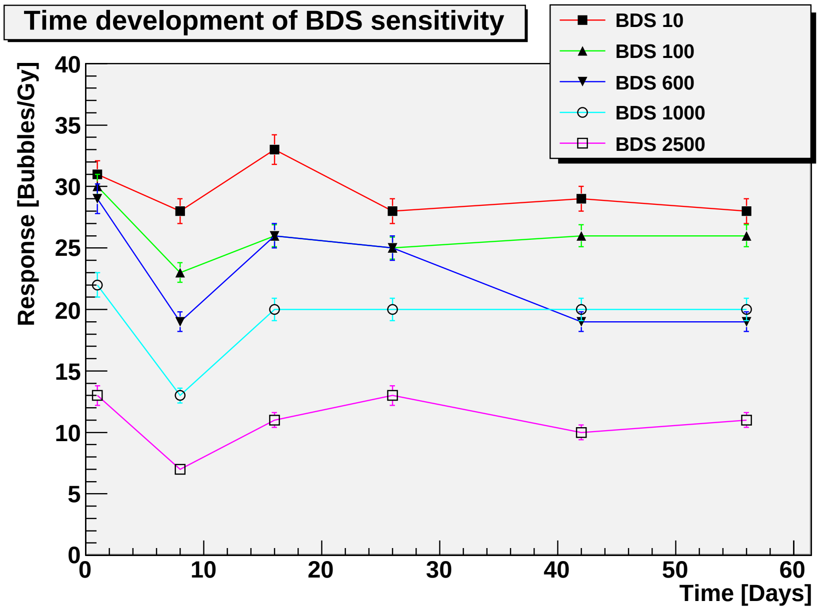

Figure 7.6: The time development of the BDS detectors sensitivity. One detector of each subgroup was used for a series of measurements over a period of about two months. The first measurement was conducted on 5th of March, about two months after the initial activation of the detectors. No clear trend can be deduced from these measurements.

time, one detector of each category from the BDS was irradiated under equal conditions repeatedly over a period of about two months. The results from these tests are shown in figure 7.6.

Although the time development data do not show a significant drop in the detectors' sensitivity over time, other measurements reveal that individual detectors seems to have a lower sensitivity after some time compared to the initial sensitivity. An example of this is given in figure 7.7 where the response from several measurements conducted with a BDS-10 detector has been plotted as a function of time. A drop in the sensitivity of about 100% can be seen here suggesting that changes in sensitivity can be larger than what figure 7.6 indicates. Another example of this is illustrated in figure 7.8. Here, the response for the 6 BDS-10 detectors is shown. This was the last measurement performed in this study, and the results reveal that the spread in the detectors' sensitivity has increased significantly. The difference from the least sensitive detector to the most sensitive is almost an order of magnitude. From this it is evident that the sensitivity of the detectors should be tested regularly to ensure reliable measurements.

The high doses that some of the detectors received in the carbon

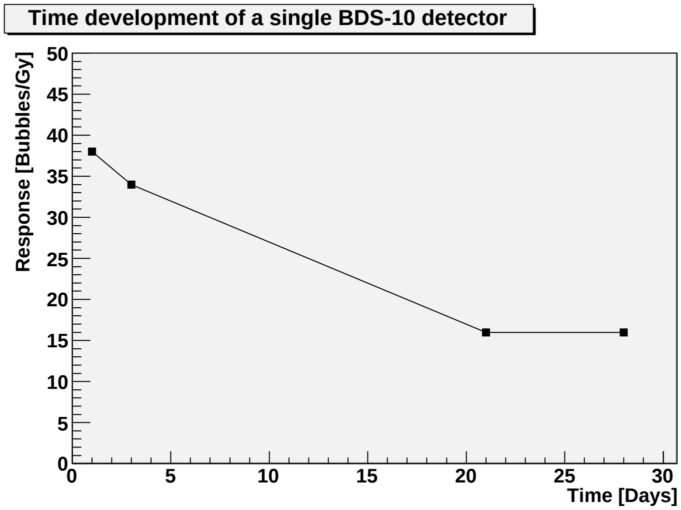

Figure 7.7: Normalized response of a single BDS-10 detector. Results are shown for measurements done in the time between the 3rd and 30th of March. A significant fall in sensitivity is observed.

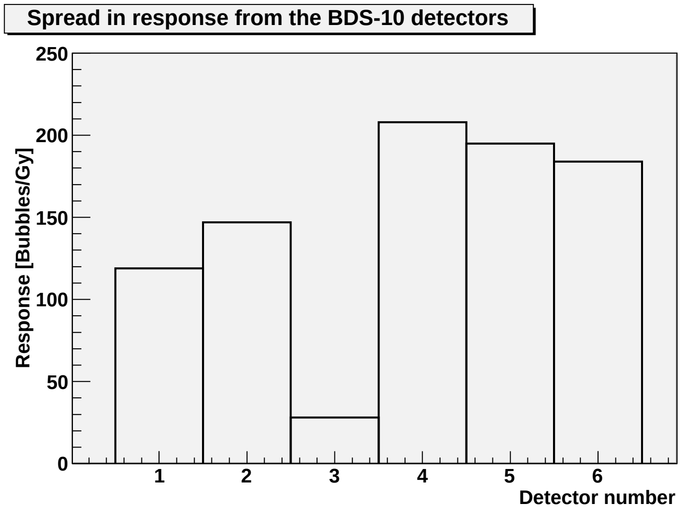

Figure 7.8: Normalized response for the last measurement with the BDS-10 detectors in this work. The response for all 6 detectors is shown. These measurements were performed without the phantom. Hence, the response is not comparable to that in figures 7.7 and 7.6.

beam experiment might be partly responsible to the drop in sensitivity. In the carbon beam measurements, more than 1000 bubbles were produced in some of the irradiation sessions. The manufacturer has not given any clear indications that high radiation doses can change the detectors' properties, but if this is the case, caution should be taken especially when performing experiments in high energy particle beams.

7.2 Neutron Source Measurements

An Americium-241/Beryllium Neutron source with a nominal activity of 1 Curie was used to perform tests of the bubble detectors and the TLDs. The neutron radiation dose rate from the source was measured by GSI physicists to be 23.9 μSv/h at a distance of 1 meter. As time was limited, a higher dose rate was necessary in order to achieve sufficient statistics. Calculations (Eq: 7.1) showed that the dose rate was about 3 mSv/h at a distance of 9 cm from the source. Figure 7.9 illustrates the neutron energy spectrum from the AmBe-source.

$$23.9\mu Sv/h \times \frac{(100cm)^2}{(9cm)^2} = 2951\mu Sv/h \tag{7.1}$$

It was assumed that the dose rate is inversely proportional to the distance to the source. This may lead to some errors, especially at low distances to the source.

7.2.1 Spectrum measurements with the BDS

The objective of this experiment was to see if the BDS detectors could reproduce the neutron energy spectrum shown in figure 7.9. As mentioned in section 5.2.3, only a 6 region histogram spectrum can be obtained from the BDS detectors, and this will consequently not present the same degree of detail in the spectrum. The temperature in the measurement room was not measured, but it was clearly below 20 ℃. This indicates that the bubble detectors' sensitivity at the temperature in the experimental room might be lower than the values given in the calibration certificates for 20 ℃.

Figure 7.10 shows the results from irradiation of the bubble detectors in units of bubbles per mSv theoretical neutron dose. In figure 7.11, the response has been converted to dose using the bubbles-to-dose conversion factors, provided by the vendor with each single detector. This conversion factor seems to only give an indication of the magnitude of the neutron dose, and might not always give an accurate estimate

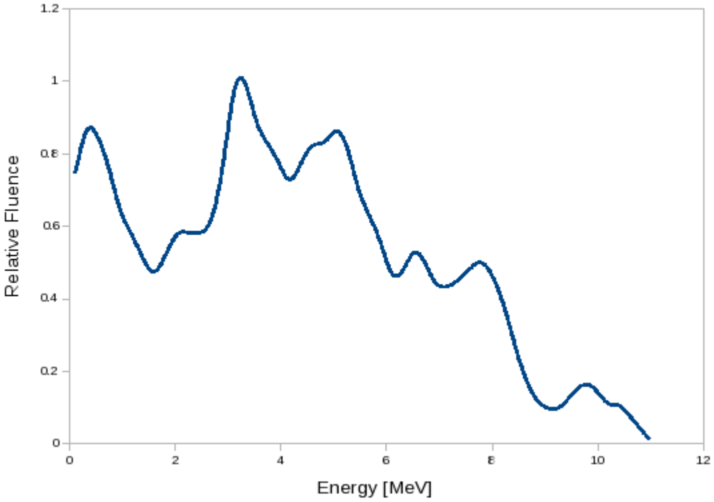

Figure 7.9: Neutron energy spectrum from the AmBe-source. Roughly 80% of the neutrons have energies in the interval 2.5 - 10 MeV, while the remaining neutrons mainly have lower energies.

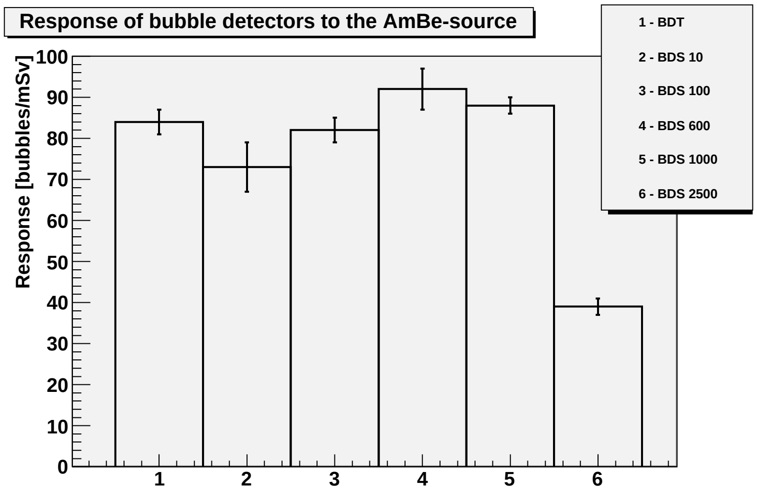

Figure 7.10: Response from the various bubble detectors in units of bubbles to a theoretical neutron dose of 1 mSv.

of the dose. The spectrum, shown in figure 7.13, is not representative for the true neutron energy distribution from the AmBe-source. This is not surprising as the unfolding procedure is based on detector response at 20 ℃, and the results of the temperature dependence measurements shows that large errors may occur when measuring at other temperatures.

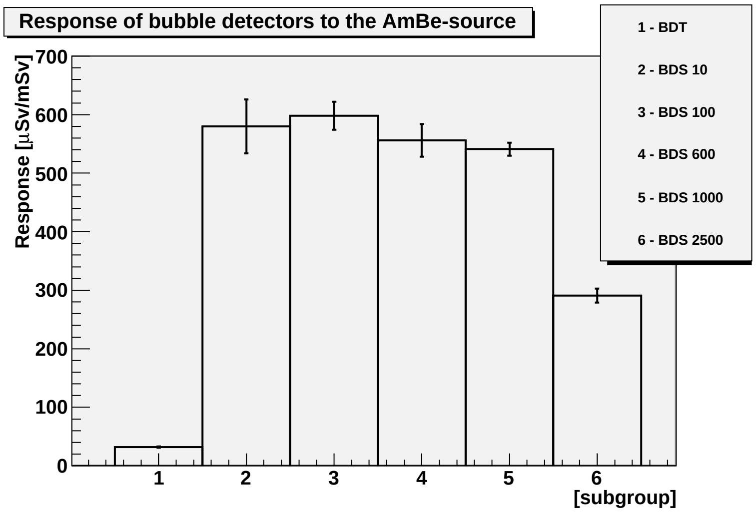

Figure 7.11: Response from the various bubble detectors to a theoretical neutron dose of 1 mSv. The response in bubbles have been converted to dose using the bubbles-to-dose conversion factors discussed in section 5.2.3.

The spectrum shown in figure 7.13 is represented using log scales. To better illustrate the following spectra presented, zero suppression is applied to those. The energy interval which do not appear in the spectra can be assumed to be empty.

Although the exact temperature was not known, a temperature corrected response chart and neutron spectrum have also been plotted. These are shown in figure 7.12 and 7.14, respectively. Here, a room temperature of 15 ℃ was assumed, and the temperature correction factors are obtained from the results found in section 7.1.3. While the uncorrected spectrum shows that the neutron fluence is largest in the area 1 - 2.5 MeV, the corrected spectrum indicates a slightly higher fluence in the interval 2.5 - 10 MeV than that in the lower interval. Although non of the spectra are representative for the true energy distribution of the neutrons, the temperature corrected spectrum shows better agreement with the theoretical spectrum than the uncorrected data do. If the exact temperature in the room was known, it may have been possible to better correct all the collected data.

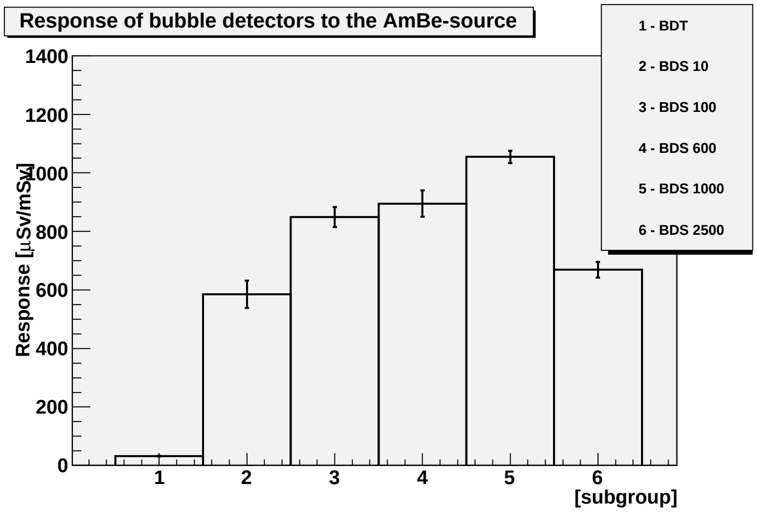

Figure 7.12: Temperature corrected response from the various bubble detectors to a theoretical neutron dose of 1 mSv. The response is normalized to response at 20 ℃ assuming the temperature in the room was 15 ℃ during the measurements, and the response in bubbles have been converted to dose using the bubbles-to-dose conversion factors discussed in section 5.2.3.

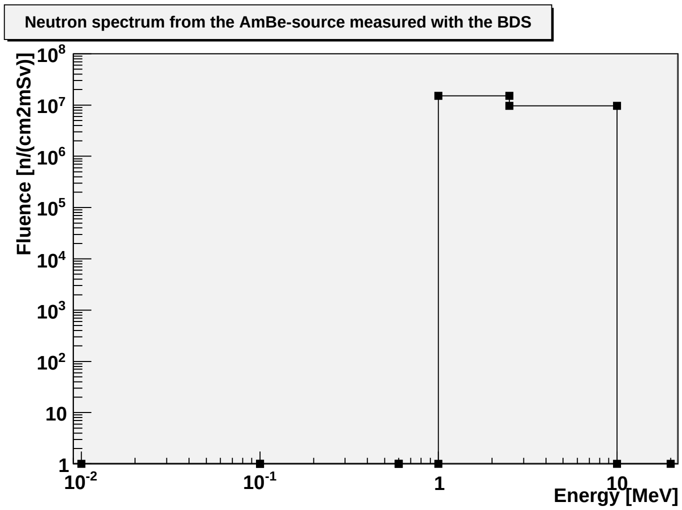

Figure 7.13: Unfolding of the BDS detectors' response to the AmBe source. Comparing it to the theoretical spectrum (figure 7.9) shows that the unfolded data do not represent the true spectrum. The unfolding procedure is based on the detectors' response at 20 ℃ and the data indicates that measuring at other temperatures may give misleading results.

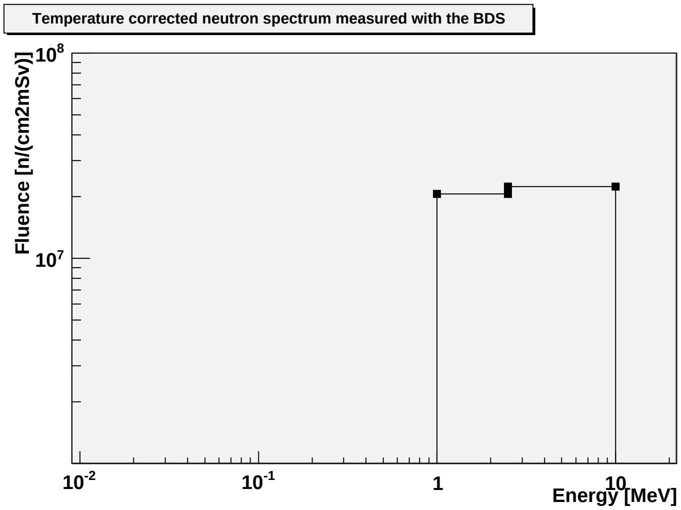

Figure 7.14: Temperature corrected spectrum from the AmBe source. The measured sensitivity changes from 20℃ to 15 ℃ have here been taken into account. It can be seen that the fluence in the interval 2.5 - 10 MeV is larger than in the interval 1- 2.5 MeV. The corrected spectrum is more in agreement with the true spectrum 7.9 than the uncorrected spectrum.

7.2.2 Thermal neutron measurements

Both bubble detectors (BDT) and thermoluminescence detectors were used to measure the thermal component of the neutrons emitted from the AmBe source. Because of the lack of calibration of the TLDs, no conclusions could be drawn from the TLD measurements, and the results are not discussed further in this thesis. As discussed earlier, the BDT detectors have a sensitivity to thermal neutrons a factor ten higher than to fast neutrons. Because the source is not moderated, the fast neutrons a expected to dominate the response from the BDT detectors, and this can be expected to be about a factor 10 lower than for the BDS detectors. Figure 7.11 shows that the measurements are to some extent in agreement with this.

7.3 Photon Beam Measurements

As discussed in section 2.2.2, the neutron spectrum from a medical linac is expected to be dominated by neutrons with energies around 1 MeV produced from the evaporation process. In addition, a smaller component from the direct knockout effect should be observed. For the measurements inside the phantom it is expected that the neutron energies are shifted downwards in energy compared to the original spectrum.

In the spectrum measurements, all detectors except the BDS-10000 detectors, were used. Some measurements were performed with the BDS-10000 detectors, and the results indicated that very few neutrons with energy above 10 MeV were present in the radiation field. The dose due to neutrons above 10 MeV was in the order of 1 μSv per Gray or less. From these preliminary tests with the BDS-10000, it was decided that it was not necessary to include these detectors in the spectrum measurement series. An extremely large photon dose would have had to be applied in order to achieve sufficient statistics if they were to be included.

7.3.1 Isocenter plane spectrum

Measurement with the BDS were performed in the isocenter plane without the phantom. The detectors were placed 4 cm off axis from the beam in the isocenter plane as described in section 6.2. All the detectors, except the BDS-10000 detectors, were irradiated twice. The experiment was the last performed in this work, and consequently the bubble detectors were already used many times and showed signs of aging. The response from two of the 30 detectors was ignored because the response from these detectors showed deviations from the mean of more than 300%. The signs of aging in the detectors decreased the confidence in the results, but on the other hand, the measurement procedure was more standardized, and factors like temperature were better controlled than in measurements conducted at an early stage in the project.

The spectrum shown in figure 7.15 is to some extent in agreement with the Monte Carlo simulations shown at the bottom of the figure. The measured spectrum shows no neutrons in the two lower energy regions (0.01 - 0. 6 MeV), but the general trend in the spectrum indicates a peak in the fluence just below 1 MeV and a neutron fluence in the interval 2.5 - 10 MeV which is about an order of magnitude less. This corresponds well to the simulated data with a dominant neutron component from evaporation below 1 MeV and a smaller contribution in the energy interval 1 - 10 MeV originating from the direct knockout effect.

The integral fluence of the spectrum is discussed in section 7.3.3 and compared to fluence in Monte Carlo simulations and in-phantom measurements. Due to the long time use the detectors had been exposed to prior to the measurements, the uncertainties in the spectrum are large. The measurements indicate that the rms values calculated at an

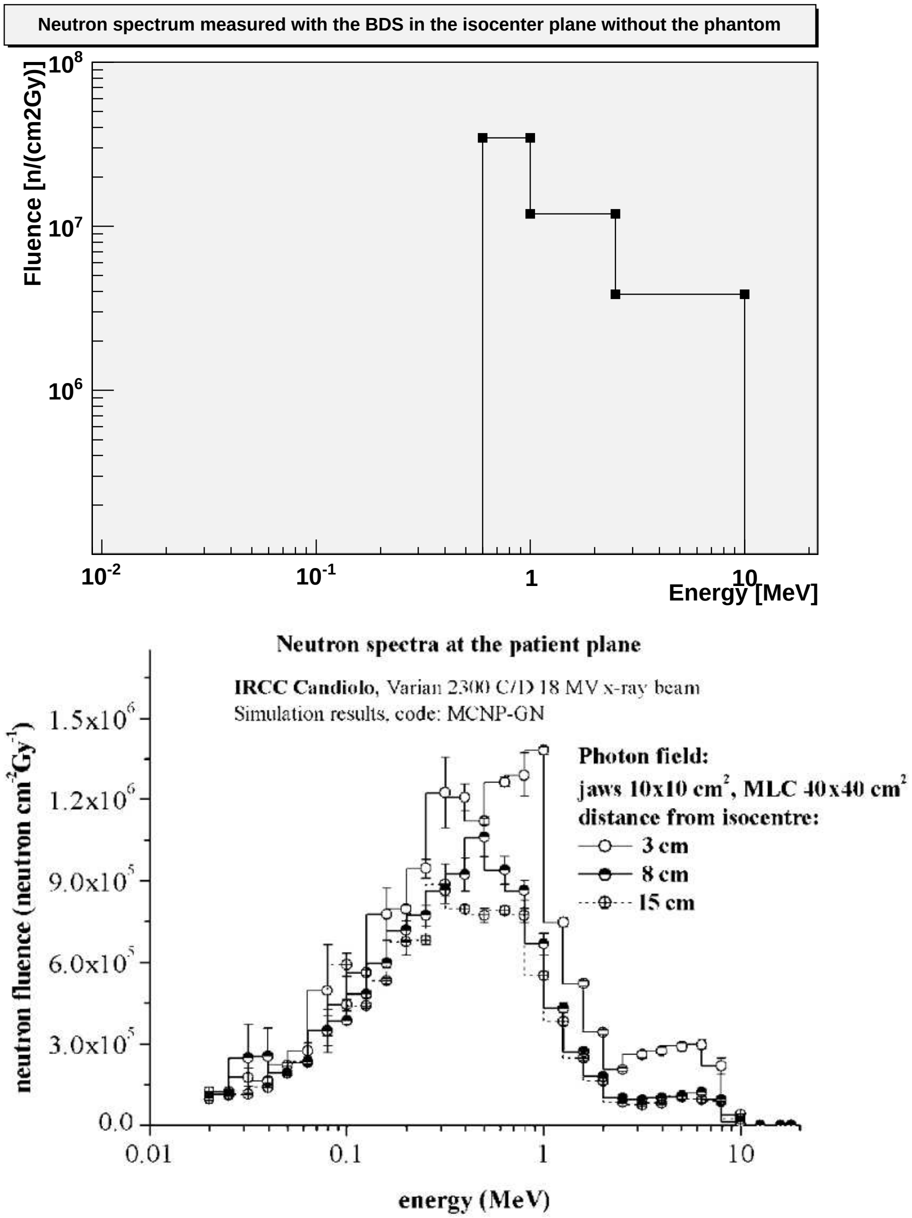

Figure 7.15: Neutron spectrum measured in the isocenter plane as described in section 6.2. The top figure shows the neutron spectrum obtained from the measurements. The spectrum underneath is obtained from Monte Carlo simulations of neutrons from a 18 MeV linac [5]. Uncertainties in the collected data lead to errors in the unfolding process resulting in zero neutron fluence in the lower energy regions.

earlier stage (see table 7.1) is no longer realistic, and that the estimation of error propagation in the unfolding would not give any realistic information about the uncertainties in the spectrum. The experiment should be repeated with a new BDS set and with more repetitions to achieve higher statistics.

7.3.2 In-phantom spectra

Measurements of the neutron spectrum in 4 different positions inside the plastic phantom were performed by use of the BDS. Positions 4 cm and 8 cm off axis from the beam axis where investigated at depths of 8.6 cm and 12.9 cm in the phantom. The effect of closing the MLCs was also investigated through measurements in positions 8 and 9 in the phantom with open and closed MLCs.

Figure 7.16 shows the energy spectra obtained 4 cm (position 9) and 8 cm from the beam axis at 8.6 cm depth. The energy interval between 0.6 and 1 MeV shows zero fluence, but apart from this, the energy spectra are dominated by neutrons of energies below 0.6 MeV. Because neutrons are moderated as they traverse through the phantom, it is expected that the neutron spectra are shifted downward with respect to energy compared to the measurements conducted without the phantom. The results indicate that a large part of the neutron from the evaporation process have been moderated.

For the positions at 12.9 cm depth in the phantom, shown in figure 7.17, the response from the detectors was significantly lower. The 8 cm off axis results (position 14) indicate the same trend as the results from positions 8 and 9. That is, a downwards shift in the energy distribution compared to the measurements without the phantom. In position 15, 4 cm off axis, only one energy interval shows a positive value. This indicates that the errors in these measurements may be large, and it is difficult to draw any conclusion from the results.

Figure 7.18 shows the spectra obtained for measurements with open and closed MLCs in positions 8 and 9. The trend for the measurements was that the response from the detectors was substantially lower with the MLCs closed. As it can be seen in the figure, the spectra have intervals with zero fluence, indicating that the uncertainties are large. The neutrons produced prior to the MLCs may be moderated and the neutron flux may be reduced as they pass through the MLCs. At the same time, photons incident on the MLCs will cause production of additional photoneutrons. No conclusive information can be drawn concerning the effect of the MLCs.

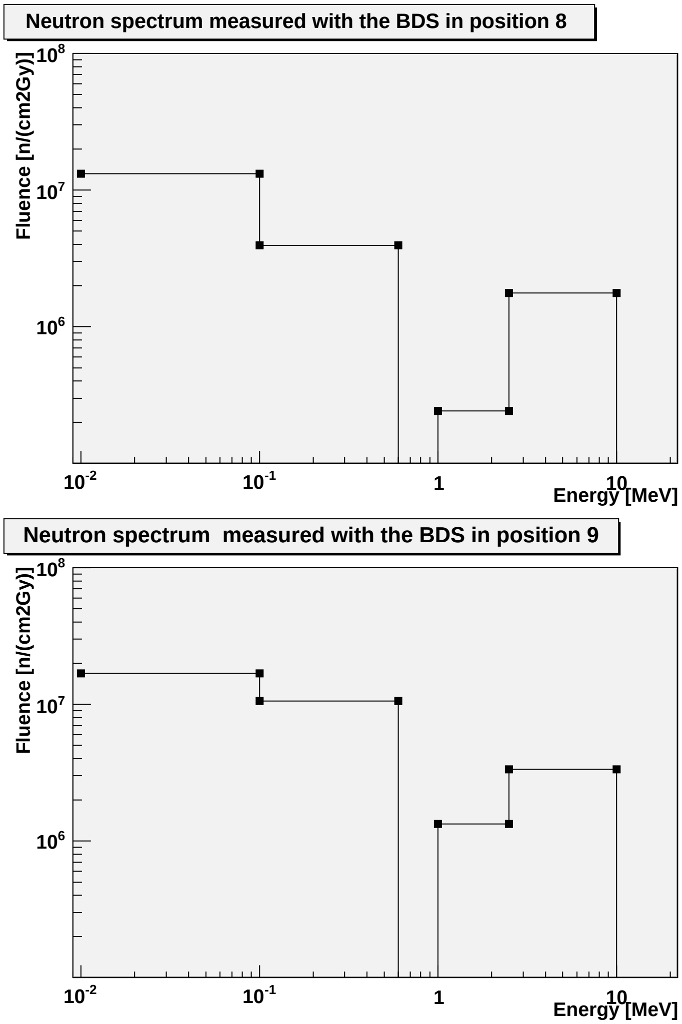

Figure 7.16: Neutron spectra measured with the BDS in positions 8 and 9. These positions are 8 and 4 cm from the beam axis, respectively, at 8.6 cm depth in the phantom. Uncertainties in the collected data lead to errors in the unfolding process resulting in some energy intervals with zero neutron fluence.

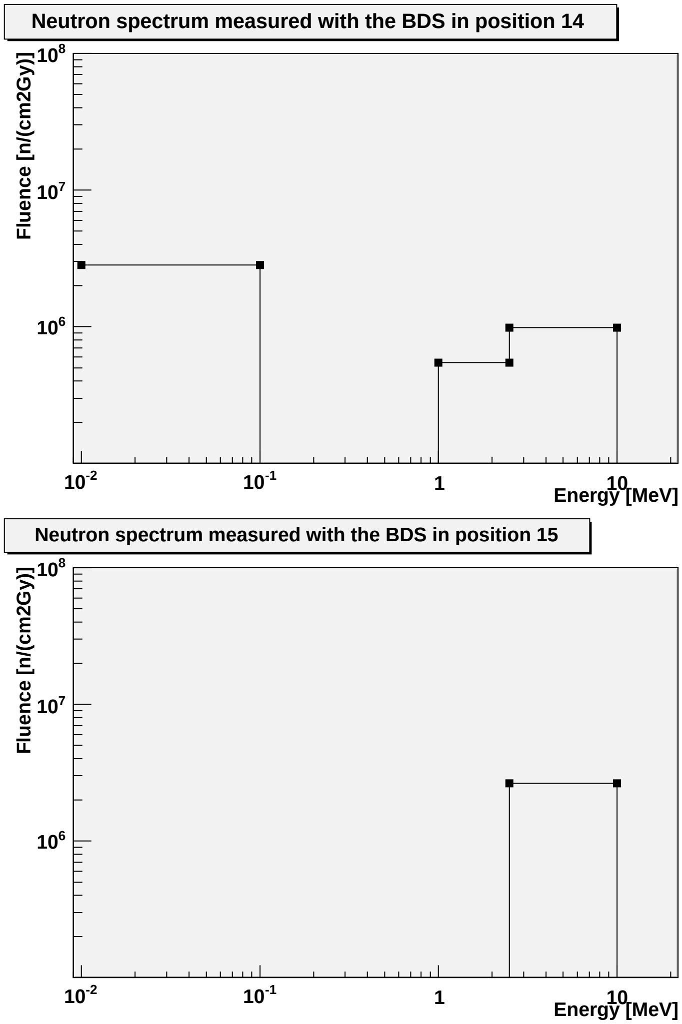

Figure 7.17: Neutron spectra measured with the BDS in positions 14 and 15. These positions are 8 and 4 cm from the beam axis, respectively, at 12.9 cm depth in the phantom.Uncertainties in the collected data lead to large errors in the unfolding process resulting in several energy intervals with zero neutron fluence.

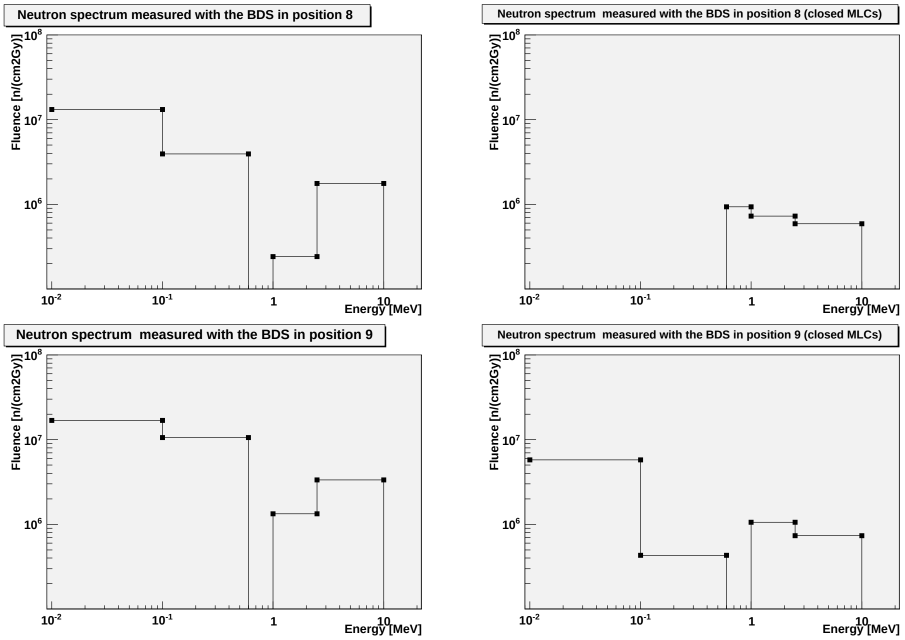

Figure 7.18: Comparison of neutron spectra measured with the BDS with open and closed MLCs.

7.3.3 Integral fluence and equivalent dose

To get an indication of the reliability of the measured neutron fluences in this work, comparisons to Monte Carlo simulations of other photoneutron fields are useful. In an article by C. Ongaro et al [5] photoneutron energy distributions, integral fluence and dose equivalents in the isocenter plane from a 18 MeV medical linac were calculated. In the simulations no phantom was used, meaning that the measurements in free air are best suited for comparison. Unfortunately, no relevant data for in-phantom spectrum measurements or simulation for comparison with the results in this work has been found. The simulations are based on the following three different setting

1. A 10 × 10 cm^2 photon field with MLCs extracted to 40 × 40 cm^2
2. A 10 × 10 cm^2 photon field with jaws at 40 × 40 cm^2 and MLCs at 10 × 10 cm^2
3. A clinical configuration with jaws at 10 × 10 cm^2 and MLCs defining a cross section of a treatment volume.

The fluence from the simulations, given in figure 7.19, is based on an average value of the three configurations, obtained at 4 cm distance from the beam axis. The photon dose was estimated at the dose maximum which is located at 3 cm depth in water for 18 MeV photons. In measurements performed in this thesis, the photon dose was estimated in the isocenter located 8.6 cm inside the plastic phantom. In addition, a 5 × 5 cm^2 photon field was used in contrast to the 10 × 10 cm^2 field used in the simulations, and, as mentioned, the photon energy during measurements was 15 MeV. For these reasons the results are not expected to match perfectly, but they should still be in the same order of magnitude.

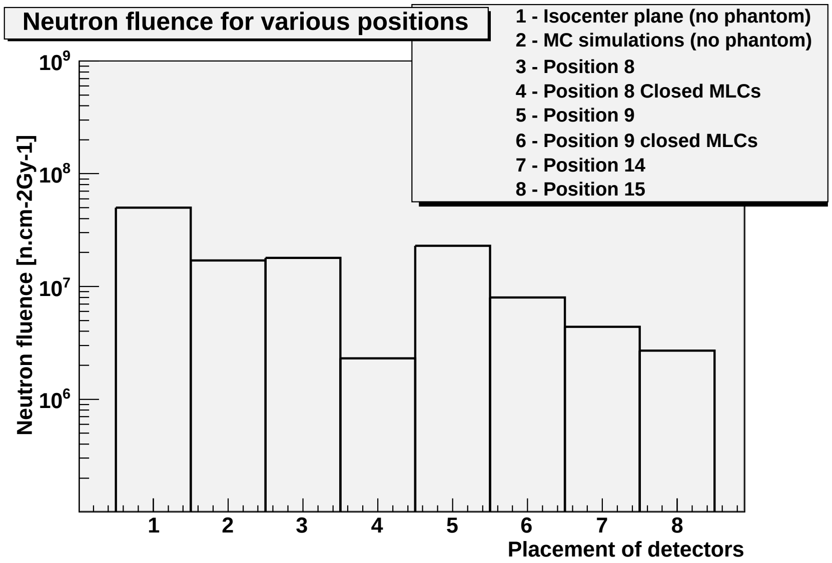

Figure 7.19: Integral 10 keV to 20 MeV neutron fluence per treatment gray of 15 MeV photons measured with the BDS. Also shown for comparison is the integral fluence obtained from Monte Carlo simulations [5] on a 18 MeV linac.

Figure 7.19 shows an overview of the integral fluence measured in the different positions. For comparison, the average fluence from Monte Carlo simulations of a neutron spectrum is also shown. The neutron fluence is highest for the measurements in the isocenter plane without the phantom. A fluence of $5 \times 10^7 n.cm^{-2}Gy^{-1}$ was obtained here. The Monte Carlo simulation for a similar setup in a 18 MeV photon beam shows a fluence which is a little less than half of this. The measurements in the positions at depth 8.6 cm in the phantom (positions 8 and 9) indicate a fluence of about $5 \times 10^7 n.cm^{-2}Gy^{-1}$. A drop in fluence of about 20% can be seen when moving from 4 to 8 cm distance to the beam axis at this depth. The results also indicate that the fluence at 12.9 cm depth in the phantom is less than one fifth of the fluence at 8.6

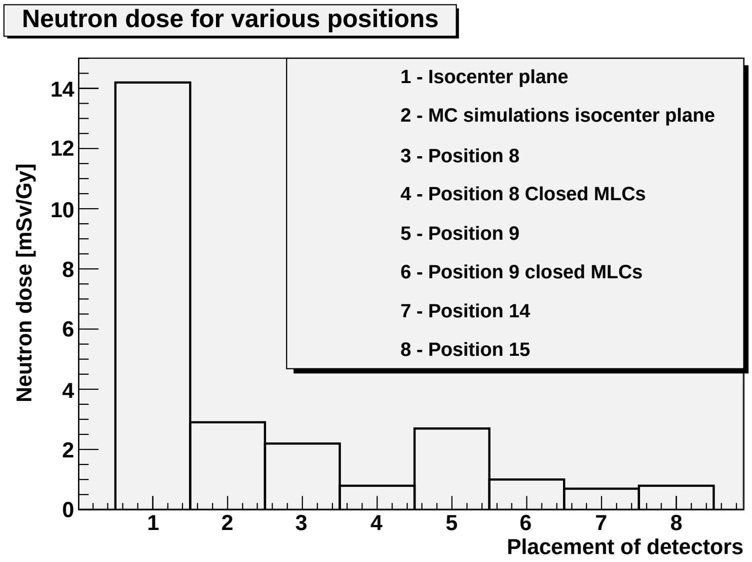

Figure 7.20: Integral 10 keV to 20 MeV neutron dose per treatment gray of 15 MeV photons measured with the BDS. The dose is converted from fluence using the conversion factors in table F.1. Also shown for comparison is the dose obtained from Monte Carlo simulations [5] on a 18 MeV linac.

cm depth. The data from the measurements with closed MLCs show a fluence of $5 \times 10^6 n.cm^{-2}Gy^{-1}$ on average for the positions at 8.6 cm depth. This lower than the values found with open MLCs at 8.6 cm depth, but higher than the fluence measured at 12.9 cm depth.

From the integral fluences the equivalent neutron doses have been estimated using energy dependent conversion factors (from table F.1) [30]. The calculated equivalent doses are shown in figure 7.20. The dose was estimated to be approximately 14 mSv per Gray for the measurement without the phantom. For the in-phantom measurements the dose was substantially lower. On average for the various positions an equivalent dose of 1.4 mSv per Gray was estimated. The large difference in dose from the measurements without the phantom to the other measurements is both due to lower fluence in the phantom and that the moderated neutrons have a lower relative biological effectiveness.

7.4 Thermal Neutrons in the Photon Setup

The bubble detector thermal (BDT) was used to measure the thermal neutron component of the radiation field from the medical linac. To obtain the dose from thermal neutrons inside the phantom, a total of 12 measurements were performed in each position using 6 different

BDTs, two times each. The average response and standard deviation, both normalized to 1 Gray, are given in table 7.2. The complete measurement series can be seen in table C.2. The results indicate that the thermal neutron dose is close to constant with respect to lateral distance from the center in the area 4 cm to 8 cm from center. In the depth direction the measured dose is about twice as high at isocenter depth compared to positions 14 and 15 which are located 4.3 cm deeper in the phantom.

Table 7.2: Thermal neutron doses measured with the bubble detector thermal (BDT). The dose is given in units of μSv per Gray photon dose. While dose variations with distance from the beam axis is small, the dose decreases significantly with depth.

Position	Average response [μSv/Gy]	σ [μSv/Gy]	σ[%]
8	146	66	45
9	148	57	39
14	66	40	61
15	67	57	85

The spread in sensitivity between the BDT detectors was found to be relatively large. The standard deviations for the measurements are given in table 7.2. A reason for the large spread may be that some of the detectors received a too high dose during the experiment with the ^{12}C beam at GSI.

7.5 Carbon beam measurements

Shown in this section are the results from measurements in a 200 MeV/u carbon beam at GSI-Darmstadt in Germany. Bubble detectors of types BDS-10, BDS-2500 and BDS-10000 were used. When measuring dose from the carbon beam at GSI, the radiation field inside the phantom will consist of several components. Neutrons, protons and heavier fragments are present in addition to the primary ^{12}C beam.

The primary beam is a narrow pencil beam with a diameter of about 6 mm, but it will be somewhat spread out as it passes through tissue. Looking at figure 3.3 and 6.7 it is evident that lateral scattering of the primary beam will not affect the measurements performed as the measurements are done 4 and 8 cm off axis from the beam, and the lateral scattering of the carbon ions is on the order of millimeters at this range. The distribution of nuclear fragments from the primary beam will in general be more forward peaked than for protons. This implies that neutrons and protons will be the dominant sources of dose

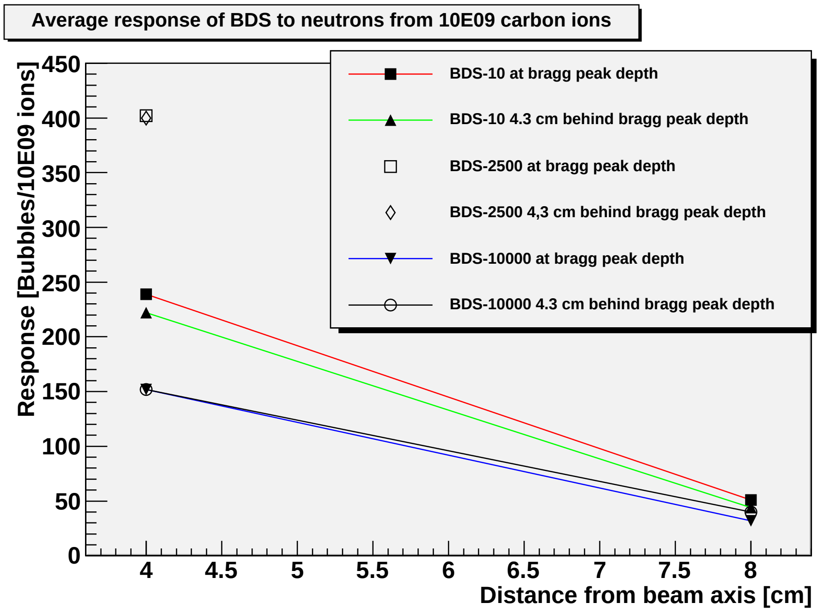

Figure 7.21: Response of the BDS detectors at Bragg peak depth and 4.3 cm behind the Bragg peak as a function of distance from the beam axis. The response is given in units of bubbles per 10^9 primary carbon ions. No measurements were performed 8 cm off axis with the BDS-2500 detectors.

deposition in the positions used for this experiment. As discussed in the section on bubble detectors, their sensitivity to protons is expected to be about one order of magnitude less than to neutrons. The response to neutrons with energy above 20 MeV is not known for these BDS and this, together with the protons present in the field, makes it is difficult to convert the response in number of bubbles to neutron dose in Sievert.

Prior to the experiments in the carbon beam, the temperature dependence of the bubble detectors' sensitivity was not known, but tests presented in section 7.1.3, indicate that temperature variations may have large influence on the experimental results. The temperature in the experimental room at GSI was 22 ℃, and the temperature of the water used for recompression was not measured.

As mentioned earlier, the bubble detectors have been calibrated at 20 ℃. From figure 7.4 and table C.1 it is seen that a temperature change of ± 5 ℃ may result in errors of more than 100%. This emphasizes the importance of controlling the temperature. However, the situation in the carbon beam setup differs from the photon beam setup concerning energy of the detected particles. The neutron energy is mainly below 10 MeV in the photon beam, while in the carbon setup, neutrons with

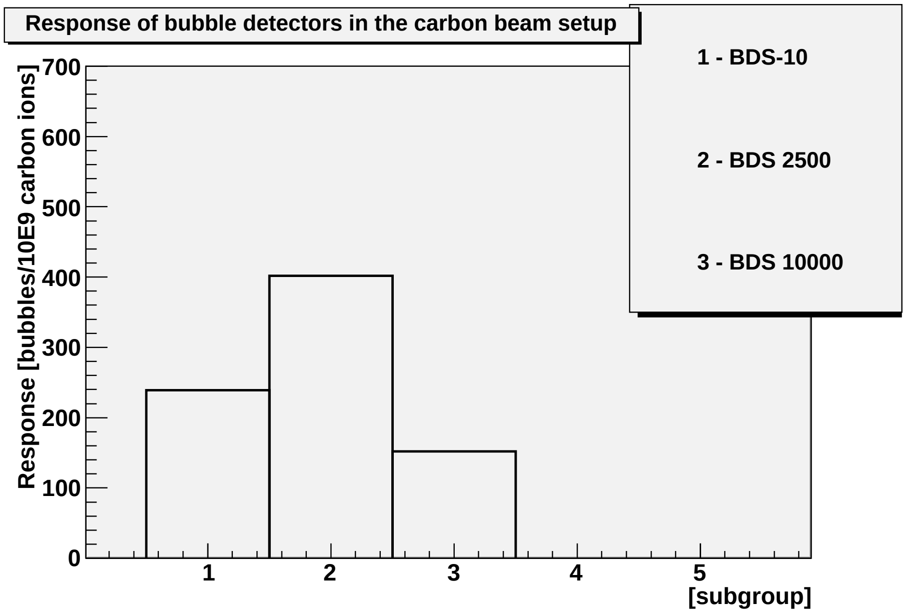

Figure 7.22: Response of the BDS detectors at Bragg peak depth 4 cm from the beam axis. The response is given in units of bubbles per 10^9 primary carbon ions. As seen, only the subgroups BDS-10, BDS-2500 and BDS-10000 were used.

energies of several hundred MeV are present. In a neutron field dominated by high energy neutrons, the temperature might not be that critical to the response from the bubble detectors, because the changes in sensitivity with temperature is believed to mainly be due to a lowering of the detector thresholds. The temperature dependence of the bubble detectors' response to high energy neutrons is an issue which would be interesting to investigate.

Tables 7.3 and 7.4 show the results from the carbon beam. The response is given in bubbles per 10^9 primary carbon ions. The results indicate that the neutron dose is close to constant in the depth direction from the bragg peak and to the next measuring point, which is located about 4.3 cm deeper in the phantom. For the measurements at 8 cm off axis, only one irradiation of the detectors BDS-10 and BDS-10000 in each position was carried out due to lack of time. This means that the statistics are much lower than what would be ideal, but it still gives an indication of the rate the dose drops when moving away from the beam axis. The response at 8 cm off axis is on average about a factor 5 lower compared to that at 4 cm off axis.

It is evident that the different types of bubble detectors do not have the same sensitivity for high energy neutron. If they did, it would

Table 7.3: Average response at Bragg peak (BP) depth and 4.3 cm behind the Bragg peak, 4 cm off axis from the 200 MeV/u ^{12}C pencil beam. The response is given in bubbles per 10^9 ions. From the results it seems that the neutron dose is close to constant in the depth direction over the measured area.

Detector	Response at BP [b/10^9ions]	Res. behind BP [b/10^9ions]
BDS 10	239	222
BDS 2500	402	400
BDS 10000	152	152

Table 7.4: Response at Bragg peak (BP) depth and 4.3 cm behind the Bragg peak, 8 cm off axis from the 200 MeV/u ^{12}C pencil beam.

Detector	Response at BP [b/10^9ions]	Res. behind BP [b/10^9ions]
BDS 10	51	44
BDS 10000	32	40

be expected that the BDS-10 gave the highest response because this detector covers the largest range of energies ($E_n > 10$ keV), in fact, the results indicate that the BDS-2500 are the detectors most sensitive to neutrons of energies above 20 MeV. This is illustrated in figure 7.22. The BDS-10000 are, by the manufacturer, calibrated to have a sensitivity of about 0.05 bubbles per μSv for neutron energies between 10 and 20 MeV, while the BDS-10 and BDS-2500 are known to have an average sensitivity of roughly 0.13 bubbles per μSv. From this it is understandable that the BDS-10000 could give a lower response than the other detectors, also in a radiation field with particle energies exceeding 20 MeV.

As an indication of how much dose 10^9 ions corresponds to, it can be mentioned that when treating a volume of $5 \times 5 \times 5\ cm^3$, 10^9 ions would approximately correspond to a dose of 1.2 GyE (Cobolt Gray equivalent) [9]. This can not be directly compared to the dose in Gray in the isocenter of the photon beam setup, but could be compared to a photon treatment plan delivering 1.2 Gray in the same volume.

To get an indication of the neutron dose measured, it can be assumed that the bubble detectors' response to neutron with energies above 20 MeV was similar to the detectors' response to neutrons of lower energies. The detectors' individual conversion factors (from the vendor's calibration) from bubbles to neutron dose can then be applied. Then, it has also been assumed that the part of the response from the detectors originating from protons was negligible, and that the temperature during measurements was close to 20 ℃. With all these assumptions, the neutron dose 4 cm off axis, at Bragg peak depth and 4.3 cm deeper, was found to be in the order of 2 mSv/GyE based on the treatment of the 5 × 5 × 5 cm^3 target volume, as discussed earlier in this section. The response, and thus the dose, at 8 cm off axis was found to be about a factor 5 lower.

It must be emphasized that a detailed study of the bubble detectors' response to high energy neutrons is necessary before reliable neutron doses from ion therapy can be obtained by the use of the BDS detectors. Investigations of the influence that protons and other fragments may have on neutron dose measurements are also essential, e.g. testing the BDS detectors' response to protons and various nuclear fragments over a wide energy range.

Chapter 8

Conclusion

This study has been performed in order to gain knowledge in the fields of radiotherapy, neutron dosimetry and the neutron doses related to radiotherapy with photons and hadrons. Bubble detectors were used to investigate neutron doses both from radiotherapy with photons and particle therapy using ^{12}C ions.

Through the work done in this thesis, a more accurate procedure for measuring with bubble detectors in the radiation field from a medical linac has been acquired. This may make it possible to conduct future experiments with lower uncertainties than in the measurements presented in this thesis. Important factors in measurements are controlling the temperature of the detectors as accurately as possible, and to be aware of the spread in sensitivity between the detectors in a batch.

Measurements with the AmBe neutron source, showed that measurements of neutron spectra should be performed at 20 ℃. An attempt to correct for the temperature was made, and the corrected spectrum was closer to the assumed true neutron spectrum than the uncorrected data was. If the temperature sensitivity of the BDS detectors is closely investigated, correction factors may contribute to accurate measurements at other temperatures as well.

The tests of the BDS detector sensitivity's temperature dependence indicate that an increase of 2 ℃ from 20 to 22 ℃ may result in a rise in the response of up to 50% in individual measurements. The results also indicate that the detectors with high energy thresholds are more sensitive to temperature changes than the low energy threshold detectors. These results agree with previous work on this topic [29].

A series of measurements were performed with the BDS detectors in order to investigate the uncertainty in their response, and to gain knowledge about which factors that may influence the detectors' sensitivity. Results from these response measurements show that the reproducibility from single BDS detector measurements have a rms value in the order of 10%. The rms in the spread in response between the detectors was found to be up to about 20%.

The measurements showed that the bubble detectors after some time show signs of aging and drop in sensitivity. This is important to take into account when considering that the manufacturer reports that the calibration values will be valid for three months. The lifetime of the detector may depend on the dose received, how many recompression cycles they have gone through and how the detectors are stored, i.e. storage temperature and radiation present during storage. The development of the detectors response is an issue that would be interesting to investigate further. If bubble detectors are used for a period of time extending towards three months, the sensitivity of the detectors should be tested regularly.

In the measurement series performed towards the end of this study, it was evident that the sensitivity had dropped significantly for several detectors, and that they no longer could not be used for precise measurement. Detectors that repeatedly show large deviations from the mean should be discarded.

The results from the measurements in the 15 MeV photon beam at Haukeland University Hospital, indicate that the neutron doses are in the order of mSv per Gray. Compared to the estimated dose in free air, the estimated doses inside the phantom at depths 8.6 cm and 12.9 cm were about a factor of 6 and 14 lower respectively. A lower dose inside the phantom is expected both due to moderation of neutrons, which results in a lower biological effectiveness for the photons, and due to attenuation of the neutron flux.

Fluence calculations show that the integral neutron fluence per Gray was in the order of 10^7 $n.cm^{-2}$. For the free air measurements an integral fluence of 5×10^7 $n.cm^{-2}Gy^{-1}$ was found. This is in the same order of magnitude as simulation results for photoneutron fluences in the isocenter plane for other medical linacs [5]. The neutron fluence at 8.6 cm depth was found to be about half of that in free air, and at 12.9 cm depth, results showed a fluence about an order of magnitude less than in the isocenter plane with no phantom. It must again be emphasized that the experimental uncertainties were significant and that new measurements should be performed to achieve more accurate results.

The bubble detectors' sensitivity to high energy neutrons was not defined in this work. Consequently, no equivalent neutron doses were obtained from the experiment in the carbon beam. Thus, a realistic comparison of the neutron doses from radiotherapy with photons and heavy ion therapy is not feasible from the experimental results in this study. However, it is possible to see some of the advantages of using a treatment modality without collimators. When moving away from the target volume in the lateral direction with respect to the beam axis, the results indicate that the neutron dose will drop faster if a carbon pencil beam is used, compared to a collimated photon beam.

Approximately 5×10^5 bubbles from the bubble detectors have been counted manually in this work. This is a time consuming process, and for that reason, the use of an automatic bubble counter is recommended for similar studies.

The work done in this thesis may contribute to enhance the knowledge concerning use of bubble detectors in further studies on neutron doses to patients during photon and hadron therapy irradiation of cancer patients.

Bibliography

[1] Howell R M et al. Investigation of secondary neutron dose for 18 MV dynamic MLC IMRT delivery. *Med. phys*, 32(3):786–93, 2005.

[2] William R. Leo. *Techniques for nuclear and particle physics experiments*. Springer verlag, second edition, 1994.

[3] Faiz M. Khan. *The physics of radiation therapy*. Lippincott Williams and Wilkins, 351 West Camden st. Baltimore, USA, second edition, 1994.

[4] NCRP. Neutron contamination from medical electron accelerators. Technical Report Report No. 79, National Council on Radiation Protection and Measurement, 1984.

[5] A Zanini et al. Monte carlo simulation of the photoneutron field in linac radiotherapy treatments with different collimation systems. *Phys med biol*, 49:571–582, 2004.

[6] Robert R Wilson. Radiological use of fast protons. *Radiology*, 47:487–491, 1946.

[7] Particle Therapy Co-Operative Group. Ptcog website. `http://ptcog.web.psi.ch/`, 2009.

[8] Gerhard Kraft. Physics of carbon ions and principles of beam scanning. PTCOG43 Educational Satellite Meeting, 2005.

[9] K Gunzert-Marx, H Iwase, D Schardt, and R S Simon. Secondary beam fragments produced by 200 MeV u^{-1} ^{12}C ions in water and their dose contributions in carbon ion radiotherapy. *New Journal of Physics*, 10(7), 2008.

[10] IBA. IBA webpage. `http://www.iba-worldwide.com/healthcare/radiotherapy/particle-therapy`, 2009.

[11] Gerhard Kraft. Tumor therapy with heavy ions. `www.gsi.de/informationen/verein-tuthe/`, 2007.

[12] Klaus Wille. *The physics of particle accelerators*. Oxford university press, second edition, 2000.

[13] GSI. Gsi webpage. `www.gsi.de/portrait/Broschueren/Therapie/Innovationen\_e.html`, 2009.

[14] ICRP. 1990 recommendations of the ICRP. Technical Report No. 60, International Commission on radiological protection, 1991.

[15] NASA. NASA webpage. `http://www.nasa.gov/audience/foreducators/postsecondary/features`, 2009.

[16] James E. Turner. *Atoms, Radiation and Radiation Protection*. Wiley-VCH, third edition, 2007.

[17] C. F. G. Delaney and E.C. Finch. *Radiation Detectors*. Oxford University Press, first edition, 1992.

[18] R.E Apfel, S.C Roy, and Y.-C Lo. Prediction of the minimum neutron energy to nucleate vapor bubbles in superheated liquids. *Physics Review A*, 31(3194), 1985.

[19] H. R. Andrews et al. LET dependence of bubble detector response to heavy ions. *Radiation protection dosimetry*, 120(1-4):480–484, 2006.

[20] H. Ing, R.A. Noulty, and T.D. McLean. Bubble detectors - a maturing technology. *Radiation Measurements*, 27(1):1–11, 1996.

[21] J. G. Eberhart et al. Metastability limits of superheated liquids: bubble nucleation of hydrocarbons and their mixtures. *Journal of Colloid and Interface Scienece*, 50(369), 1975.

[22] F Seitz. On the theory of the bubble chamber. *Physics and Fluids*, 1(2), 1958.

[23] J. W. Gibbs. The scientific papers of Willard Gibbs. 1, 1961.

[24] M. M. El-Nagdy and M. J. Harris. Experimental study of radiation induced boiling on superheated liquids. *Journal of the British Nuclear Engineering society*, 10(131), 1971.

[25] Masashi Takada et al. Measured proton sensitivities of bubble detectors. *Radiation protection dosimetry*, 111(2):181–189, 2004.

[26] Bubble Technology Industries. BTI bubble detector spectrometer, BDS, for low resoltion neutron spectroscopy - manual. Comes with purchase of BDS neutron spectrometer, 2008.

[27] P. Tume et al. Characterisation of neutron sensitive bubble detectors for applications in the measurement of jet aircrew exposure to natural background radiation. *Nuclear instruments and methods in physics research*, 406:153–168, 1998.

[28] W. E. Shoupp and J. E. Hill. Thresholds for fast neutron fission in thorium and uranium. *Phys. Rev.*, 75(5):785–789, Mar 1949.

[29] M. A. Bucknert, R.A. Noulty, and T. Cousins. Thresholds of bubble technology industries' bubble detector spectrometer. *Radiation protection dosimetry*, 55(1):23–30, 1994.

[30] B.R.L. Siebert and H. Schuhmacher. Quality Factors, Ambient and Personal Dose Equivalent for Neutrons, Based on the New ICRU Stopping Power Data for Protons and Alpha Particles. *Radiat Prot Dosimetry*, 58(3):177–183, 1995.

Appendix A

Particle Therapy Facilities

Table A.1: Proton therapy facilities in operation.

Center	Start of treatment	♯ patients treated
ITEP, Russia	1969	4024
St.Petersburg, Russia	1975	1327
PSI, Switzerland	1984	5076
Dubna, Russia	1999	489
Uppsala, Sweden	1989	929
Clatterbridge, England	1989	1803
Loma Linda, CA, USA	1990	13500
Nice, France	1991	3690
Orsay, France	1991	4497
iThemba labs, South Africa	1993	503
MPRI, IN, USA	2004	632
UCSF, CA, USA	1994	1113
Triumf, Vancouver, Canada	1995	137
PSI, Switzerland	1996	426
HZB Berlin, Germany	1998	1227
NCC, Kashiwa, Japan	1998	607
HIBMC, Hyogo, Japan	2001	2033
PMRC, Tsukuba, Japan	2001	1367
NPTC, Boston, USA	2001	3515
INFN-LNS, Catania, Italy	2002	151
Shizuoka, Japan	2003	692
WERC, Tsuruga, Japan	2002	56
WPTC, Zibo, China	2004	767
MD Anderson, TX, USA	2006	1000
FPTI, FL, USA	2006	988
NCC, South Korea	2007	330

Table A.2: Ion therapy facilities in operation. All centers use carbon ions. *Patients treated at the end of 2007.

Center	Start of treatment	♯ patients treated
HIMAC, Chiba, Japan	1994	4504
GSI Darmstadt, Germany	1997	384*
HIBMC, Hyogo, Japan	2002	454

Table A.3: Particle therapy centers under construction or in a planning stage.

Center	Particle	Planned opening
Med-Austron, Austria	p, C-ion	2013
CNAO, Pavia, Italy	p, C-ion	2010
HIT, Heidelberg, Germany	p, C-ion	2009
PTC, Marburg, Germany	p, C-ion	2010
NRoCK, Kiel, Germany	p, C-ion	2012
Maebashi, Japan	C-ion	2010
RPTC, Munich, Germany	p	2009
PSI, Switzerland	p	2009
UPenn, PA, USA	p	2010
Trento, Italy	p	2011
iThemba Labs, South Africa	p	-
RPTC, Köln, Germany	p	-
WPE, Essen, Germany	p	2009
CPO, Orsay, France	p	2010
Chicago, IL, USA	p	2010
Taipei, Taiwan	p	2011
Oklahoma City, OK, USA	p	2009
Hampton, VA, USA	p	2010
PMHPTC Protvino, Russia	p	2010
CCRS, Bratislava, Slovak. Rep.	p	2010
Ruzomberok, Slovak. Rep.	p	2010
SJFH, Beijing, China	p	2010
Skandion Clinic, Uppsala, Sweden	p	2012

Appendix B

BDS Spectrum Unfolding Procedure

Unfolding of the data from the bubble detector spectrometer is based on a number of assumptions [26]:

1. The derived unfolded spectrum can be adequately approximated by a 6-region histogram.
2. The neutrons detected are assumed to not have higher energy than 20 MeV.
3. Fluence per unit energy is constant over the histogram interval.

Calculations:

1. Count the number of bubbles (A_i) in each detector.
2. Normalize the data by dividing A_i by the sensitivity of the current detector. This gives the standardized response, R_i.

$$R_i = \frac{A_i}{(sensitivity)_i} \tag{B.1}$$

3. Average all the standardized responses for each threshold. This gives six averaged responses where R_1 corresponds to BDS-10, R_2 corresponds to BDS-100 and so on.
4. The neutron fluence in each energy interval, N_i can then be calculated by using the cross sections in various energy intervals given in table B.1.

$$R_6 = \sigma_{66} \times N_6 \tag{B.2}$$

which gives

$$N_6 = \frac{R_6}{\sigma_{66}} \tag{B.3}$$

where σ_{66} is the average response of the BDS-10000 detector over the interval 10 - 20 MeV. N_6 is the total fluence between 10 - 20 MeV.

5. When N_6 is determined it is possible to determine the fluence in the next interval:

$$R_5 = \sigma_{55} \times N_5 + \sigma_{56} \times N_6 \tag{B.4}$$

which leads to

$$N_5 = \frac{R_5 - \sigma_{56} \times N_6}{\sigma_{55}} \tag{B.5}$$

Following this pattern, equations for the remaining energy intervals can also be deduced

$$N_4 = \frac{R_4 - \sigma_{45} \times N_5 - \sigma_{46} \times N_6}{\sigma_{44}} \tag{B.6}$$

$$N_3 = \frac{R_3 - \sigma_{34} \times N_4 - \sigma_{35} \times N_5 - \sigma_{36} \times N_6}{\sigma_{33}} \tag{B.7}$$

$$N_2 = \frac{R_2 - \sigma_{23} \times N_3 - \sigma_{24} \times N_4 - \sigma_{25} \times N_5 - \sigma_{26} \times N_6}{\sigma_{22}} \tag{B.8}$$

$$N_1 = \frac{R_1 - \sigma_{12} \times N_2 - \sigma_{13} \times N_3 - \sigma_{14} \times N_4 - \sigma_{15} \times N_5 - \sigma_{16} \times N_6}{\sigma_{11}} \tag{B.9}$$

If there are few or none neutrons in some energy intervals in the source spectrum, it might happen that one or more of the intervals comes out with a negative fluence. This is due to statistical uncertainties and usually occurs in the lower energy regions as the unfolding can suffer from error accumulation. In such cases it is common to set the fluence for the current interval to zero. This is referred to as the “non-negativity” condition imposed on the spectral unfolding.

6. The total fluence, $\Phi[n.cm^{-2}]$, over the time of detector exposure is given by

$$\Phi = \sum_{n=1}^{6} N_i \tag{B.10}$$

Table B.1: Average cross sections of BDS over various energy ranges [$\frac{bubble}{n.cm^{-2}}$] [26].

Detector I.D.	J =	1	2	3	4	5	6
	MeV	(0.01 - 0.1)	(0.1 - 0.6)	(0.6 - 1)	(1 - 2.5)	(2.5 - 10)	(10 - 20)
BDS-10	1	5.00×10^{-6}	2.50×10^{-5}	2.92×10^{-5}	2.97×10^{-5}	4.15×10^{-5}	4.78×10^{-5}
BDS-100	2	-	2.27×10^{-5}	3.14×10^{-5}	3.23×10^{-5}	4.47×10^{-5}	5.09×10^{-5}
BDS-600	3	-	-	1.60×10^{-5}	3.27×10^{-5}	4.75×10^{-5}	5.45×10^{-5}
BDS-1000	4	-	-	-	1.32×10^{-5}	3.50×10^{-5}	5.90×10^{-5}
BDS-2500	4	-	-	-	-	2.99×10^{-5}	8.70×10^{-5}
BDS-10000	4	-	-	-	-	-	4.35×10^{-5}

Appendix C

Photon Beam Data

Table C.1: Temperature dependence measurements for BDS.

Average response [bubbles/Gy]	15 ℃	20 ℃	25 ℃
BDS 10	170	171	231
BDS 100	135	192	277
BDS 600	141	227	406
BDS 1000	76	148	331
BDS 2500	43	99	196

Table C.2: Thermal neutron doses measured with the bubble detector thermal (BDT). Position (P), Response (R)

Detector ID	P	R [μSv/Gy]	P	R [μSv/Gy]	P	R [μSv/Gy]	P	R [μSv/Gy]
2	8	191	9	230	14	77.5	15	84
2	8	230	9	210	14	106	15	92
7	8	226	9	150	14	110	15	64.5
7	8	194	9	222	14	108	15	208
9	8	102	9	88	14	35.5	15	27.5
9	8	74	9	106	14	31	15	34
19	8	70	9	72	14	25	15	28
19	8	60	9	82	14	22.5	15	22
20	8	94	9	114	14	32	15	37
20	8	110	9	138	14	34.5	15	93
35	8	192	9	166	14	79	15	62
35	8	204	9	200	14	128	15	55

Appendix D

Carbon Beam Data

Table D.1: Results from measurements 4 cm off axis from the 200 MeV/u pencil beam at GSI 12/1-2009.

Detector	Number of ions	Position	Response [bubbles/10^9 ions]
BDS 10	1.71×10^9	9	251
BDS 10	1.80×10^9	9	230
BDS 10	2.11×10^9	9	235
BDS 10	1.71×10^9	15	201
BDS 10	1.80×10^9	15	209
BDS 10	2.11×10^9	15	256
BDS 2500	1.79×10^9	9	439
BDS 2500	1.79×10^9	10	364
BDS 2500	1.79×10^9	15	437
BDS 2500	1.79×10^9	16	362
BDS 10000	1.71×10^9	10	100
BDS 10000	1.80×10^9	10	122
BDS 10000	2.11×10^9	10	166
BDS 10000	1.71×10^9	16	112
BDS 10000	1.80×10^9	16	148
BDS 10000	2.11×10^9	16	197

Table D.2: Measurements 8 cm off axis from 200 MeV/u pencil beam at GSI 12/1-2009

Detector type	Det. ID	Number of ions	Position	Response [Bubbles]	Bubbles/10^9 ion
BDS 10	1	8.368080×10^9	8	425	51
BDS 10	2	8.368080×10^9	14	365	44
BDS 10000	33	8.368080×10^9	11	264	32
BDS 10000	34	8.368080×10^9	17	333	40

Appendix E

Error Propagation in the Unfolding Process

The method used in this work for unfolding the data from the BDS to obtain spectral information is called “spectral striping”. This procedure is known to suffer from error accumulations, leading to large errors especially in the lower energy regions of the spectrum. The theoretical uncertainties in the various energy intervals can be calculated.

The general uncertainty for error propagation for a function, f, depending on the variables x_1, x_2 and x_3 assuming that the measurements are not correlated is given by

$$\sigma_f^2 = \left(\frac{\partial f}{\partial x_1}\right)^2 \times \sigma_{x_1}^2 + \left(\frac{\partial f}{\partial x_2}\right)^2 \times \sigma_{x_2}^2 + \left(\frac{\partial f}{\partial x_3}\right)^2 \times \sigma_{x_3}^2 \tag{E.1}$$

This formula can be used to estimate the theoretical error in each individual energy region for the neutron spectra obtain with the BDS detectors. As essentially no neutrons with energies above 10 MeV were detected the highest region, N_6, is empty. This leads to that the uncertainty in the fluence for region 5 (1 MeV - 2.5 MeV) is given by

$$\sigma_{N_5} = \frac{\sigma_{R_5}}{s_{55}} \tag{E.2}$$

$$N_4 = \frac{R_4 - s_{45} \times N_5}{s_{44}} \tag{E.3}$$

$$\sigma_{N_4}^2 = \left(\frac{\partial N_4}{\partial R_4}\right)^2 \times \sigma_{R_4}^2 + \left(\frac{\partial N_4}{\partial N_5}\right)^2 \times \sigma_{N_5}^2 \tag{E.4}$$

Using equation B.6 yields

$$\sigma_{N_4}^2 = \left(\frac{\sigma_{R_4}}{s_{44}}\right)^2 + \left(\frac{s_{45}\sigma_{N_5}}{s_{44}}\right)^2 \tag{E.5}$$

In the same manner equations for σ_{N_3}, σ_{N_3}, σ_{N_2} and σ_{N_1} are obtained

$$\sigma_{N_3}^2 = \left(\frac{\sigma_{R_3}}{s_{33}}\right)^2 + \left(\frac{s_{34}\sigma_{N_4}}{s_{33}}\right)^2 + \left(\frac{s_{35}\sigma_{N_5}}{s_{33}}\right)^2 \tag{E.6}$$

$$\sigma_{N_2}^2 = \left(\frac{\sigma_{R_2}}{s_{22}}\right)^2 + \left(\frac{s_{23}\sigma_{N_3}}{s_{22}}\right)^2 + \left(\frac{s_{24}\sigma_{N_4}}{s_{22}}\right)^2 + \left(\frac{s_{25}\sigma_{N_5}}{s_{22}}\right)^2 \tag{E.7}$$

$$\sigma_{N_1}^2 = \left(\frac{\sigma_{R_1}}{s_{11}}\right)^2 + \left(\frac{s_{12}\sigma_{N_2}}{s_{11}}\right)^2 + \left(\frac{s_{13}\sigma_{N_3}}{s_{11}}\right)^2 + ... \tag{E.8}$$

Uncertainties from table 7.1 was put into these equation, and the theoretical errors estimated for the spectra obtain from position 9. The calculated errors are shown in table E.1. Here it has also been taken into account that 9 repeated measurements were performed to reduce the error. The uncertainties in the obtained spectra are larger than the theoretical and includes a number of factors not taken into account in this calculation.

Table E.1: Theoretical uncertainties estimated for the spectrum obtain for position 9.

Energy interval	$\sigma[n/cm^{-2}]$	σ/fluence [%]
10-100 keV	9.9×10^6	59
100-600 keV	1.4×10^6	136
600-1000 keV	9.1×10^5	-
1000-2500 keV	3.6×10^5	26
2500-10000 keV	1.1×10^5	3.3

Appendix F

Neutron Conversion Factors

Table F.1: Fluence to dose conversion factors [30].

Energy interval [MeV]	Fluence-to-dose factor $[pSv/(n.cm^{-2}]$
0.01 - 0.1	5.25×10^1
0.1 - 0.6	2.50×10^2
0.6 - 1	3.38×10^2
1 -2.5	3.63×10^2
2.5 - 10	3.18×10^2

Table F.2: Estimated equivalent neutron doses from the BDS measurements using the conversion factors in table F.1.

Position	Neutron fluence $[\frac{n}{cm^2Gy}]$	Neutron dose [mSv/Gy]
No phantom	5.0×10^7	14.2
8	1.8×10^7	2.2
8 Closed MLC	2.3×10^6	0.8
9	2.3×10^7	2.7
9 Closed MLC	8.0×10^6	1.0
14	4.4×10^6	0.7
15	2.7×10^6	0.8
MC simulations [5]	1.7×10^7	2.9